Exploring Dipolar Coupling and the Chemical Shift for Structure Determination in Solids and in Liquid Crystals.

by

Robert Harold Havlin, Jr.

B.S. (University of Illinois, Urbana-Champaign) 1997

A dissertation submitted in partial satisfaction of the
requirements for the degree of
Doctor of Philosophy

in

Chemistry

in the

GRADUATE DIVISION
of the
UNIVERSITY OF CALIFORNIA, BERKELEY

Committee in charge:
Professor Alexander Pines, Chair
Professor Robert A. Harris
Professor Erwin L. Hahn

Fall 2002

The dissertation of Robert Harold Havlin, Jr. is approved:

Chair Date

Date

Date

University of California, Berkeley

Fall 2002

Exploring Dipolar Coupling and the Chemical Shift for Structure Determination in Solids and in Liquid Crystals.

Copyright 2002

by

Robert Harold Havlin, Jr.

Abstract

Exploring Dipolar Coupling and the Chemical Shift for Structure Determination in Solids and in Liquid Crystals.

by

Robert Harold Havlin, Jr.

Doctor of Philosophy in Chemistry

University of California, Berkeley

Professor Alexander Pines, Chair

The development of novel structural techniques is vital to progress in many fields, most notably chemistry and biology. Nuclear magnetic resonance (NMR) has developed to a degree that ideally enables it to address structural questions. In this work, several new techniques are presented that provide structural parameters for systems which might be difficult to determine structures for by any other method. In particular, liquid crystalline systems such as organic liquid crystals and membrane mimetic bicelle systems can be studied now by utilizing the methods presented in this thesis. Another method for providing structural information for proteins in the solid and liquid state employs developments in *ab initio* chemical shift calculations to generate dihedral angles from spectroscopic observables. Finally, a novel method for creating isotropic dipole coupled spectra in solids is presented and applied to simple samples in an initial step toward becoming a new structural technique.

Professor Alexander Pines
Dissertation Committee Chair

To Jeff Lype,

you will always embody the *excitement* of chemistry in my mind.

Acknowledgments

I would first like to acknowledge my loving family. In particular, my Dad for opening doors of discovery in the sciences, and my Mom for providing me with the courage to walk through them, my sisters (Laura, Nancy, and Karen) who have supported and encouraged me throughout all of my endeavors, and, finally, my Grandma Jean who has been an inspiration all of my life.

I would like to acknowledge my best friend, Eric Castelli, whom I have known all my life and has been a brother to me, and his lovely wife Courtney who helps me to keep my feet on the ground.

For preventing me from becoming a *Mad Scientist*, I would like to acknowledge Preston Snee, Harry Gomez, Rich Schaller, Richard "WTF" Wong, Nick Pivonka, Jason Robinson, and Tanya Mazur.

At Berkeley I have had the experience to work with a number of wonderful scientists, many of whom became close friends.

I am greatly indebted to Tanya Mazur, who has been a very dear friend for most of my time at Berkeley and I have had the pleasure of working with. She has helped me enjoy more of my time at Berkeley scientifically and personally.

One of the most enlightening interactions I have had while at Berkeley was with Jamie Walls, who not only blessed me with his friendship but also his theoretical prowess. Jamie and I explored many wonderful ideas in NMR and found a few that worked; for example, the theory in Chapter 7 is entirely due to his brilliance.

For providing a very stimulating, but strange family-type environment during my

stay at Berkeley, I would like to thank all of the Pinenuts. Early in my graduate career, Prof. Dave Wemmer, Marco Tomaselli, Prof. Boyd Goodson and Prof. Seth Bush made for an exciting research environment. People who have contributed to the work in this thesis include: Jamie Walls, Tanya Mazur, Bo Blanton, Lori Sanders, Greg Park, Morgan Moschetti, David Laws, Hans Bitter, Maggie Marjanska, Dimitris Sakellariou, and Kim Pierce.

Not all of the work done during my graduate career is included in this thesis. Some of the more *hare-brained* ideas I had the fortunate opportunity to explore in collaboration with Prof. Erwin Hahn, Prof. Matt Augustine, and Andreas Trabesinger did not make the cut.

I would like to thank Prof. Eric Oldfield for being a wonderful mentor during my studies at the University of Illinois and helping me start my career in NMR.

And finally, I would like to acknowledge Prof. Alexander Pines who has provided an excellent environment where students are free to explore some of his wonderful ideas as well as their own.

Contents

List of Figures vii

List of Tables ix

1 Introduction 1

2 Basics of NMR 3
- 2.1 The Hamiltonians . . . 3
  - 2.1.1 Zeeman . . . 6
  - 2.1.2 Radio Frequency . . . 7
  - 2.1.3 Chemical Shift . . . 8
  - 2.1.4 J Coupling . . . 10
  - 2.1.5 Dipolar Coupling . . . 11
  - 2.1.6 Quadrupolar Coupling . . . 13
- 2.2 Calculating Observables . . . 14
- 2.3 The Experimental Setup . . . 17

3 Liquid Crystal NMR 19
- 3.1 Introduction to Liquid Crystals . . . 19
  - 3.1.1 A 'Meso'-Phase of Matter . . . 19
  - 3.1.2 Types . . . 21
  - 3.1.3 Magnetic Properties . . . 23
  - 3.1.4 Order Parameter . . . 25
- 3.2 Partially Averaged Observables . . . 28
- 3.3 Recent Approaches . . . 30
  - 3.3.1 Simple One-Dimensional Experiments . . . 31
  - 3.3.2 Multiple Quantum . . . 32
  - 3.3.3 Local Field . . . 34

4 Dynamic Director Experiments in Liquid Crystals 37
- 4.1 Introduction Director Alignment . . . 37
  - 4.1.1 Advantages of Oriented Systems . . . 37
  - 4.1.2 Techniques for Simplifying Spectra . . . 43

4.2 Variable Angle Spinning (VAS) Experiments . . . 48
4.2.1 Scaling Couplings: Second Order, First Order, Isotropic . . . 49
4.3 Switched Angle Spinning Probehead . . . 52
4.4 SAS: Parallel Director Alignment . . . 54
4.4.1 First Order System: C_2F_3I . . . 54
4.4.2 Second Order: C_6F_5Cl . . . 62
4.5 SAS: Switched Director Alignment . . . 68
4.5.1 Introduction . . . 68
4.5.2 Results . . . 69
4.6 Conclusions . . . 72
4.7 Future Directions . . . 73

5 Solid State NMR **79**
5.1 Issues in the Solid State . . . 79
5.1.1 Decoupling Strong Interactions . . . 83
5.2 Current Abilities . . . 83

6 Using the CSA to Determine Structure **86**
6.1 Introduction . . . 86
6.2 Proteins and Peptides . . . 87
6.3 CSA Tensors in Proteins and Peptides . . . 88
6.3.1 Experimental Section . . . 90
6.3.2 Results and Discussion . . . 93
6.3.3 Conclusions . . . 107

7 Dipolar Coupling Measurements in the Solid State **109**
7.1 Introduction . . . 109
7.2 Tycko's Zero-Field in High-Field . . . 111
7.3 Isotropic Homonuclear Recoupling (HOMIE) . . . 116
7.3.1 Implementation and Simulation of HOMIE . . . 121
7.3.2 Experimental Demonstration of HOMIE . . . 126
7.4 Isotropic PDLF Spectroscopy (HETIE) . . . 130
7.4.1 Theory of heteronuclear isotropic spectra . . . 133
7.4.2 Implementation and Simulation of HETIE . . . 139
7.4.3 Experimental Demonstration of HETIE . . . 147
7.4.4 Results . . . 149

8 Conclusion **156**
8.1 Oriented Systems . . . 156
8.2 Solid State . . . 157
8.2.1 Structure from CSA . . . 157
8.2.2 Isotropic Dipolar Spectra . . . 157
8.3 NMR Crystallography . . . 158

Bibliography **159**

A Appendix **172**
A.1 Irreducible Tensor Representations of Spin Interactions 172
A.2 Simulation Programs 174
A.3 Pulse Sequences 180
A.4 Processing Scripts 189

List of Figures

2.1 Principal Axes 5

3.1 Cartoon of the Order in Phases 22
3.2 Mesogen in a magnetic field. 25
3.3 1D ^{1}H spectrum of methylene chloride (CH_2Cl_2) dissolved in the liquid crystal I52 31
3.4 1D ^{19}F NMR spectrum of C_6F_5Cl in the liquid crystal I52 33
3.5 Proton Detected Local Field Pulse Sequence with PMLG Decoupling 35
3.6 Proton Detected Local Field 2D Spectrum of $C_6H_2Cl_2FNO_2$ in a nematic liquid crystal 36

4.1 Cartoon of an oriented liquid crystalline spinning sample 39
4.2 One-dimensional ^{19}F spectra of C_2F_3I 40
4.3 ^{19}F spectrum of C_6F_5Cl in a nematic liquid crystal 42
4.4 Angle Dependence of ^{19}F shifts and splittings of C_2F_3I in a liquid crystal . 47
4.5 ^{19}F spinning spectra of perfluorochlorobenzene in a liquid crystal 50
4.6 Switched angle spinning (SAS) probe diagram 53
4.7 Iodotrifluoroethylene with A, M, and X ^{19}F spins labeled. 55
4.8 Switched Angle Spinning COSY45 Pulse Sequence. 55
4.9 COSY45 and SAS-COSY45 2D Correlations of C_2F_3I in a nematic liquid crystal. 60
4.10 Two dimensional switched angle spinning pulse sequence. 63
4.11 Two dimensional ^{19}F switched angle spinning correlation of C_6F_5Cl in a liquid crystal. 65
4.12 Two dimensional second order ^{19}F switched angle spinning correlation of C_6F_5Cl in a liquid crystal. 67
4.13 Two dimensional switched angle spinning pulse sequence providing sideband correlations. 68
4.14 Two dimensional ^{19}F switched angle spinning correlation of C_6F_5Cl in a liquid crystal perpendicular phase. 71
4.15 DMPC lipid molecule 74
4.16 1D Proton Spectra of Oriented Bicelles Under Different Conditions. 75

4.17 Variable Angle Spinning of an Oriented Bicelle 76
4.18 Plot of the Variable Angle Spinning of an Oriented Bicelle 76
4.19 SAS-PDLF Simulation of and Oriented Bicelle 78

5.1 Diagram of the homonuclear dipolar powder pattern 81
5.2 Diagram of the principal elements of the CSA tensor 82
5.3 ^{13}C CP-MAS spectra of labeled glycine 84

6.1 Diagram of ϕ, ψ dihedral angles in an amino acid 88
6.2 Locally dense basis set diagram of a Leucine Fragment 92
6.3 Fit of the experimental MAS spectrum of a Leucine $^{13}C_\alpha$ labelled peptide. . 94
6.4 Computed shielding surfaces for $^{13}C^\alpha$ in N-formyl leucine amide **mt** 95
6.5 Correlation plot of $^{13}C^\alpha$ chemical-shielding tensor elements for alanine, valine, and leucine peptides 98
6.6 Computed shielding surfaces for $^{13}C^\alpha$ in N-formyl leucine amide **tp** 99
6.7 Computed shielding surfaces for $^{13}C^\alpha$ in N-formyl leucine amide **tt** 99
6.8 Comparison of experimental and theoretical chemical shift tensor elements for Ala, Val and Leu peptides 102
6.9 Fit of the experimental MAS spectrum of a Leucine $^{13}C_\alpha$ labelled peptide. . 106
6.10 Theory versus experiment comparison of the C^α solution CSA ($\Delta\sigma^* = \sigma_{orth}$-$\sigma_{par}$) 107

7.1 Zero-field vs. high-field spectrum of dipole-coupled spin system 113
7.2 The Basic procedure in order to obtain isotropic dipolar spectra. 117
7.3 An ideal HOMIE sequence and simulations demonstrating performance. . . 124
7.4 Actual experiments performed in order to obtain the HOMIE isotropic dipolar spectra 127
7.5 Experimental HOMIE results overlaid with a simulation. 129
7.6 Comparison of zero-field proton-detected local field spectroscopy with high-field proton-detected local field spectroscopy 132
7.7 The Basic procedure in order to obtain isotropic proton detected local field dipolar spectra. 136
7.8 Basic pulse sequences to create the various Hamiltonians needed for HETIE 142
7.9 ^{1}H NMR spectrum of $FeCp_2$ spinning 15 kHz at 73.9° 148
7.10 Actual experiment performed for demonstration of HETIE methodology . . 150
7.11 Simulation of the performance of the HETIE pulse sequence 152
7.12 HETIE experiment and simulation comparison for $FeCp_2$ 154

List of Tables

2.1 Interaction Hamiltonians 6

4.1 Chemical shift parameters from C_2F_3I 57
4.2 Coupling Constants from the Line Fits in Figure 4.4 58

6.1 Experimentally Measured $^{13}C^{\alpha}$ Chemical Shift Tensor Information in ppm for Ala-, Val-, and Leu-containing Peptides 93
6.2 Table of shielding calculations for peptides **1-11** 96

Chapter 1

Introduction

Perhaps one of the most important questions in chemistry and biology today is: What is the structure of a given molecule, peptide, or protein, etc.? Understanding the three-dimensional (3D) structure of a catalyst can allow a chemical engineer make improvements in an industrial process to reduce pollution. Knowing the 3D fold of an enzyme enables a molecular biologist to design a drug that saves the life an alarming number of AIDS patients worldwide. Without a doubt, structural methods have an impact on the world around us.

Structural techniques such as X-ray crystallography have developed to an extent where the structure of almost any molecule or protein can be determined if a single crystal of it can be grown. Problems arise with X-ray crystallography when crystals cannot be grown or a molecule has a dynamic structure. Obviously, other methods are required when X-ray crystallography fails to provide a structure for a sample of great importance.

An alternate method for structure determination that has been growing in importance is nuclear magnetic resonance (NMR). NMR spectroscopy has made the largest

impact in the determination of protein structures, and a pioneer in NMR was awarded the Nobel Prize this year for his contributions in this area[1]. The information provided by NMR structures is not only complementary to X-ray crystallography, but it can provide additional information about dynamics. Another benefit of structure determination by NMR is that it is performed on molecules in solution and not the single crystals required for X-ray diffraction. Since NMR structures are typically determined in water, it is well suited to study proteins and other biologically relevant molecules; these systems are almost exclusively found in water and are difficult to crystallize.

However, many molecules of significance cannot be studied by X-ray or liquid state NMR methods. Molecules such as zeolite catalysts or membrane proteins are examples of systems that cannot be studied by these methods. In these cases, researchers often turn to an alternate method such as solid state NMR which can study solids as well as solid-like systems.

The content of this thesis describes some novel attempts toward reaching the ultimate goal of a methodology which can be described as NMR crystallography. This methodology is able to determine 3D structures of molecules from observed interactions in NMR that are described by the Hamiltonians in the following chapter.

Chapter 2

Basics of NMR

2.1 The Hamiltonians

The nuclear spin Hamiltonian can be written as a sum of internal and external parts:

$$H = H_{int} + H_{ext}. \tag{2.1}$$

With this separation, the effects intrinsic to the spin system are included in the H_{int} Hamiltonian while H_{ext} contains terms due to the experimental setup. The H_{int} can be further subdivided into the basic interactions resulting from the environment of the nucleus:

$$H_{int} = H_{CS} + H_J + H_D + H_Q \tag{2.2}$$

where H_{CS} is the chemical shielding (or chemical shift), H_J is the indirect spin-spin coupling (or J coupling), H_D is the direct dipole-dipole coupling (or dipolar coupling), and H_Q is the quadrupolar coupling. Each of these interactions is intrinsic to the spin system and

primarily depends upon the chemical environment of the nucleus.

Effects that are a result of actions performed on the spin system are included in the external Hamiltonian, and they can usually be separated into Zeeman and radio frequency (RF) contributions:

$$H_{ext} = H_Z + H_{RF}. \tag{2.3}$$

It is through the Hamiltonian of Eq. (2.3) that the experimenter is able to interact with the spins, and this has been the focus of much of the field of NMR[2].

With a thorough knowledge of the information that is intrinsically available from the internal Hamiltonian of Eq. (2.2), we can tailor our H_{ext} to extract the desired information. Each of the components of the internal and external Hamiltonians will be described in more detail below.

The basic NMR interaction Hamiltonians can be described as the product of vectors $\mathbf{I}$ and $\mathbf{S}$ with a second rank Cartesian tensors ($\hat{\mathbf{A}}$) which are 3x3 matrices:

$$H = \mathbf{I} \cdot \hat{\mathbf{A}} \cdot \mathbf{S} = \begin{bmatrix} I_X & I_Y & I_Z \end{bmatrix} \begin{bmatrix} A_{XX} & A_{XY} & A_{XZ} \\ A_{YX} & A_{YY} & A_{YZ} \\ A_{ZX} & A_{ZY} & A_{ZZ} \end{bmatrix} \begin{bmatrix} S_X \\ S_Y \\ S_Z \end{bmatrix}. \tag{2.4}$$

For example, coupling of the spin $\mathbf{I}$ to an external magnetic field can be represented as:

$$H_{0,I} = \mathbf{I} \cdot \hat{\mathbf{Z}} \cdot \mathbf{B}_0 \tag{2.5}$$

where $\hat{\mathbf{Z}} = -\gamma_I \hat{\mathbf{1}}$ and $\mathbf{B}_0 = (B_x, B_y, B_z)$.

These second rank Cartesian tensors are represented in the molecular axis system; they can be made diagonal in their principal axis system (PAS) to yield three principal components (A_{11}, A_{22}, A_{33}). This is depicted in Figure 2.1:

$$H_{PAS} = \begin{bmatrix} A_{11} & 0 & 0 \\ 0 & A_{22} & 0 \\ 0 & 0 & A_{33} \end{bmatrix}.$$

Often times in NMR, frame transformations are performed in and out of the PAS to

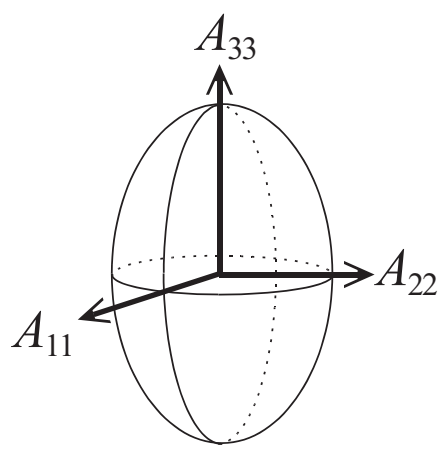

Figure 2.1: Ellipsoid representing a second rank interaction tensor in the principal axis system.

facilitate calculations.

In addition to expressing spin interactions in terms of Cartesian tensors, they may also be written using spherical tensors. This is often times more convenient when calculating the effects of rotations or other unitary transformations[3]. The general form of

the Hamiltonian written in spherical tensors is then:

$$H = \sum_{l=0}^{2} \sum_{m=-l}^{+l} (-1)^m A_{lm} T_{l-m} \tag{2.6}$$

where A_{lm} is a rank l spherical tensor due to space and T_{l-m} is a rank l spherical tensor due to spin space. The details of this representation are treated in more detail in Appendix A.1 and are used extensively in Chapter 7.

Interaction	**Hamiltonian**
Chemical Shift	$H_{CS} = \gamma \mathbf{I} \cdot \hat{\sigma} \cdot \mathbf{B_0}$
Dipole-Dipole	$H_D = \frac{\gamma_i \gamma_j \hbar}{r_{ij}^3}[\mathbf{I}_i \cdot \mathbf{I}_j - \frac{3(\mathbf{I}_i \cdot \mathbf{r}_{ij})(\mathbf{I}_j \cdot \mathbf{r}_{ij})}{r_{ij}^2}]$ $H_D = \mathbf{I}_i \cdot \hat{\mathbf{D}} \cdot \mathbf{I}_j$
J-coupling	$H_J = \mathbf{I}_i \cdot \hat{\mathbf{J}} \cdot \mathbf{I}_j$
Quadrupolar coupling	$H_Q = \frac{eQ}{2I(2I-1)\hbar} \mathbf{I} \cdot \hat{\mathbf{V}} \cdot \mathbf{I}$

Table 2.1: Interaction Hamiltonians

2.1.1 Zeeman

The largest interaction in magnetic resonance is that of the spin with the large external magnetic field. It is this field which creates the $2I+1$ non-degenerate spin angular momentum energy levels characterized by the spin angular momentum quantum number I. When written as a second rank Cartesian tensor, the Zeeman Hamiltonian has the form:

$$H_Z = -\mathbf{I} \cdot \hat{\mathbf{Z}} \cdot \mathbf{B}. \tag{2.7}$$

Eq. 2.7 is simplified when the magnetic field is only applied in the z direction:

$$H_Z = -\gamma B_z I_z \tag{2.8}$$

where γ is the magnetogyric ratio ($\gamma_{^1H} = 26.7522128 \times 10^7 \frac{rad}{T \cdot s} = 42.58 \frac{MHz}{T}$ and $\gamma_{^{13}C} = 6.728284 \times 10^7 \frac{rad}{T \cdot s} = 10.71 \frac{MHz}{T}$), B_z is the magnetic field strength, and I_z is a spin angular momentum operator with eigenvalues $m = -I, (-I+1), ..., I$. The Zeeman Hamiltonian is often written in the form:

$$H_Z = \omega_0 I_z \tag{2.9}$$

where ω_0 is the Larmor frequency and is given by $\omega_0 = -\gamma B_z$.

2.1.2 Radio Frequency

The other external interaction is represented by the RF Hamiltonian which occurs due to an applied RF field of frequency ω and strength $\omega_1 = -\gamma B_z$:

$$H_{RF} = 2\omega_1 \cos(\omega t + \phi) I_x. \tag{2.10}$$

This Hamiltonian is utilized to describe the application of RF pulses.

Rotating Frame

In an effort to simplify the calculation and interpretation of NMR signals, we often perform the rotating frame transformation to remove the large Zeeman term from the

analysis. In the rotating frame transformation, Eq. 2.10 becomes:

$$H_{RF} = \omega_1(\cos\phi I_x + \sin\phi I_y). \tag{2.11}$$

In this manner, the frequency of the applied field does not oscillate but instead lies in the x-y plane at an angle ϕ from the x axis. This results in the replacement of the Larmor frequency with an offset frequency $\Delta\omega = \omega_0 - \omega$ in the Zeeman Hamiltonian:

$$H_Z = \Delta\omega I_z. \tag{2.12}$$

This frame transformation allows us to focus on the smaller perturbations that represent the interesting aspects of NMR.

2.1.3 Chemical Shift

The field experienced at the nucleus generally is not exactly the applied B_z; instead, the nucleus is shielded by the surrounding bonding electrons, and the field it experiences varies accordingly. This chemical shielding Hamiltonian can be written as:

$$H_{CS} = \gamma \mathbf{I} \cdot \hat{\sigma} \cdot \mathbf{B_0} \tag{2.13}$$

where $\hat{\sigma}$ represents a second rank tensor describing the chemical shielding. The following relationship is noteworthy to remember

$$\delta = (\sigma_{ref} - \sigma) \tag{2.14}$$

where δ represents the chemical shift which is commonly what is reported experimentally, and σ_{ref} is the absolute shielding of a reference compound (such as tetramethylsilane). Therefore, we can discuss either chemical shielding or chemical shift in the following chapters. The chemical shielding in the PAS can be separated into an isotropic:

$$\begin{aligned} H_{CS}^{iso} &= \gamma B_z \frac{1}{3}(\sigma_{11} + \sigma_{22} + \sigma_{33}) I_z \\ &= -\omega_0 \sigma_{iso} I_z \end{aligned} \tag{2.15}$$

and an anisotropic part:

$$\begin{aligned} H_{CS}^{aniso} = & - \frac{1}{3}\omega_0[\sigma_{33} - \frac{1}{2}(\sigma_{11} + \sigma_{22})](3\cos^2\beta - 1) I_z \\ & - \frac{1}{2}\omega_0[(\sigma_{11} - \sigma_{22})\sin^2\beta\cos 2\alpha] I_z. \end{aligned} \tag{2.16}$$

If we define $\Delta\sigma = \sigma_{33} - \sigma_{iso}$ as the chemical shift anisotropy (CSA) and $\eta = \frac{\sigma_{22}-\sigma_{11}}{\Delta\sigma}$ as the asymmetry of the chemical shift, then the anisotropic part becomes:

$$H_{CS}^{aniso} = -\frac{1}{2}\omega_0 \Delta\sigma[(3\cos^2\beta - 1) + \eta\sin^2\beta\cos 2\alpha] I_z \tag{2.17}$$

where α and β relate the principal axis system of the chemical shielding tensor to the lab frame where the field is oriented along the z axis. Therefore, the total chemical shielding Hamiltonian is:

$$H_{CS} = -\omega_0 \sigma_{iso} I_z - \frac{1}{2}\omega_0 \Delta\sigma[(3\cos^2\beta - 1) + \eta\sin^2\beta\cos 2\alpha] I_z \tag{2.18}$$

Quantities which are convenient for comparing the chemical shift anisotropy tensors as defined by Jameson [88] are the span (Ω, which is always positive) and skew (κ, ranging from -1 to +1):

$$\Omega = (\sigma_{33} - \sigma_{11}), \quad where \;\; \sigma_{33} \geq \sigma_{22} \geq \sigma_{11} \tag{2.19}$$

$$\kappa = (\sigma_{iso} - \sigma_{22})/(\sigma_{33} - \sigma_{11}), \quad where \;\; \sigma_{33} \geq \sigma_{22} \geq \sigma_{11} \tag{2.20}$$

2.1.4 J Coupling

Indirect spin-spin coupling, also called the J coupling, is the interaction between nuclei mediated through the bonding electrons in the molecule. The J coupling can also be expressed as a second rank Cartesian tensor:

$$H_J = \mathbf{I_i} \cdot \hat{\mathbf{J}} \cdot \mathbf{I_j}. \tag{2.21}$$

Although most people are familiar with the isotropic part of the J coupling observed in liquid state NMR, an anisotropic part also exists which is not usually seen. Using the familiar ladder operators:

$$I_{\pm} = I_X \pm iI_Y, \tag{2.22}$$

we simplify Eq. (2.21) to:

$$H_J = J_{ZZ} I_{i,Z} I_{j,Z} + \frac{1}{4}(J_{ij,XX} + J_{ij,YY})(I_{i,+}I_{j,-} + I_{i,-}I_{j,+}) \tag{2.23}$$

where only those terms that commute with I_Z are observable. In Eq. (2.23) the J coupling can be separated into the isotropic:

$$H_J^{iso} = J_{ZZ} I_{i,Z} I_{j,Z} \tag{2.24}$$

and the anisotropic part:

$$H_J^{aniso} = \frac{1}{4}(J_{ij,XX} + J_{ij,YY})(I_{i,+}I_{j,-} + I_{i,-}I_{j,+}). \tag{2.25}$$

Thus, even if the anisotropic part is not negligible, it will be difficult to separate it from the direct dipolar couplings experimentally.

2.1.5 Dipolar Coupling

The direct dipole-dipole interaction, also called dipolar coupling, is the interaction of two spins through space. Unlike the J coupling or the chemical shift, the dipolar coupling has no isotropic part; therefore, in liquid state NMR where the samples are isotropically tumbling, the dipolar coupling is not observed. The dipolar coupling interaction can be expressed as a second-rank Cartesian tensor that is both symmetric and traceless:

$$H_D = \mathbf{I_i} \cdot \hat{\mathbf{D}} \cdot \mathbf{I_j}. \tag{2.26}$$

Again, it is more convenient to write the interaction in the laboratory frame; this frame is rotated from the principal axis system and is axially symmetric about the internuclear

vector. The second rank tensor $\hat{D}$ can be rewritten as:

$$D_{\alpha\beta} = \frac{\mu_0 \hbar \gamma_i \gamma_j}{4\pi r_{ij}^3}[\delta_{\alpha\beta} - 3e_\alpha e_\beta] \tag{2.27}$$

where α and β are the laboratory fixed axes X,Y,Z, $\delta_{\alpha\beta}$ is the Kronecker delta function (1 if $\alpha = \beta$, 0 if $\alpha \neq \beta$) and $e_{\alpha,\beta}$ is the α, β component of the unit vector along the internuclear vector, $\vec{r}_{ij}$. Using spherical coordinates and the ladder operators of Eq. (2.22), Eq. (2.26) can be rewritten as:

$$H_D = \frac{\mu_0 \hbar \gamma_i \gamma_j}{4\pi r_{ij}^3}(A + B + C + D + E + F) \tag{2.28}$$

with

$$A = (1 - 3\cos^2\theta_{ij}) I_{i,Z} I_{j,Z} \tag{2.29}$$

$$B = -\frac{1}{4}(1 - 3\cos^2\theta_{ij})(I_{i,+} I_{j,-} + I_{i,-} I_{j,+}) \tag{2.30}$$

$$C = -\frac{3}{2}\sin\theta_{ij}\cos\theta_{ij} e^{-i\phi_{ij}}(I_{i,+} I_{j,Z} + I_{i,Z} I_{j,+}) \tag{2.31}$$

$$D = C^* = -\frac{3}{2}\sin\theta_{ij}\cos\theta_{ij} e^{+i\phi_{ij}}(I_{i,-} I_{j,Z} + I_{i,Z} I_{j,-}) \tag{2.32}$$

$$E = -\frac{3}{4}\sin^2\theta_{ij} e^{-i2\phi_{ij}} I_{i,+} I_{j,+} \tag{2.33}$$

$$F = E^* = -\frac{3}{4}\sin^2\theta_{ij} e^{+i2\phi_{ij}} I_{i,-} I_{j,-}. \tag{2.34}$$

$$\tag{2.35}$$

Keeping only those terms in the Hamiltonian that commute with I_Z, we are left with only the 'secular' terms:

$$H_D = 2D_{ij,ZZ}[I_{i,Z}I_{j,Z} - \frac{1}{4}(I_{i,+}I_{j,-} + I_{i,-}I_{j,+})] \tag{2.36}$$

where

$$D_{ij,ZZ} = \frac{\mu_0 \hbar \gamma_i \gamma_j}{4\pi r_{ij}^3}(1 - 3\cos^2\theta_{ij}). \tag{2.37}$$

2.1.6 Quadrupolar Coupling

The quadrupolar interaction, referred to as the quadrupolar coupling, exists only for nuclei with $I > \frac{1}{2}$. The interaction can be expressed as a second rank tensor:

$$H_Q = \frac{eQ}{2I(2I-1)\hbar}\mathbf{I} \cdot \hat{\mathbf{V}} \cdot \mathbf{I} \tag{2.38}$$

where I is the spin of the nucleus, e is the charge of an electron, Q is the quadrupolar coupling constant for the nucleus, and $V_{\alpha\alpha}$ are the components of the electric field gradient tensor in the PAS. If we define $\eta = \frac{V_{xx}-V_{yy}}{V_{zz}}$ as the asymmetry, q as the field gradient, and the quadrupole frequency as:

$$\omega_Q = \frac{3e^2qQ}{4I(2I-1)\hbar}, \quad eq = V_{zz} \tag{2.39}$$

Eq. (2.38) becomes:

$$H_Q = \omega_Q \left[(I_Z^2 - \frac{1}{3}I^2) + \frac{\eta}{3}(I_x^2 - I_Y^2)\right] \tag{2.40}$$

with the principle values of the electric field gradient tensor $|V_{xx}| \leq |V_{yy}| \leq |V_{zz}|$ and the asymmetry $0 \leq \eta \leq 1$.

2.2 Calculating Observables

Now that the relevant interaction Hamiltonians have been described in detail for our NMR experiments, a brief review is provided on how to utilize the Hamiltonians to calculate an NMR signal. Using the density matrix method, we begin by describing our equilibrium density operator which is determined by the populations of states given by the Boltzmann distribution [4]:

$$p_i \propto e^{-\beta E_i} \tag{2.41}$$

where E_i is the energy of the state i and $\beta = \frac{1}{kT}$. The dominant energy contribution to our system is the Zeeman energy, thus we have:

$$\rho_{eq} = p_i \propto e^{-\beta\omega_0 I_z} \tag{2.42}$$

for the equilibrium density operator. Since the Zeeman energy is small compared to β, we can expand the exponential as a Taylor series and truncate it as follows:

$$\rho_{eq} = 1 - \beta\omega_0 I_z. \tag{2.43}$$

The constant term and the constants do not evolve; therefore they will be dropped, leaving the reduced density operator:

$$\rho_{eq} = I_z. \tag{2.44}$$

Under the influence of a Hermitian Hamiltonian, the time evolution of the density operator can be described by the Liouville-von Neumann equation [5, 6]:

$$\frac{d\rho}{dt} = i[\rho, H]. \tag{2.45}$$

This equation can be solved for a time-independent Hamiltonian to yield:

$$\rho(t) = e^{-iHt}\rho(0)e^{iHt}. \tag{2.46}$$

If the time evolution of the system can be divided up into several time intervals, each governed by a time-independent Hamiltonian, the evolution can be expressed by:

$$\rho(t) = e^{-iH_n t_n} e^{-iH_{n-1} t_{n-1}} \cdots e^{-iH_1 t_1} \rho(0) e^{-iH_1 t_1} \cdots e^{-iH_{n-1} t_{n-1}} e^{-iH_n t_n}. \tag{2.47}$$

Using Eq. (2.47) and the Hamiltonians given in the previous sections, we can now calculate the density operator at a given time. In order to generate a the detected signal from the calculated evolution, $\rho(t)$, we employ the operator $I_+ = I_x + iI_y$ which reflects what is detected by the NMR spectrometer. The signal, $S(t)$, is then calculated by:

$$S(t) = Tr(\rho I_+). \tag{2.48}$$

For example, the signal calculated from the NMR experiment which is simply a $(\frac{\pi}{2})_y$ RF-pulse is:

$$S(t) = Tr(e^{-iHt} e^{-i\frac{\pi}{2}I_y} \rho_{eq} e^{i\frac{\pi}{2}I_y} e^{-iHt} I_+). \tag{2.49}$$

Here the RF Hamiltonian is expressed in terms of the pulse angle $\theta = \omega_1 \tau = \frac{\pi}{2}$ and the spin operator I_y. Immediately following the pulse, the density operator is:

$$\rho(0) = e^{-i\frac{\pi}{2}I_y} I_z e^{i\frac{\pi}{2}I_y} = I_x. \tag{2.50}$$

The signal then simplifies to:

$$S(t) = Tr(e^{-iHt} I_x e^{iHt} I_+), \tag{2.51}$$

and using the properties of the trace [7]:

$$S(t) = Tr(I_x e^{iHt} I_+ e^{-iHt}). \tag{2.52}$$

For an actual calculation, we must choose a basis set; in this case the most convenient is the eigenstates of the Hamiltonian $|i>$. The signal is then:

$$S(t) = \sum_i \langle i|I_x e^{iHt} I_+ e^{-iHt}|i\rangle \tag{2.53}$$

$$S(t) = \sum_{i,j} \langle i|I_x e^{iHt}|j\rangle\langle j|I_+ e^{-iHt}|i\rangle \tag{2.54}$$

$$S(t) = \sum_{i,j} e^{i(\omega_j - \omega_i)t} \langle i|I_x|j\rangle\langle j|I_+|i\rangle \tag{2.55}$$

where ω_i and ω_j are the eigenvalues of the Hamiltonian and $(\omega_j - \omega_i)$ is the transition frequency. The difference between the diagonal elements of the Hamiltonian matrix $(\omega_j - \omega_i)$ provides the observed transition frequencies, and the product $\langle i|I_x|j\rangle\langle j|I_+|i\rangle$ gives the relative amplitude of the signal at this frequency. Thus we have successfully calculated the

NMR signal.

2.3 The Experimental Setup

The previous section describes a basic introduction to the elegant theory detailing the interactions and methods for calculating NMR signals. However, the experiment is implemented with real hardware which will be described briefly below.

The most important element required for any magnetic resonance experiment is the magnet (with the exception of some novel zero-field experiments). In the early days of NMR, the magnets were electromagnets, and the field was swept through the resonance condition for a given continuous-wave (CW) RF irradiation. Today, spectrometers operate in a pulsed mode, and the magnets are superconductors with a fixed field strength. The superconducting coils of today's magnets are usually constructed with several miles worth of a Niobium-Titanium alloy that superconducts at 10 K. This is why a sophisticated liquid nitrogen and liquid helium dewaring system is required.

The probe in a NMR experiment serves two roles; it applies a perturbation to the sample and detects the sample's response to the initial perturbation. The basic design for the probe is a inductive-capacitive tank circuit which resonates at a tuned frequency given by $\omega_0 = \frac{1}{\sqrt{LC}}$. The inductance defined by L is the total inductance for the circuit, including the main inductor which surrounds the sample and actually detects the precessing magnetization of the spins in the sample, while C is the capacitance provided by the tuning and matching capacitors. This basic Faraday transmit-detect design for magnetic resonance has performed amazingly well throughout the history of NMR and has yet to be

truly challenged by other methods such as optical detection[8] or SQUID (superconducting quantum interference device) detection[9].

Interestingly, the detection efficiency of the Faraday detector has been perfected to the degree that the limits are now due to the thermal noise of the wire and other electronic components. However, by cryogenically cooling the components this noise is reduced. NMR probes having cryogenic cooling of the probe coil and preamplifier systems are now commercially available. These probes provide better S/N on a 500 MHz magnet than a standard probe on a 800 MHz magnet (at an $\sim$ \$2M higher cost). Detection limits are in the sub-μmol range, but more importantly many previously nonviable experiments can be performed with a cryoprobe[10, 11].

The limitation on the circuit's performance as a transmitter is obviously highly system dependent; however, optimized commercial systems can provide amplitudes of $\omega_1/2\pi$ = 150-200 kHz (ω_1 is the frequency at which the spins precess about the applied RF field). In several of the experiments in this thesis, these limits presented some problems as is addressed in the solid state chapters.

The remainder of the experimental setup consists of converting the detected current in the coil into a digital signal; this has been treated in excellent detail by Fukushima[12].

Chapter 3

Liquid Crystal NMR

3.1 Introduction to Liquid Crystals

In the introduction of this thesis the point was stressed that we desire to help develop a structural method which is applicable where X-ray crystallography and liquid state NMR are deficient. Liquid crystalline phases are applicable here because they span a variety of systems including membrane proteins in their native state which is difficult to study by either of the other two methods. As is described below, the liquid crystalline phase has properties that are ideally suited to allow accurate determination of some of the anisotropic interactions described above.

3.1.1 A 'Meso'-Phase of Matter

The study of liquid crystals began in 1888 when an Austrian botanist named Friedrich Reinitzer observed that a material known as cholesteryl benzoate had two distinct melting points[13]. In his experiments, Reinitzer increased the temperature of a solid sample

and watched the crystal change into a hazy liquid. As he increased the temperature further, the material changed again into a clear, transparent liquid. Because of this early work, Reinitzer is often credited with discovering a new phase of matter - the liquid crystalline phase.

Liquid crystalline materials generally have several common characteristics. Among these are a rod-like molecular structure, rigidness of the long axis, and strong dipolar moments and/or easily polarizable substituents.

The primary distinguishing characteristic of the liquid crystalline state is the tendency of the molecules (mesogens) to align along a common axis, called the director and denoted $\vec{n}$. This is in direct contrast to molecules in the liquid phase (where there is no intrinsic order) or the solid state (where molecules are highly ordered and have little translational freedom). The characteristic orientational order of the liquid crystalline state is between that of traditional solid and liquid phases, and this is the origin of the term mesogenic state, used synonymously with liquid crystalline state.

To quantify how much order is present in a material, an order parameter (S) is defined. Traditionally, the order parameter is given as follows:

$$S = \frac{1}{2}\langle 3\cos^2\theta - 1\rangle \tag{3.1}$$

where θ is the angle between the director ($\vec{n}$) and the long axis of each molecule. The brackets denote an average over all of the molecules in the sample. In an isotropic liquid, the average of the cosine term is zero, and therefore the order parameter is equal to zero. For a perfect crystal, the order parameter evaluates to one. Typical values for the order

parameter of a liquid crystal range between 0.3 and 0.9. As a result of kinetic molecular motion, the exact value is a function of temperature. This is illustrated in Figure 3.1 for a nematic liquid crystal (to be discussed further in the next section).

The tendency of the liquid crystal molecules to point along the director leads to a condition known as anisotropy. The anisotropic nature of liquid crystals is responsible for the unique properties exploited by scientists and engineers in a variety of applications, including magnetic resonance which is explored to a limited degree in this thesis.

3.1.2 Types

Liquid crystals (LCs) are typically organic compounds that flow like a liquid while maintaining the long-range order of a solid. When crystals of a pure compound are heated, they normally show a well-defined and characteristic melting point where the ordered crystalline lattice structure breaks down and the material becomes a liquid. In the liquid phase, the individual molecules show no preferred spatial orientation. A unique feature of liquid crystals is that, during the melting process, the well-ordered three-dimensional crystalline structure transforms into a one- or two-dimensional ordered state. This results in a material that has some of the optical properties of a solid combined with the fluidity of a liquid; therefore this material displays a potpourri of unique properties. The molecular aggregates (collection of molecules) of an LC compound are in the form of long cigar-shaped rods. The orientation of these rod-like polar molecules forms the basis for classifying three basic types of liquid crystals: smectic, nematic, and cholesteric. The smectic phase consists of flat layers of cigar-shaped molecules with their long axes oriented perpendicular to the plane of the layer. This is the most ordered LC phase. The molecules within each layer remain

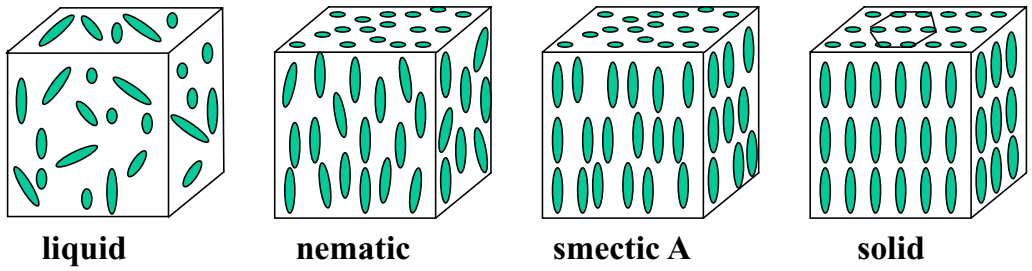

Figure 3.1: This phase cartoon depicts an increasing degree of order from left to right. Liquids clearly lack any positional or orientational order. The nematic liquid crystalline phase lacks positional order but has orientational order. The smectic-A liquid crystalline phase has molecules arranged in layers. Despite the layer structure, the phase lacks positional order within a given layer; however there is orientational order perpendicular to the layer. Finally, solids have both positional and orientational order in all three dimensions.

oriented within each layer and do not move between layers. Figure 3.1 shows a structural model of this smectic mesophase. The molecules lie with their long axes parallel in layers. The molecules can move relative to each other, and consequently several types of smectic structures can be formed depending upon the inclination of the long axes of the molecules to the plane of the layers.

The nematic phase also has molecules with their long axes parallel, but they are not separated into layers. Rather, their structural arrangement is similar to the ordinary packing of toothpicks in a box. Figure 3.1 depicts such a nematic mesophase structure. While maintaining their orientation, the individual molecules can translate freely up and down.

The cholesteric mesophase can be defined as a special type of the nematic phase (chiral nematic) in which the thin layers (one molecule thick) of mostly parallel molecules have their longitudinal axes twisted (rotated) in adjacent layers at a defined angle. Each layer is basically a nematic structure. The axes of alignment of contiguous layers differ by

a small angle and produce a helix or progressive rotation of many layers in an LC material.

3.1.3 Magnetic Properties

The liquid crystalline phase alone is a very interesting physical system due to the unique macroscopic properties of the system as determined by the microscopic structure of the individual molecules. The structure of liquid crystal molecules also determines their response to an applied magnetic field. Although the intermolecular interactions might be expected to significantly contribute to the system's response to a magnetic field, magnetic properties are only weakly influenced by intermolecular interactions. Thus, the magnetic response for non-ferromagnetic materials is simply the sum of the individual molecular responses. The net magnetic properties of liquid crystal molecules are determined by their electronic structure and can be characterized by their magnetic susceptibility. A negative magnetic susceptibility is characteristic of a diamagnetic response, a positive susceptibility is indicative of a paramagnetic response, and a permanent magnetization is indicative of ferromagnetism. Both diamagnetic and paramagnetic liquid crystals are well known, and even some ferromagnetic liquid crystals have been prepared[14].

Since the magnetic properties of liquid crystals are directly related to their molecular structure and this structure is anisotropic, the uniform alignment of liquid crystal molecules can be induced by utilizing this magnetic susceptibility anisotropy. Macroscopically, this magnetic susceptibility induces a net magnetization referred to as **M** when placed in a magnetic field **B** as given below:

$$M_\alpha = \mu_0^{-1} \chi_{\alpha\beta}^{mag} B_\beta \tag{3.2}$$

where μ_0 is the permeability of free space and $\chi_{\alpha\beta}^{mag}$ is the magnetic susceptibility. The free energy density due to the magnetization is then:

$$\begin{aligned} g_{mag} &= -\int B_\alpha dM_\alpha \\ &= -\mu_0^{-1}\int B_\alpha \chi_{\alpha\beta} dB_\beta \\ &= g_0 - \frac{1}{2}\mu_0^{-1}\chi_{\alpha\beta}B_\alpha B_\beta. \end{aligned} \tag{3.3}$$

The susceptibility, $\chi_{\alpha\beta}$, has the symmetry of the material, so expressing it in the principle axes of χ gives:

$$\begin{aligned} g_{mag} &= g_0 - \frac{1}{2}\mu_0^{-1}(\chi_\parallel B_\parallel^2 + \chi_{\perp'} B_{\perp'}^2 + \chi_\perp B_\perp^2) \\ &= g_0 - \frac{1}{2}\mu_0^{-1}(\chi_\parallel \cos^2\theta + \chi_{\perp'}\sin^2\theta\sin^2\phi + \chi_\perp \sin^2\theta\cos^2\phi) \end{aligned} \tag{3.4}$$

where θ and ϕ are polar angles defining the orientation of $\mathbf{B}$ with respect to the principal axes of the susceptibility. For a uniaxial material $\chi_{\perp'} = \chi_\perp$ and:

$$\begin{aligned} g_{mag} &= g_0 - \frac{1}{2}\mu_0^{-1}B^2(\chi_\perp + \Delta\chi\cos^2\theta) \\ &= g_0 - \frac{1}{2}\mu_0^{-1}B^2\chi_\perp - \frac{1}{2}\mu_0^{-1}\Delta\chi(\mathbf{B}\cdot\mathbf{n})^2. \end{aligned} \tag{3.5}$$

where $\Delta\chi = \chi_\perp - \chi_\parallel$ and $\vec{n}$ is the director defining the principal axis for the susceptibility for uniaxial materials. Eq. (3.5) shows the effect of the sign of $\Delta\chi$. When $\Delta\chi$ is positive the director aligns parallel to the magnetic field to minimize the free energy, and if $\Delta\chi$ is negative, the director aligns perpendicular to the magnetic field.

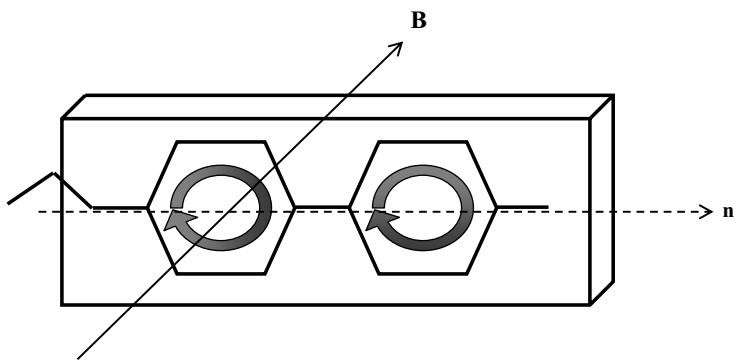

Figure 3.2: Simple example of how a liquid crystal mesogen responds to an applied magnetic field. Here the induced ring currents generate a field in opposition to the applied field, thus the molecule tends to align to minimize its free energy.

The magnetic field aligning mechanism of the liquid crystal can be thought of as a current induced in the bonding electrons of the nematogen which in turn generate an opposing magnetic field according to the structure of the molecule. Typically, liquid crystal molecules have aromatic groups which provide a large diamagnetic susceptibility for the molecule as pictorially represented in Figure 3.2. The director $\vec{n}$ of Figure 3.2 will then align according to Eq. 3.5 in order to minimize the free energy of the system.

3.1.4 Order Parameter

One of the most important aspects of an oriented liquid crystalline system is being able to quantitatively describe the degree to which the system is aligned. This quantification is required if the static NMR observables are to be accurately determined from the oriented phase. Although determining the 3D alignment tensor appears to be a daunting task, it can become more tractable by utilizing symmetry and the available observable interactions.

First we must develop a description of how to relate the molecule fixed frame to the laboratory frame. The Zeeman interaction favors representation in the laboratory

frame with axes represented as X,Y,Z. However, many of the interesting interactions in NMR have different principal axes more closely related to the molecular structure such as CSA, dipolar couplings and the quadrupolar interaction. It is more convenient to formulate these interactions in the molecule fixed frame of x,y,z; however, this does require a frame transformation. Of all of the tensors that occur in the high-field approximation, only the ZZ components play an important role. Thus we perform the transformation given below:

$$A_{ZZ} = \sum_{\alpha,\beta} \cos\theta_{Z,\alpha} \cos\theta_{Z,\beta} A_{\alpha\beta} \tag{3.6}$$

where the quantity $\cos\theta_{Z,\alpha}$ is the cosine of the angle between the laboratory-fixed Z-axis and the molecule-fixed α-axis ($\alpha, \beta = x, y, z$).

For any system, we wish to determine how the molecular axis system is tumbling in terms of the laboratory axis system. Since the molecule is tumbling in the laboratory frame, we must perform an ensemble average over all of the tumbling angles. This ensemble average is referred to as the Saupe orientation tensor[15, 16], $S_{\alpha\beta}$:

$$S_{\alpha\beta} = \frac{1}{2}\langle 3\cos\theta_{Z,\alpha}\cos\theta_{Z,\beta} - \delta_{\alpha\beta}\rangle \tag{3.7}$$

where the brackets denote the ensemble average and $\delta_{\alpha\beta}$ is the Kronecker delta function. From Eq. (3.7) it can be derived that the tensor is both symmetric and traceless:

$$S_{\alpha\beta} = S_{\beta\alpha} \tag{3.8}$$

$$\sum_{\alpha} S_{\alpha\alpha} = 0. \tag{3.9}$$

Utilizing spherical coordinates where the Z-axis makes an angle θ with the z-axis and the projection of the Z-axis onto the xy-plane makes an angle ϕ with the positive x-axis, we obtain:

$$\begin{aligned}
S_{xx} &= \frac{1}{2}\langle 3\sin^2\theta\cos^2\phi - 1\rangle \\
S_{yy} &= \frac{1}{2}\langle 3\sin^2\theta\sin^2\phi - 1\rangle \\
S_{zz} &= \frac{1}{2}\langle 3\cos^2\theta - 1\rangle \\
S_{xy} &= \frac{3}{2}\langle 3\sin^2\theta\sin\phi\cos\phi\rangle \\
S_{xz} &= \frac{3}{2}\langle 3\sin\theta\cos\theta\cos\phi\rangle \\
S_{yz} &= \frac{3}{2}\langle 3\sin\theta\cos\theta\sin\phi\rangle. \qquad (3.10)
\end{aligned}$$

The values of these elements vary in the ranges:

$$-\frac{1}{2} \leq \quad S_{xx}, S_{yy}, S_{zz} \quad \leq 1 \qquad (3.11)$$

$$-\frac{3}{4} \leq \quad S_{xy}, S_{xz}, S_{yz} \quad \leq \frac{3}{4}. \qquad (3.12)$$

In the isotropic tumbling case, all of the elements of the S-tensor are zero:

$$\int_0^{\pi}\int_0^{2\pi} S_{\alpha\beta}\sin\theta d\theta d\phi = 0, \qquad (3.13)$$

and $S_{\alpha\beta} \neq 0$ for anisotropic tumbling.

3.2 Partially Averaged Observables

Utilizing the S-tensor we wish to rewrite the relevant Hamiltonians in a more convenient form to take into account molecular tumbling. The chemical shielding is now:

$$\sigma_{ZZ} = \frac{1}{3}(\sigma_{11} + \sigma_{22} + \sigma_{33}) + \frac{2}{3}\sum_{\alpha,\beta} S_{\alpha\beta}\sigma_{\alpha\beta}. \tag{3.14}$$

The isotropic term remains:

$$\sigma^{iso} = \frac{1}{3}(\sigma_{11} + \sigma_{22} + \sigma_{33}), \tag{3.15}$$

and the averaged anisotropic part is:

$$\sigma_{ZZ} - \sigma^{iso} = \sigma^{aniso'} = \frac{2}{3}\sum_{\alpha,\beta} S_{\alpha\beta}\sigma_{\alpha\beta}. \tag{3.16}$$

The chemical shift Hamiltonian of Eq. (2.18) must now be rewritten in the common molecule-fixed frame:

$$H_{CS} = -\omega_0(\sigma^{iso} + \sigma^{aniso'})I_Z. \tag{3.17}$$

Similar to the chemical shielding, the averaged indirect spin-spin coupling is:

$$J_{ij,ZZ} = J_{ij}^{iso} + \frac{2}{3}\sum_{\alpha\beta} S_{\alpha\beta}J_{ij,\alpha\beta} = J_{ij}^{iso} + J_{ij}^{aniso'}. \tag{3.18}$$

Eq. (2.23) can be rewritten as:

$$H_J = J_{ij}^{iso}[I_{i,Z}I_{j,Z} + \frac{1}{2}(I_{i,+}I_{j,-} + I_{i,-}I_{j,+})]$$
$$+J_{ij}^{aniso'}[I_{i,Z}I_{j,Z} - \frac{1}{4}(I_{i,+}I_{j,-} + I_{i,-}I_{j,+})] \tag{3.19}$$

or alternatively as:

$$H_J = J_{ij}^{iso}\mathbf{I_i} \cdot \mathbf{I_j} + J_{ij}^{aniso'}[I_{i,Z}I_{j,Z} - \frac{1}{4}(I_{i,+}I_{j,-} + I_{i,-}I_{j,+})]. \tag{3.20}$$

Dipolar coupling has no isotropic component. Therefore the averaged interaction is written as:

$$D_{ij,ZZ} = D_{ij}^{aniso'} = \frac{2}{3}\sum_{\alpha\beta} S_{\alpha\beta}D_{ij,\alpha\beta}, \tag{3.21}$$

and from Eq. (2.27) we have:

$$D_{ij,\alpha\beta} = \frac{\gamma_i\gamma_j h}{8\pi^2 r_{ij}^3}(3\cos\theta_{ij,\alpha}\cos\theta_{ij,\beta} - \delta_{\alpha\beta}). \tag{3.22}$$

Therefore, the dipolar Hamiltonian is now:

$$H_D = 2D_{ij}^{aniso'}[I_{i,Z}I_{j,Z} - \frac{1}{4}(I_{i,+}I_{j,-} + I_{i,-}I_{j,+})]. \tag{3.23}$$

Similarly, the observable quadrupolar interaction is :

$$q_{ZZ} = q^{aniso'} = \frac{2}{3}\sum_{\alpha\beta} S_{\alpha\beta}q_{\alpha\beta}, \tag{3.24}$$

and the averaged quadrupolar Hamiltonian is:

$$H_Q = \frac{q^{aniso'}}{4I(2I-1)}(3I_Z^2 - I^2). \tag{3.25}$$

In summary, for the total Hamiltonian we have:

$$\begin{aligned} H = & - \sum_i \omega_{i,0}(1 - \sigma_i^{iso} - \sigma_i^{aniso'})I_{i,Z} \\ & + \sum_{i<j} J_{ij}^{iso}\mathbf{I}_i \cdot \mathbf{I}_j \\ & + \sum_{i<j} 2D_{ij}^{aniso'} + J_{ij}^{aniso'}[I_{i,Z}I_{j,Z} - \frac{1}{4}(I_{i,+}I_{j,-} + I_{i,-}I_{j,+})] \\ & + \sum_i \frac{q_i^{aniso'}}{4I_i(2I_i-1)}(3I_{i,Z}^2 - I_i^2). \end{aligned} \tag{3.26}$$

3.3 Recent Approaches

Now that the basic principles of NMR in liquid crystals have been thoroughly discussed, the experimental abilities and difficulties will be discussed below. The first thing to note is what happens to the NMR spectrum of a molecule when it is dissolved in an anisotropic phase such as a liquid crystal. As shown in Figure 3.4, the ^{19}F spectrum of a very simple molecule such as C_6F_5Cl which would normally exhibit three chemical shifts in the ratio of 2:1:2 for the ortho:meta:para becomes extremely complex. Analysis of a spectrum such as the one presented in Figure 3.4 would be incredibly difficult without some information to help simplify the problem. Many NMR spectroscopists have studied different methods to provide simplification of the 1D spectrum; these efforts will be briefly described below.

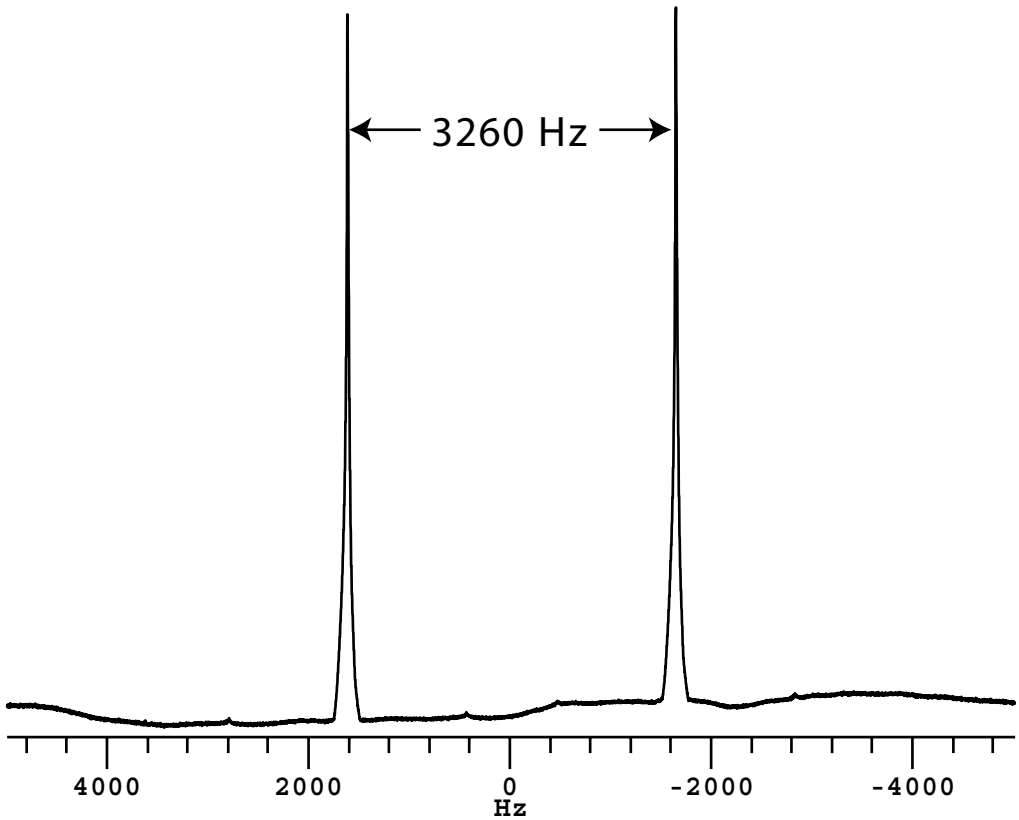

Figure 3.3: 1D ^{1}H spectrum of methylene chloride (CH_2Cl_2) dissolved in the liquid crystal I52

3.3.1 Simple One-Dimensional Experiments

For molecules such as methylene chloride (CH_2Cl_2) spectral interpretation is very straightforward. In Figure 3.3, instead of the expected single proton resonance observed in isotropic solution, we see two peaks split by several kilohertz due to the non-zero dipolar coupling between the methylene protons when methylene chloride is dissolved in a LC solvent. Although the spectrum of Figure 3.3 is extremely simple and easy to interpret, the complexity of the spectrum rapidly increases when the number of coupling nuclei increases. The upper limit for the level of complexity is determined by the number of single quantum

transitions (Z_1) from the expression[17, 18, 19]:

$$Z_1 = \begin{pmatrix} 2N \\ N+1 \end{pmatrix} = \frac{2N!}{(N+1)!(N-1)!} \tag{3.27}$$

where N is the number of spins. For N=4 this number is 56, for N=8 it is 11,440 and for N=12 is 2,496,144. Clearly for molecules with more than a few spins, the number of transitions is too large and the spectrum too complex for interpretation. For example, only recently has the spectrum of ethylbenzene in a liquid crystal been fully assigned and the structure determined from the analysis of the 1D spectrum[20]. However, in the case of ethylbenzene, the analysis was performed with the aid of several simplifications including deuteration to reduce the strength of some of the couplings (the γ of ^{2}H is a fraction of ^{1}H). Another simplification utilized was the implementation of multiple quantum spectroscopy which is discussed further below.

3.3.2 Multiple Quantum

One of the most exciting advances in the NMR of complex spin systems was the utilization of multiple quantum (MQ) spectroscopy. In MQ spectroscopy, a complex spectrum can be simplified by observing transitions other than the single quantum single spin flip; instead, the signal that results from several simultaneous spin flips is observed[18, 21]. In general, as the number of observed quanta, n, is increased, the spectrum is simplified

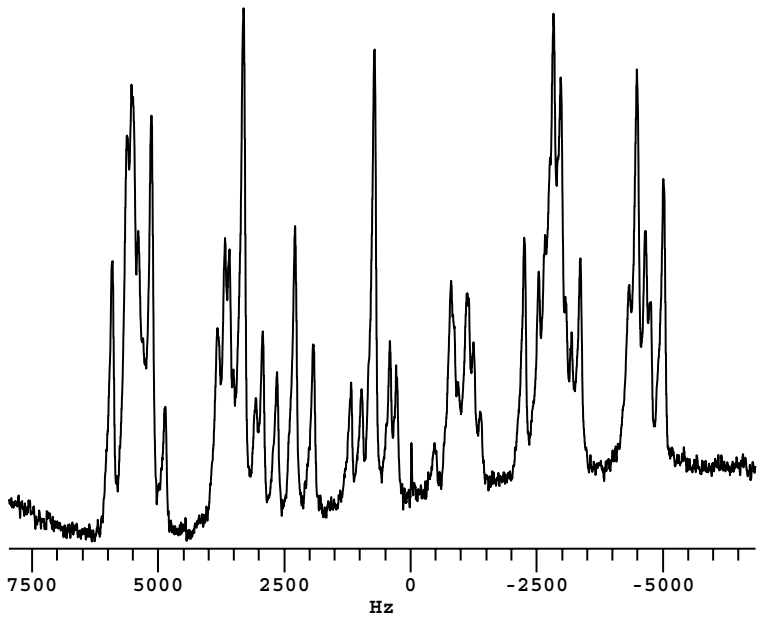

Figure 3.4: 1D ^{19}F NMR spectrum of C_6F_5Cl in the liquid crystal I52

due to the reduced number of transitions. Generalizing Eq. (3.27) for n-quanta we see:

$$Z_n = \begin{pmatrix} 2N \\ N+n \end{pmatrix} = \frac{2N!}{(N+n)!(N-n)!}. \tag{3.28}$$

For example, a six-quantum spectrum of benzene in an oriented system obtained using TPPI (time proportional phase incrementation) [21] would have only a single peak, the five-quantum would yield two peaks, seven four-quantum peaks would exist, and so forth. However, these n-quantum spectra require a difficult analysis for full interpretation since the observed signal is the product of the couplings and chemical shifts of all of the nuclei involved in the transition; thus, this again becomes a daunting task. Instead we turn to a heteronucleus to aid in simplification of the coupled spectrum described below.

3.3.3 Local Field

Another exciting advance in the determination of couplings, termed separated local field (SLF)[22] experiments, utilizes the fact that a rare spin of type S (e.g. ^{13}C) among many strongly coupled abundant spins of type I (e.g. ^{1}H) can 'feel' the couplings of each abundant I-spin if the homonuclear I-I couplings are turned off. In this manner, a 2D correlation is obtained where each S-spin resonance is resolved along with every I-S coupling to that particular S-spin.

This method was then further developed[17] to simplify interpretation of the coupling even more by detecting the I-spins directly after the indirect evolution of the local-field. This new method called proton detected local field (PDLF) improves upon the local field idea by reducing the number of lines from 2^N, as observed in the SLF experiment, to $2N$ lines; this effectively changes the situation from one of exponentially increasing complexity to a *linear* situation.

These types of experiments are ideal for hydrocarbon samples where natural abundance carbon signal would ensure the dilute nature of the S-spin, and the protons would be the I-spins. However, to date this method has been utilized only to a limited degree. This is presumably due to the requirement that the simplification only truly applies in samples such as liquid crystals where the observed dipolar coupling is isotropic and thus each coupling is a doublet instead of an anisotropically broadened line as would be observed in the solid state.

A demonstration of the type of interesting spectra that the PDLF method provides is shown in Figure 3.6 which was obtained using the pulse sequence of Figure 3.5. In

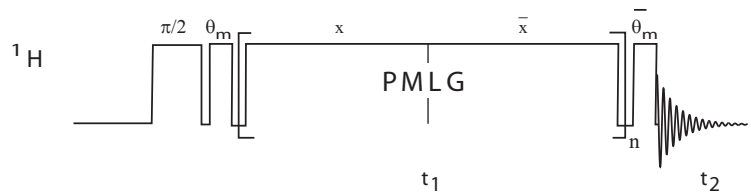

Figure 3.5: Proton Detected Local Field Pulse Sequence with PMLG Decoupling used to acquire the 2D spectrum of Figure 3.6

Figure 3.5, the section labeled PMLG refers to the homonuclear decoupling sequence called phase modulated Lee-Goldburg (PMLG)[23] whose effect is to eliminate the proton-proton couplings in the indirect t_1 dimension. The effects of this technique on our model system, dichlorofluoronitrobenzene ($C_6H_2Cl_2FNO_2$), is shown in Figure 3.6. The vertical axis in Figure 3.6 is the directly detected dimension which has a large ^1H_A-^{19}F dipolar coupling that produces the outer two doublets. The doublet structure of the ^1H_A resonance is due to the ^1H_A-^1H_B coupling from across the benzene ring. The inner quartet seen on the vertical axis then is from the ^1H_B-^1H_A coupling and the much weaker ^1H_B-^{19}F. This information can be inferred from knowing the structure of the molecule. However, with the addition of the horizontal local field dimension in Figure 3.6, we have an additional dimension free of the ^1H_A-^1H_B couplings; this allows the spin states of all of the coupling nuclei to be readily observed from the contour plot.

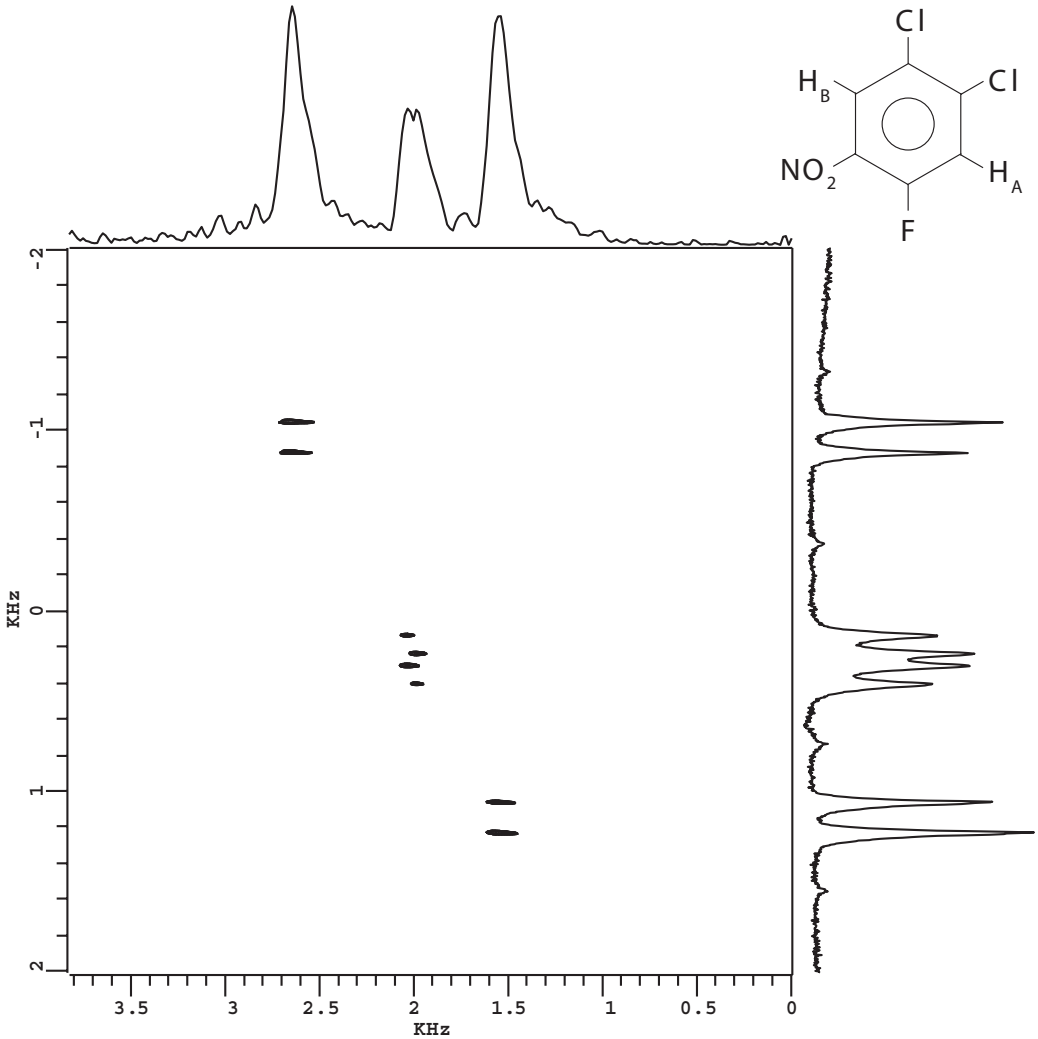

Figure 3.6: Proton Detected Local Field 2D Spectrum of $C_6H_2Cl_2FNO_2$ in a nematic liquid crystal

Chapter 4

Dynamic Director Experiments in Liquid Crystals

4.1 Introduction Director Alignment

4.1.1 Advantages of Oriented Systems

Anisotropic interactions, such as dipolar couplings, have long provided a means for extracting structure from molecules using nuclear magnetic resonance (NMR)[2, 24]. Traditional structural methods in liquid state NMR measure dipolar couplings via the nuclear Overhauser effect (NOE) and use this information to solve three-dimensional structures in isotropic solutions[25, 26]. The NOE method in liquids quantifies the cross-relaxation rate due to dipolar coupling to extract $1/r^6$ distance information; methods in solid state NMR are able to directly measure dipolar couplings with a $1/r^3$ dependence [27]. Although structure determinations using NOEs in isotropic solution have been fruitful, the $1/r^6$ distance

constraints can be structurally limiting. Ideally, the $1/r^3$ dependence of dipolar coupling that is observed in solids could provide valuable structural constraints without the lower resolution typically seen in the solid state. The high-resolution observed in liquid state NMR is the result of isotropic molecular tumbling which averages the anisotropic interactions to zero. However, in the solid state the lack of isotropic motion gives rise to convoluted broad lines resulting from the presence of these anisotropic interactions. In oriented liquid crystals, anisotropic interactions, such as dipolar couplings, are only partially averaged. This averaging gives rise to well resolved, sharp lines that can yield valuable structural information.

The unique nature of the oriented liquid crystalline phase has provided an interesting realm for the study of anisotropic magnetic interactions in NMR [28, 29, 30]. These phases are aligned by an applied magnetic field while the individual molecules tumble about a magnetic alignment axis called a director and labeled $\vec{n}$ in Figure 4.1. This molecular tumbling property of liquid crystals yields an environment where anisotropic NMR interactions can be observed to a reduced degree while maintaining the high resolution found in the liquid state, see Figure 4.2.

Recent advances in the availability of reliable liquid crystalline phases have catalyzed the measurement of dipolar couplings in routine protein structure determinations where they are referred to as '*residual* dipolar couplings'[31]. The liquid crystalline systems commonly used for residual dipolar coupling determinations are intentionally prepared to only weakly align in the magnetic field. This weak alignment only reveals weak dipolar couplings between directly bonded nuclei that can be easily interpreted as a small splitting (∼5-10 Hz). This is in contrast to strongly aligned systems where the spectrum becomes

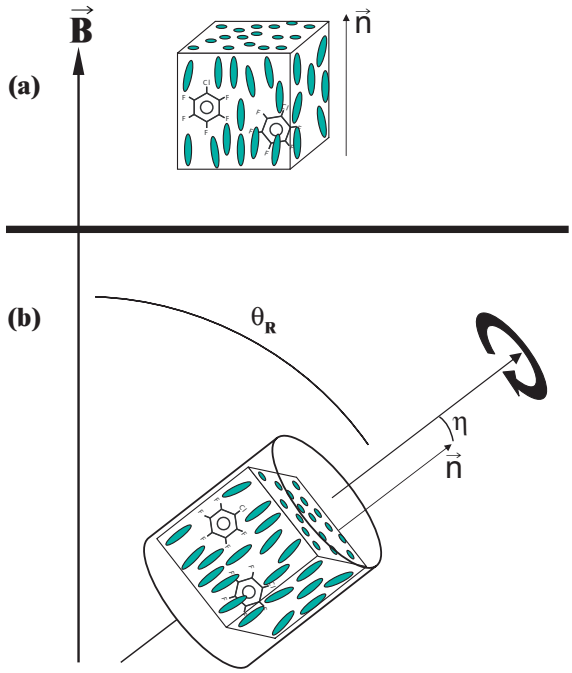

Figure 4.1: (a) Cartoon of the oriented liquid crystalline sample with the rods representing the liquid crystal molecules which align the solute molecule C_6F_5Cl in the direction of the director $\vec{n}$. (b) The effect of sample spinning on the oriented sample. The angle θ_R denotes the spinning axis angle and η is the angle between the spinning axis and the director.

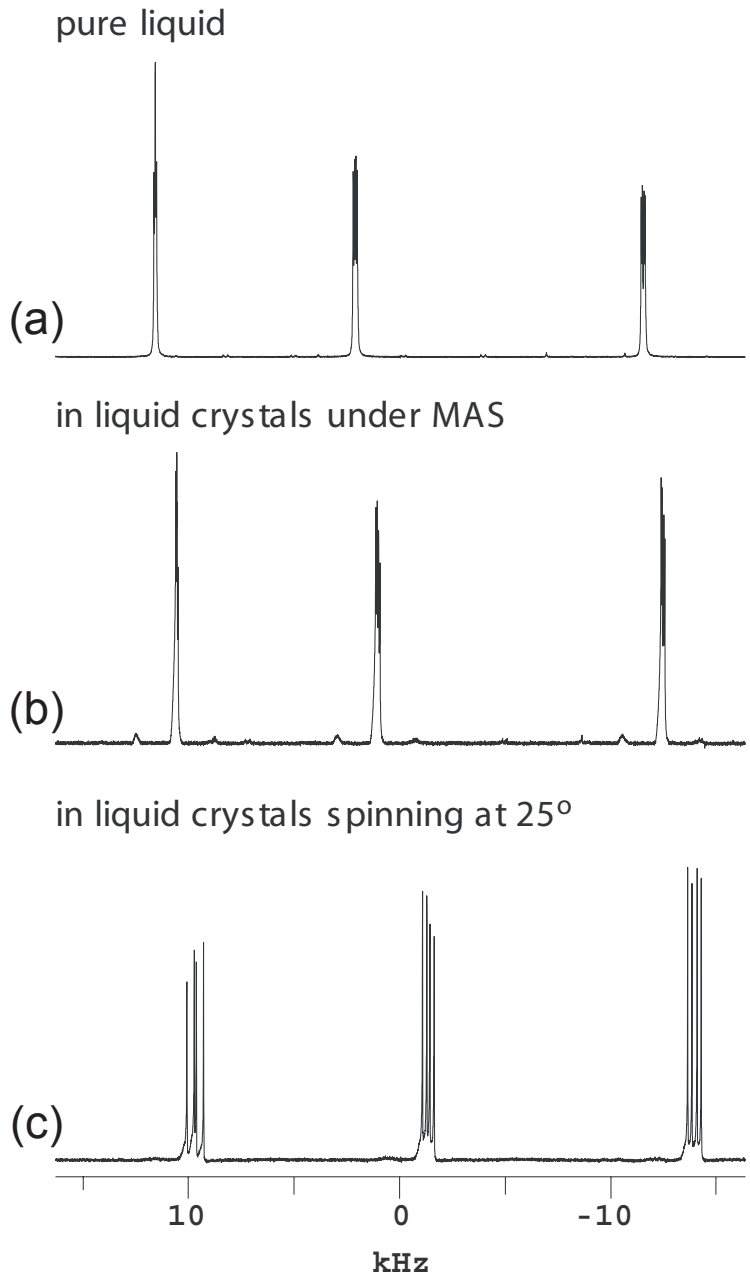

Figure 4.2: One-dimensional ^{19}F spectra of (a) neat C_2F_3I, (b) MAS of C_2F_3I dissolved in a nematic liquid crystal spinning at 2 kHz, and (c) same sample as in (b) spinning at $\theta_R = 25°$.

exponentially more complex with an increase in the strength and number of coupled spins. However, strongly oriented systems can potentially provide valuable structural information via measurable couplings from nuclei separated by more than a single bond. If the long range couplings are measurable despite the increased spectral complexity, they provide strong geometrical constraints for use in three-dimensional structure determinations. Clearly, it is beneficial to utilize a more strongly orienting system if possible; however we must make efforts to simplify and facilitate interpretation of the increasingly complex dipolar coupled spectrum.

Examples of even simple molecules such as C_6F_5Cl in a strongly aligned liquid crystal have observable ^{19}F-^{19}F dipolar couplings on the order of kHz. When the observed couplings approach the chemical shift differences of the coupled nuclei, the $1/r^3$ structural information from the dipolar couplings is lost in a complex spectrum such as shown in Figure 4.3a. When there exist strong homonuclear couplings between several nuclei, as in Figure 4.3a, the system is termed second order or strongly-coupled and is a complex spin system that is difficult to both interpret and manipulate[27]. However, if the dipolar couplings are reduced to values smaller than their chemical shift differences, the useful structural information can be easily read from the spectrum, as shown in Figure 4.3b; this is what is termed a 'first order' type spectrum. The challenge in structure determination is the fact that the structurally important couplings are often weak and masked by shorter range dipolar couplings; thus we must attempt to introduce couplings as strongly as possible while maintaining interpretability.

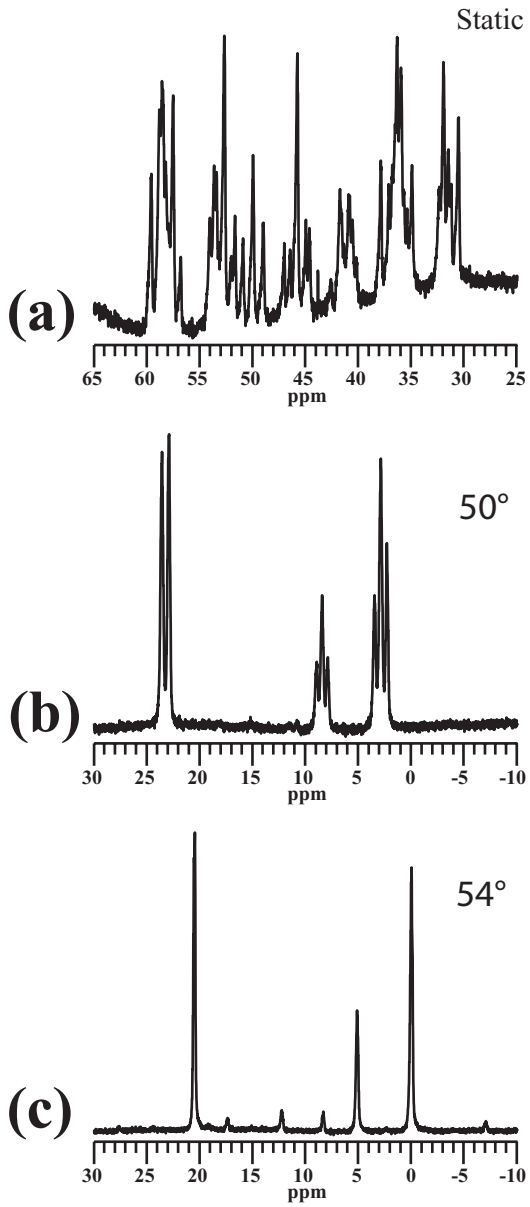

Figure 4.3: ^{19}F spectrum of C_6F_5Cl in the nematic liquid crystal I52 15% w/w obtained (a) without sample spinning, (b) with sample spinning at 50°, and (c) under magic angle spinning. Spectra are shown in ppm from a reference frequency of 376.086 MHz.

4.1.2 Techniques for Simplifying Spectra

Currently, a number of techniques exist that aid in the analysis and simplification of coupled systems. However, most of them have difficulty in dealing with second order type systems. Perhaps the most promising group of existing methods that are capable of dealing with second order systems are the heteronuclear local field experiments[17, 32]. Although heteronuclear dipolar couplings provide a first order type spectrum with the aid of homonuclear decoupling methods, the presence of more than one coupling can complicate interpretation. In order to keep the interpretation of the dipolar couplings tractable, their strength must remain minimal. This weak coupling requirement limits measurement to directly bonded atoms and provides limited structural information; this is in contrast to long range couplings that can yield excellent constraints in structure determinations.

In an effort to utilize more strongly dipole coupled liquid crystalline samples, several multiple pulse experiments have been developed which reduce[33]or even eliminate[34] homonuclear dipolar couplings to an extent which makes spectral interpretation viable. These methods perform well even in strongly coupled systems and possess only a modest scaling factor. Instead of employing RF pulses to reduce dipolar couplings, it is also possible to simplify dipolar couplings in liquid crystals by reorienting the alignment director whereby the intrinsic molecular motion performs the averaging[35, 36, 37, 38]. Director reorientation methods have no associated scaling factor and work well even in strongly coupled systems.

It has been shown that the alignment of the liquid crystal director can be manipulated readily with spinning according to the properties of the liquid crystal and the spinning angle[39, 40]. Depending upon the anisotropy of the diamagnetic susceptibility ($\Delta\chi$) of the

liquid crystal[37]and the spinning angle with respect to the magnetic field, θ_R, the director of the liquid crystalline phase will align parallel or perpendicular to the spinning axis. For example, in a liquid crystal sample with $\Delta\chi > 0$, as is the case with the sample studied in this work, the director aligns parallel to the spinning axis in the angle range of $\theta_R = 0°$ to $54.7°$ and perpendicular in the range of $54.7°$ to $90°$. Therefore, in the appropriate spinning angle range, the alignment and thus the averaging of interactions in the sample can be controlled.

The motivation for developing methods to simplify and facilitate the interpretation of spectra of molecules in an oriented liquid crystalline phase is clearly shown in the one-dimensional (1D) spectrum in Figure 4.3a. Although there is some resolution of peaks in the dipole coupled ^{19}F spectrum of oriented C_6F_5Cl, discerning the three chemical shifts and ten dipolar couplings is extremely difficult. The level of complexity in Figure 4.3a approaches the upper limit of 210 possible single quantum transitions (Z_1) from the expression[41, 17]:

$$Z_1 = \begin{pmatrix} 2N \\ N+1 \end{pmatrix} = \frac{2N!}{(N+1)!(N-1)!} \tag{4.1}$$

where N is the number of spins. A complete analysis of this spectrum would require a lengthy fitting routine that may or may not converge to the correct spectral parameters for δ^{aniso}, D_{ij}^{aniso}, and $S_{\alpha\beta}$. The order parameter, $S_{\alpha\beta}$, describes the molecular motions of the molecules in the liquid crystalline phase and can be thought of as representing the average molecular orientation in the phase. Further details on the orientational order parameter

can be found elsewhere[15, 16]. $S_{\alpha\beta}$ is defined by:

$$S_{\alpha\beta} = \frac{1}{2}\langle 3\cos\theta_\alpha \cos\theta_\beta - \delta_{\alpha\beta}\rangle \tag{4.2}$$

where $\theta_\chi(\chi = x, y, z)$ is the angle between the director and the molecular χ-axis and $\delta_{\alpha\beta}$ is the Kronecker delta function (1 if $\alpha = \beta$, 0 if $\alpha \neq \beta$). The dipolar coupling in the molecular frame is:

$$D^{MOL}_{ij,\alpha\beta} = -\frac{h\gamma_i\gamma_j}{2\pi r^3_{ij}}(3\cos\theta_{ij,\alpha}\cos\theta_{ij,\beta} - \delta_{\alpha\beta}) \tag{4.3}$$

where $\theta_{ij,\chi}$ is the angle between the internuclear vector and the molecular χ axis, γ_i and γ_j are the magnetogyric ratios of the two nuclei, and r_{ij} is the internuclear distance. The remaining anisotropic component of the dipolar coupling, D^{aniso}_{ij}, now depends upon the order parameter matrix, $S_{\alpha\beta}$, and $D^{MOL}_{ij,\alpha\beta}$:

$$D^{aniso}_{ij} = \frac{2}{3}\sum_{\alpha\beta} S_{\alpha\beta} D^{MOL}_{ij,\alpha\beta}. \tag{4.4}$$

In the case of C_6F_5Cl, we assume the molecule is rigid so that r_{ij} of Eq. (4.3) is constant. The chemical shift in an anisotropic phase is actually the sum of the isotropic and anisotropic chemical shifts:

$$\delta^{obs} = \delta^{iso} + \delta^{aniso} = \delta^{iso} + \frac{2}{3}\sum_{\alpha,\beta} S_{\alpha\beta}\delta_{\alpha\beta} \tag{4.5}$$

where $\delta_{\alpha\beta}$ are the elements of the chemical shift anisotropy tensor in the molecule fixed frame. Normally, both the isotropic and anisotropic J coupling would provide additional contributions to consider in the spectral analysis. However, since the J coupling was not

observable in this sample, it's nominal contribution is not discussed further. If the order parameter can be determined, anisotropic information about the molecules can be immediately derived from the two observables δ^{obs} and (to first order) D_{ij}^{aniso} from the relationships in Eqns. (4.4) and (4.5). However, as the spin system becomes more complex, assignment is difficult and these relationships are less obvious.

Instead of employing a brute-force approach to the interpretation of a spectrum such as in Figure 4.3a, the spectrum can be simplified first into more tractable portions. In addition to the scaling of interactions resulting from $S_{\alpha\beta}$, the anisotropic components of D_{ij}^{aniso} and δ^{obs} can be further scaled if the director is aligned at an angle θ_R with the magnetic field[37]. With the liquid crystal directors reoriented, Eqns. (4.4) and (4.5) become:

$$\delta^{obs} = \delta^{iso} + \frac{1}{2}(3\cos^2\theta_R - 1)\delta^{aniso} \tag{4.6}$$

$$D_{ij}^{obs} = \frac{1}{2}(3\cos^2\theta_R - 1)D_{ij}^{aniso}. \tag{4.7}$$

For first order couplings this dependence is observed in Figure 4.4.

This scalability of the anisotropic interactions requires that the director axis is single-valued with respect to the magnetic field. Since the liquid crystal solvent I52 has the property of positive magnetic susceptibility anisotropy[42], the liquid crystal director aligns parallel to the spinning axis at angles $0° < \theta_R < 54.7°$[37]. Thus by simply rotating the spinning axis to 50° with respect to the applied magnetic field, the dipolar couplings are scaled by the factor $\frac{1}{2}(3\cos^2 50° - 1)$, and a first order type spectrum is obtained. This reduction of strong second order dipolar couplings to simple first order couplings is readily

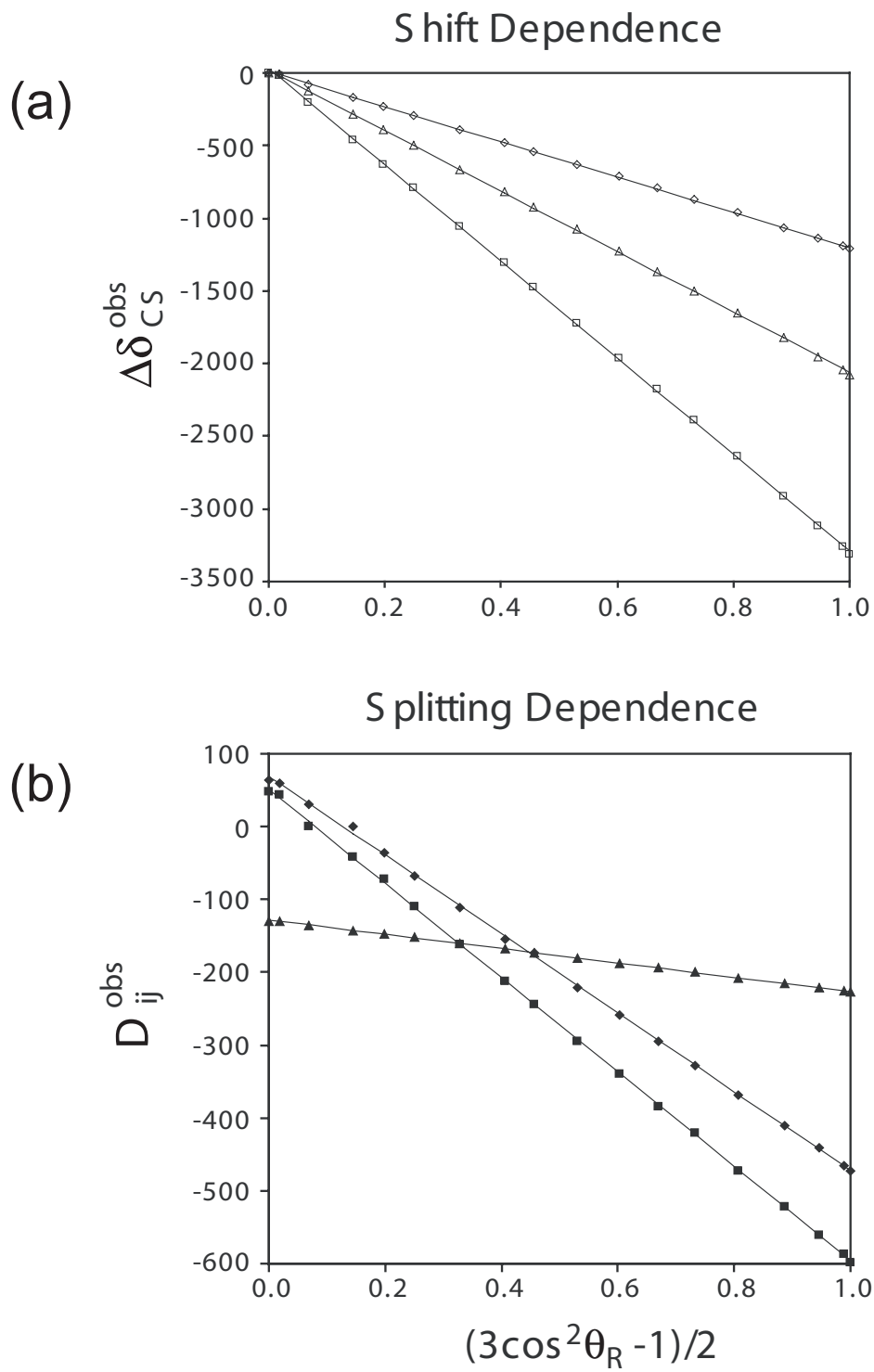

Figure 4.4: The dependence of the (a) dipolar splitting and (b) of the chemical shift as a function of $(3\cos^2\theta_R - 1)/2$.

seen in Figures 4.3a and 4.3b. At a spinning angle of 50°, the measured splittings are 250 Hz for the ortho-meta coupling and 195 Hz for the two meta-para couplings. Although scalar couplings could contribute to the observed splittings, the three bond scalar couplings were not observable, as shown in the isotropic spectrum of Figure 4.3c. In addition, the dipolar splitting of the single ^{19}F of the solvent liquid crystal was also observed with a splitting of 1085 Hz (not shown in Figure 4.3).

Figure 4.3c demonstrates how a second order spectrum can be reduced to an isotropic spectrum by spinning at the magic angle. With the nematic director aligned at the magic angle, the sample spinning provides the appropriate mechanism to align the liquid crystal director, and it is actually the uniaxial motion of the liquid crystal about the magic angle that averages the dipolar couplings to zero. Since the liquid crystal motion is much faster than the 4.5 kHz spinning speed, the effectiveness of the averaging is much greater than could be obtained with spinning of a solid crystalline sample.

4.2 Variable Angle Spinning (VAS) Experiments

By reorienting the director at various angles, we obtain information regarding the anisotropic interactions of the system. This information can be used to deduce the structure of molecules dissolved in the liquid crystalline phase. The observed ortho, para, and meta ^{19}F isotropic chemical shifts of perfluorocholorbenzene in I52 are 0.0, 5.1 and 20.5 ppm with intensity ratios of 2:1:2 referenced to 376.073058 MHz on a spectrometer where TMS (tetramethylsilane) resonates at 399.74179 MHz. The isotropic shifts reported were obtained from Figure 4.3c where the sample's director is oriented at the magic angle. In

addition to the isotropic resonances, small peaks appear in the spectrum that are due to spinning sidebands[43] occurring at integer multiples of the spinning frequency (ω_R). The spinning sidebands are the result of domains that are not aligned with the spinning axis; their anisotropic interactions then become time dependent with the rotor frequency. Due to the $\frac{1}{2}(3\cos^2\theta_R - 1)$ dependence of the aligning force, at exactly the magic angle, there is no favorable alignment direction. Thus some liquid crystal domains begin to form a random powder-type spectrum which results in spinning sidebands. These sidebands can be avoided by spinning at the magic angle for short times or at angles near the magic angle ($< 0.5°$ away).

4.2.1 Scaling Couplings: Second Order, First Order, Isotropic

Figure 4.5 demonstrates the scalability of the dipolar couplings from second order to first order and ultimately to the isotropic spectrum. The isotropic spectrum obtained at 54° has the resonances indicated with arrows to the perfluorochlorobenzene molecule. The resonance furthest downfield arises from a single ^{19}F in the I52 liquid crystal solvent. Although this background solvent resonance has a measurable splitting at angles near the magic angle, the peak quickly broadens and shifts out of the spectral window and is folded into the opposite side causing a rolling baseline. The broadening of this peak is not the result of couplings to the perfluorochlorobenzene but is instead the result of couplings to the numerous protons in the I52 liquid crystal molecules. Of more interest is what happens to the resonances from the perfluorocholorbenzene.

Examining the first order data in the angle range of 54° to 45°, we are able to extract some information about the anisotropic interactions. However, even in a 1D first order

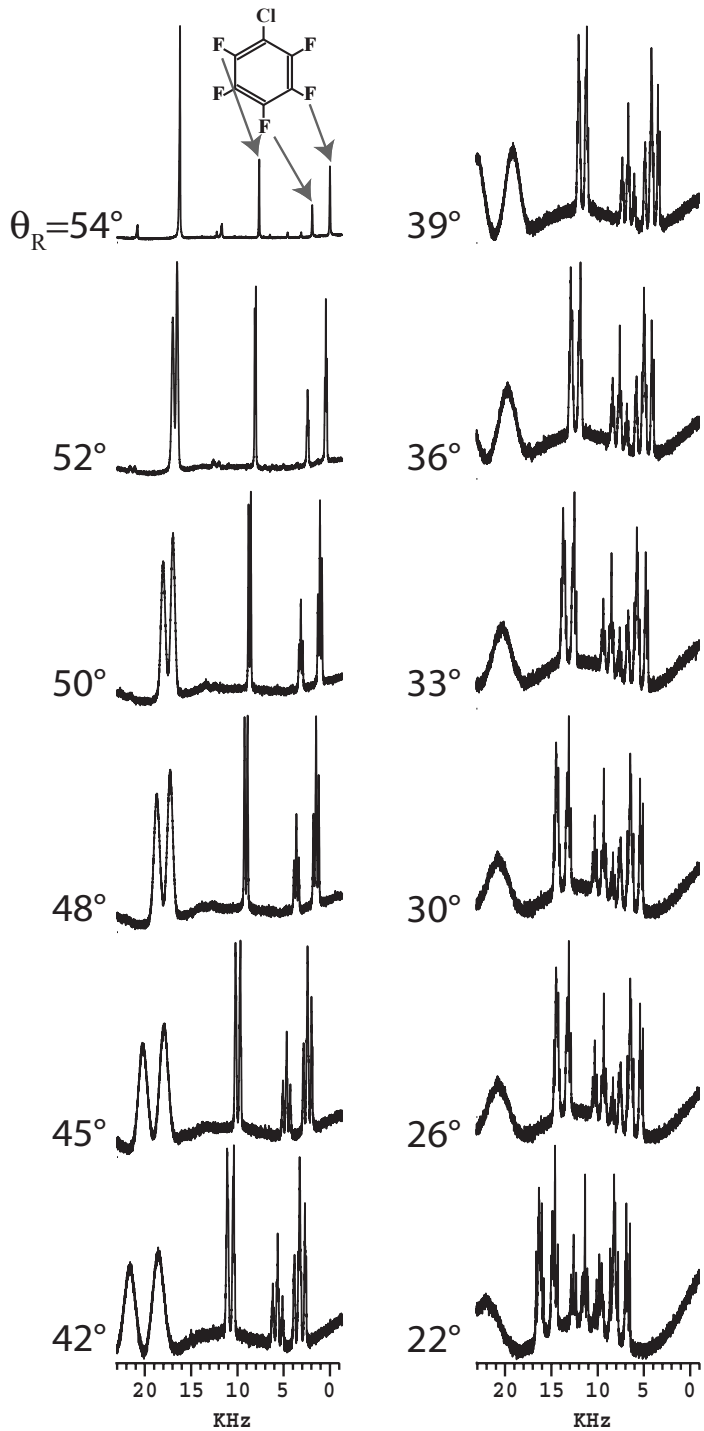

Figure 4.5: ^{19}F spinning spectra ($\omega_R = 4$ kHz) of perfluorochlorobenzene in I52 with the spinning axis at the angle, θ_R, relative to the field as indicated in the figure.

analysis, it is difficult to accurately assign the overlapping first order couplings. The dipolar coupling of the ortho peak suggests that $D^{aniso}_{ortho,meta} = 2208 \pm 7$Hz; this is determined from a fit of the first order doublet splitting to Eq. (4.7) which is a function of $P_2(\cos\theta_R)$ where $P_2(\cos\theta_R)$ is the second order Legendre polynomial and equals $\frac{1}{2}(3\cos^2\theta_R - 1)$. The meta and para fluorines were both pseudo-triplets; thus it is difficult to accurately determine the two different couplings present from a simple first order analysis. The 2D experiments described below will demonstrate how a second dimension helps to separate even these simple first order splittings. In addition to the perfluorochlorobenzene ^{19}F , the liquid crystal ^{19}F first order dipolar splittings could also be fit as a function of $P_2(\cos\theta_R)$ to give $D^{aniso}_{LC} = 9915 \pm 15$Hz. In a similar fashion as with the dipolar couplings, the chemical shift could also be fit using Eq. (4.6) to give δ^{iso} and δ^{aniso}. The isotropic shift values were fit from the first order data to be: $\delta^{iso}_{LC} = 16332 \pm 10$, $\delta^{iso}_{ortho} = 7713 \pm 7$, $\delta^{iso}_{para} = 1921 \pm 7$ and $\delta^{iso}_{meta} = 0 \pm 7$ Hz. The anisotropic contributions to the shift, δ^{aniso}, were fit to be: $\delta^{aniso}_{LC} = 12805 \pm 46$, $\delta^{aniso}_{ortho} = 10045 \pm 37$, $\delta^{aniso}_{para} = 12102 \pm 44$, and $\delta^{aniso}_{meta} = 10573 \pm 39$ Hz. These values will be addressed again and compared to the results from the 2D correlations.

Couplings to ^{19}F beyond the nearest neighbor ^{19}F become apparent at angles smaller than $\sim 50°$. At spinning angles of $\sim 40°$, the spectral complexity begins to make interpretation difficult. Using the angle analysis of Figure 4.5, the spinning angles of 50° and 40° were selected to study in a SAS-2D mode with hopes that they would provide an example of both first- and second order couplings correlated with an isotropic dimension.

4.3 Switched Angle Spinning Probehead

In order to perform the experiments described in the previous section and discussed in more detail in the next section, we designed and constructed a novel SAS probe. Experiments correlating the anisotropic dipolar coupled dimension with the isotropic MAS dimension were performed using this home-built SAS probe that allows for angle hopping from zero to the magic angle within 20 ms. The SAS probe used was a modified Chemagnetics (now Varian Inc., Palo Alto, CA) 5mm HX MAS probe. Angle switching was done by an API Motion (now Danaher Motion, Washington, DC) feedback stepping motor and a pulse programmer triggered motor controller. In addition to rapid movement between angles, a split solenoid coil design was utilized in the probe to allows for a consistent circuit amplitude and phase independent of the angle of rotation. This is an important property when attempting phase cycling in 2D experiments. See Figure 4.6.

Spinning liquid crystal samples commonly requires the use of rotor inserts to prevent sample leakage and degradation. The use of rotor inserts typically reduces the filling factor and may cause spinning instabilities that disrupt the liquid crystalline phase. These problems were circumvented by using Teflon spacers and rubber stoppers. Using appropriately sized rubber stoppers and spacers, stable spinning speeds of > 12 kHz for one week with no sample loss were obtained for a typical liquid crystal sample . In a 5mm outer diameter Chemagnetics pencil rotor, a 3 mm thick Teflon spacer is placed next to a 1 mm thick rubber stopper; then another 5 mm thick Teflon spacer is inserted into each end of the sample.

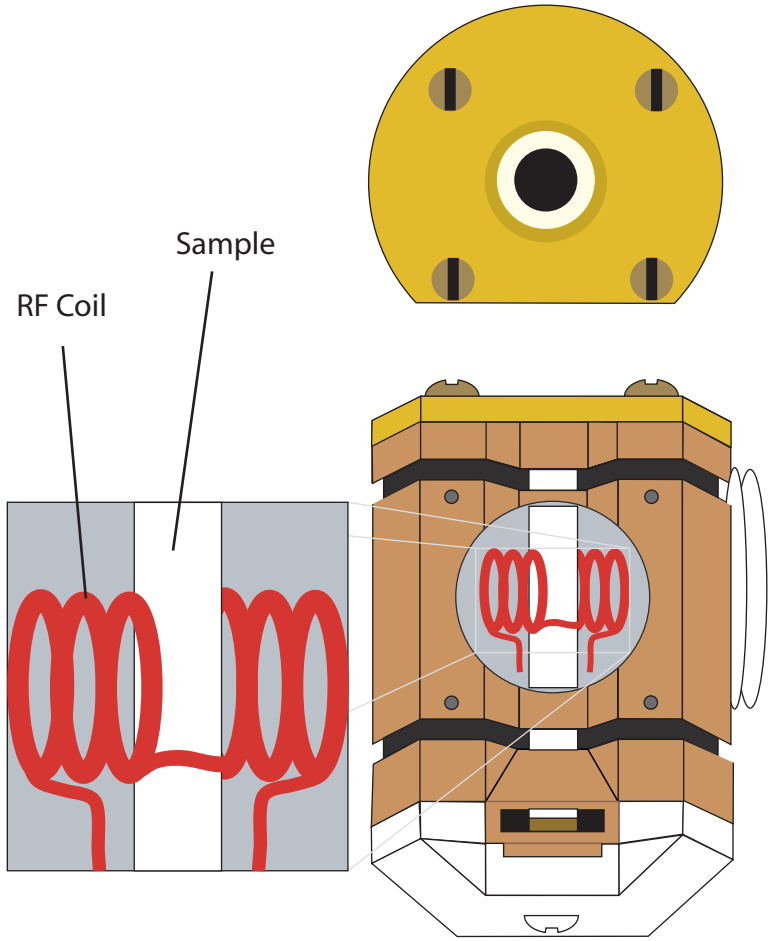

Figure 4.6: Switched angle spinning (SAS) probe diagram. The whole unit (with the exception of the split-solenoid coil) switches angles via a motor controlled string which is attached to the pulley on the right hand side of the diagram.

4.4 SAS: Parallel Director Alignment

The scaled interactions, discussed earlier, can be assigned in a two-dimensional (2D) switched angle spinning (SAS) experiment. First the anisotropic interactions are evolved at a given angle, and then the spinning axis is switched to the magic angle for detection of an isotropic dimension. In this manner, the anisotropic interactions of the spins, that can be complex and difficult to interpret in a 1D mode, are now separated in the second dimension by their isotropic chemical shifts. Similar to previous work performed in solids [44, 45] and in liquid crystals on first order dipolar couplings [38], the 2D SAS experiment provides a method for assigning dipolar couplings in liquid crystals using the isotropic chemical shift. Both first order and second order type 2D correlations will be presented. Additionally, a method that reveals the anisotropic interactions of individual spins in the liquid crystalline phase will be discussed.

4.4.1 First Order System: C_2F_3I

Introduction

The liquid crystal sample of ∼25% w/w iodotrifluoroethylene (Oakwood Products, West Columbia, SC) in 4-octylphenyl-2-chloro-4-(4-heptylbenzoyloxy)-benzoate (Acros Organics, Belgium) was prepared under nitrogen. In all of the following cases, the ^{19}F spectra of iodotrifluoroethylene were recorded with a center frequency of 376.095042 MHz on a system where TMS resonates at 399.741790 MHz. The ^{19}F spins of iodotrifluoroethylene are labeled A, M, and X corresponding to their respective resonance frequencies as depicted in Figure 4.7.

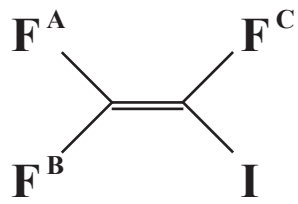

Figure 4.7: Iodotrifluoroethylene with A, M, and X ^{19}F spins labeled.

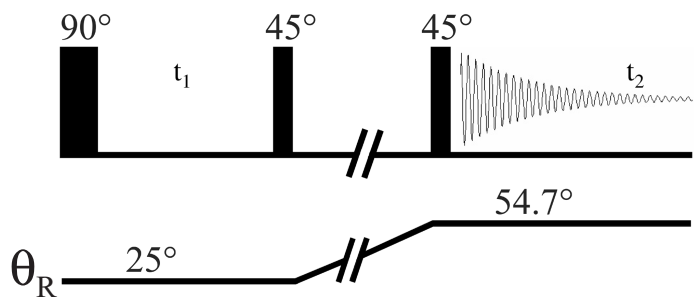

Figure 4.8: Switched Angle Spinning COSY45 Pulse Sequence.

In order to observe the isotropic-anisotropic correlations, a SAS version of the well-known COSY (SAS-COSY) experiment was used as shown in Figure 4.8. The pulse sequence begins with a 90° pulse and a t_1 evolution period. Then a 45° pulse stores part of the signal to allow angle switching to the magic angle. After this a second 45° pulse recalls the signal for observation in t_2 under magic angle spinning. A 45° pulse was used in order to observe more intense signal in the connected transition cross peaks versus the non-connected transition cross peaks [46]. The SAS-COSY pulse sequence is well suited to the requirement of storing the desired signal during the angle switching.

Results: 1D Characterization

The isotropic spectrum of the neat liquid is shown in Figure 4.2a. To demonstrate the ability of MAS to produce an isotropic spectrum, the liquid crystal MAS spectrum is overlaid with the neat liquid isotropic spectrum (Figure 4.2b). The relative shifts and

splittings due to J coupling are nearly identical in the two spectra. However, there exists an upfield shift of approximately 1 kHz when the C_2F_3I is dissolved in the liquid crystal. The origin of the upfield shift has been generally observed in these types of systems and is most likely a result of "π stacking" in this highly ordered system[47]. Another minor difference in the MAS spectrum in Figure 4.2b is the appearance of small spinning sidebands; these are the result of a small amount of thermal disorder that gives rise to a degree of powder-like orientations in the sample. Figure 4.2c shows the ^{19}F spectrum when spinning at an angle of 25° from the magnetic field; note the introduction of dipolar splittings while maintaining a first order type spectrum. In addition, there is a further non-uniform peak position shift from Figure 4.2b to Figure 4.2c due to the CSA.

The chemical shift dependence of the spinning angle,ω_R, was investigated as shown in Figure 4.4a. This dependence results from the anisotropic contributions from the chemical shift. The slope of the linear correlation in Figure 4.4a contains information about the chemical shift anisotropy as it exists in this anisotropic environment by:

$$\delta^{obs} = \delta^{iso} + \delta^{aniso} \cdot P_2(cos\theta_R) \tag{4.8}$$

where δ^{iso} is the isotropic chemical shift, δ^{aniso} is the anisotropic component of the CSA as it exists after the motional averaging from the liquid crystal environment, and $P_2(cos\theta_R)$ is the second order Legendre polynomial. The linear correlation parameters for the three spins (A, M, and X) are shown in Table 4.1. Estimates of the CSA can be derived from the δ^{aniso} parameter; however interpretation of the CSA tensor requires knowledge of the molecular order parameter which is beyond the scope of this paper.

Spins	δ_{iso} (Hz)	δ_{aniso} (Hz)
A	10578	-1210
M	1061	-3319
X	-12437	-2079

Table 4.1: Chemical shift parameters from C_2F_3I

Shown in Figure 4.4b is the spinning angle dependence of the observed dipolar couplings $2D^{aniso}(\theta_R) + J$ as it fits to the linear relation:

$$\Delta_{ij}^{obs} = 2D_{ij}^{aniso} \cdot P_2(cos\theta_R) + J_{ij}^{iso} \tag{4.9}$$

where Δ_{ij}^{obs} is the observed splitting on spins i and j and D_{ij}^{aniso} is the dipolar coupling in the liquid crystal. In Figure 4.4b we obtain the expected linear dependence of $2D_{ij}^{aniso}(\theta_R) + J_{ij}$ versus $P_2(cos\theta_R)$ with the intercept at the J coupling values. The sign of J can be derived from the observation of whether the $2D_{ij}^{aniso)(\theta_R)+J}$ value passes through zero in combination with the assumed negative sign of the dipolar interaction. In order to determine the absolute sign of the dipolar interaction and thus the sign of the J couplings, it is necessary to know the orientational order parameter of C_2F_3I in the liquid crystal. Based on the assumption that the planar molecule would orient with the molecular plane parallel to the liquid crystal director, the dipolar coupling can be assumed to be negative. Courtieu et al. [36] have used similar arguments in assigning the sign of the dipolar couplings in C_2F_3Br. We therefore assign J_{AM} and J_{AX} positive values and J_{MX} a negative value since only $2D_{MX}^{aniso}(\theta_R)+J_{MX}$ did not pass through zero (Table 4.2). Additionally from Figure 4.4b we obtain what we would expect to be the $2D^{aniso}(0°) + J$ values for a non-spinning sample where the scaling

Spins	J^{iso} (Hz)	$2D^{aniso}$ (Hz)
AM	69.0	-472.4
AX	51.2	-596.1
MX	-128.3	-226.4

Table 4.2: Coupling Constants from the Line Fits in Figure 4.4

of the dipolar interaction is unity. The spectra obtained with and without spinning at 0° were nearly identical (not shown).

While spinning at the magic angle, significant thermal disordering occurred within 5 seconds of setting the spinning axis to exactly the magic angle. This thermal disordering was overcome by simply setting the spinning angle slightly less (0.1°) than the magic angle such that slight orienting forces still existed, and yet an isotropic spectrum was still observed.

Results: 2D Correlations

After sufficiently characterizing the interactions in our liquid crystal sample, we will discuss the main goal of this work: a demonstration of the correlation of isotropic chemical shifts with anisotropic dipolar couplings using SAS. In order to illustrate the effects of the liquid crystal and SAS on the COSY experiment, we first performed the conventional COSY-45 experiment without angle switching on the neat liquid C_2F_3I. The conventional COSY-45 pulse sequence is simply: 90° - t_1 - 45° - t_2. Figure 4.9a illustrates how the J couplings provide cross peak patterns that indicate the relative signs of the directly connected transitions. The cross peak regions are enlarged ten-fold relative to the scale of the underlying spectrum. The dashed lines act as a guide to reveal the connected cross

peaks. The projected axes show that only the J coupling is observable in both dimensions, equivalent to the spectrum in Figure 4.2a.

In contrast, the dipolar-isotropic correlation obtained by applying the SAS-COSY experiment of Figure 4.8 on the liquid crystal sample is shown in Figure 4.9b. The liquid crystal sample was spinning at 2 kHz and hopped from 25° relative to B_o in ω_1 to the magic angle in ω_2. The projected dipolar axis (ω_1, horizontal) reproduces the spectrum observed by simply spinning at 25° without angle switching as seen in Figure 4.2c. The projected ω_1 dimension appears somewhat broadened due to a combination of a limited number of points sampled during t_1 (512 points) and minor angle inaccuracies ($< 0.1°$). The projection onto isotropic ω_1 or ω_2 dimensions in Figure 4.9a is effectively identical to the projection onto the isotropic MAS dimension (ω_2) in Figure 4.9b minus solvent effects. The differences in the two projected axes in Figure 4.9b reveal not only the introduction of dipolar coupling but also changes in peak positions due to the CSA contributions. The 10x magnified insets demonstrate how the $2D^{aniso} + J$ values that evolved during ω_1 are readily revealed by the separation provided by the J coupling in ω_2. The measured splittings from the expanded insets were $\Delta_{AM} = 320 \pm 8$ Hz, $\Delta_{MX} = 199 \pm 4$ Hz, and $\Delta_{AX} = 410 \pm 10$ Hz. The values measured in the SAS-COSY experiment agree well with the values as predicted from the linear correlations from Figure 4.4.

The cross peak shapes in this magnitude spectrum are easily understood when considering the spin states of all three fluorines. The directly connected transitions form the corners of the two rectangles in each cross peak, and the slope of the line connecting the center of the two rectangles is determined by the sign of the indirect spin J coupling relative to the observed dipolar coupling (which are all assumed negative in this case). For

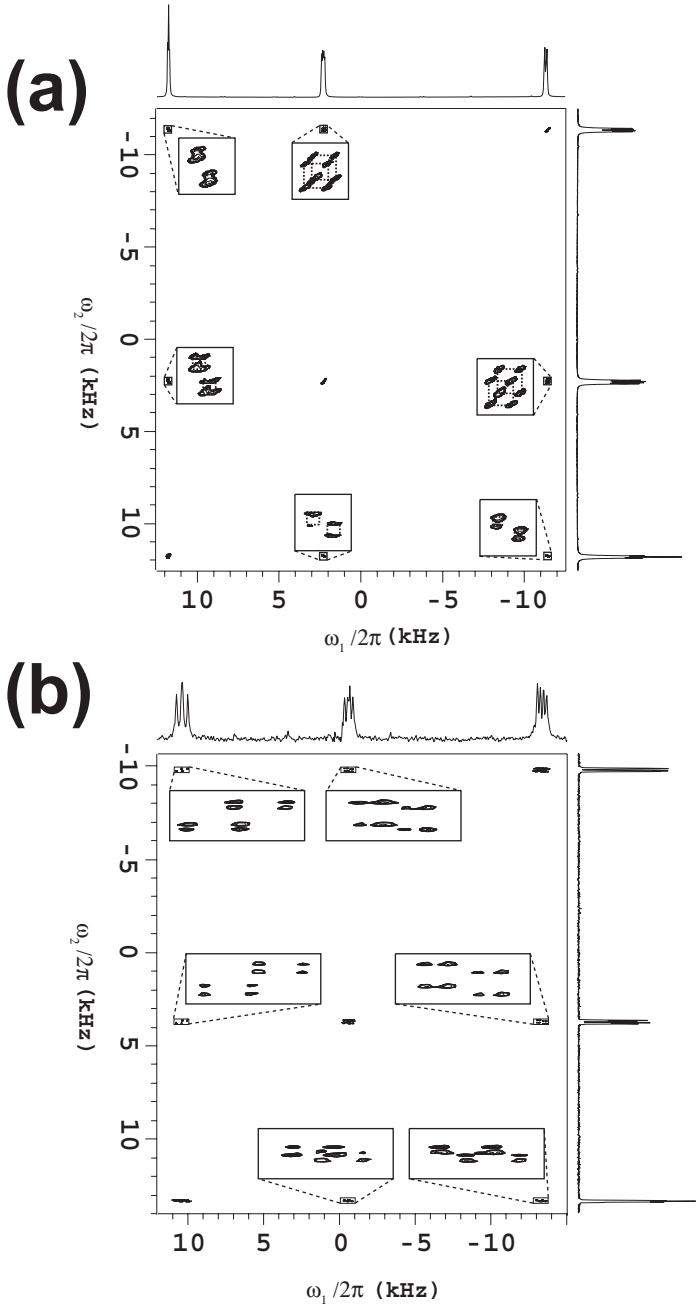

Figure 4.9: (a) The normal COSY-45 pulse sequence performed on the neat liquid C_2F_3I. (b) The SAS-COSY45 performed on 15% w/w C_2F_3I in a liquid crystal.

example, the AX cross peak (upper left) in Figure 4.9b has a negative dipolar coupling in ω_1 and a negative J_{MX} in ω_2; thus the slope of the line connecting the two rectangles is positive. The coupling patterns were reproduced using the Gamma library [48] with the J and $2D^{aniso} + J$ values from Table 4.2. In the simple system investigated here, the dipolar coupling assignments are trivial; however, this demonstration reveals how the dipolar couplings of only connected transitions are spread out in the second dimension by their respective isotropic chemical shifts.

We expect spin diffusion to be a significant problem when dealing with strongly coupled systems where the barriers to spin diffusion are very low. In order to deal with the potential problems of spin diffusion, we are keeping the couplings weak by spinning at angles close to the magic angle and minimizing the hopping time during which significant dipole-dipole coupling take place. This initial work was done utilizing the absence of any fluorine in the liquid crystal itself to avoid problems with background signal. However, extending this method to the more general case with protons requires contending with the potentially large, resolved signal due to the liquid crystal background. Investigations addressing these issues are currently underway.

Conclusions

The liquid crystal SAS-COSY experiment described in this paper illustrates how the isotropic chemical shift correlated with dipolar couplings reveals the dipolar coupling network. The ability to manipulate the liquid crystal director and thus the underlying interactions provides a large degree of experimental utility, particularly in a 2D mode. Numerous advantages are gained by performing measurements of dipolar couplings in the SAS mode

presented here. First, isotropic chemical shifts are maintained in a 2D correlation without the scaling normally associated with multi-pulse homonuclear decoupling techniques. In addition, the homonuclear couplings can be scaled at will in order to maintain a first order type spectrum through the adjustment of the hopping angles. Lastly, by correlating the dipolar information with the isotropic chemical shifts in one experiment, this type of technique may be useful for more complex correlations involving multiple heteronuclei. Even more information may be extracted for interesting systems including organic systems, proteins, nucleotides and lipids. The applicability of this technique is only limited by the selection of a strongly orienting system to allow for the observation of the information rich anisotropic interactions such as dipolar couplings and CSAs.

There currently exist a variety of different orienting systems that immediately lend themselves to investigation with the aid of the SAS-COSY technique. For example, organic liquid crystals, phage, bicelles, and polyacrylamide gels would be amenable to these types of studies. Although in this investigation sample spinning was used to manipulate the director, some orienting systems such as polyacrylamide gels do not require sample spinning. By facilitating the study of residual dipolar couplings in the liquid state, this approach should allow insight into the detailed structure of partially aligned proteins and nucleic acids.

4.4.2 Second Order: C_6F_5Cl

Introduction

To demonstrate the ability to scale a second order spectrum of an oriented liquid crystal sample, the ^{19}F NMR was observed for the small molecule perfluorochlorobenzene

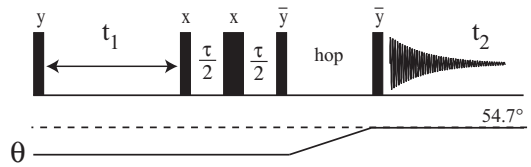

Figure 4.10: A modified SAS-COSY pulse sequence used in Figures 4.11 and 4.12. The upper half shows the radiofrequency pulses with the narrow blocks representing a 90° pulse and the wider block representing a 180° pulse. The lower half shows how the spinning angle, θ , changes during the pulse sequence with direct detection at the magic angle (54.7°).

(C_6F_5Cl) dissolved in a nematic liquid crystal solvent. The second order ^{19}F spectrum of perfluorochlorobenzene (Sigma-Aldrich) 15% w/w in the nematic liquid crystal I52 (EM Industries) is shown in Figure 4.3a. The liquid solute perfluorochlorobenzene was dissolved in the liquid crystal I52 by slow mixing for 5 minutes. The liquid crystalline mixture was then placed in a 5 mm outer diameter ceramic rotor with rubber sealing gaskets[38].

The pulse program used to correlate the dipolar couplings with the isotropic chemical shifts was a modified SAS-COSY type experiment shown in Figure 4.10. Following an initial 90° pulse, the sample evolved while spinning off of the magic angle to allow for dipolar couplings in t_1. The evolved anti-phase magnetization was then converted to in-phase z-magnetization by a 90_x-$\tau/2$-180-$\tau/2$-90_{-y} where τ was constant and approximately 1/(4D) and D is the average dipolar coupling at the initial spinning angle. The spinning axis was then switched to the magic angle by triggering the motor controller. Then a 90° pulse was applied to observe the isotropic signal. Following t_2 acquisition, the angle was switched back to the initial evolution angle for relaxation.

Results

The goal of this work was to examine how an isotropic dimension might provide additional information in what are inherently strongly dipolar coupled systems using a SAS-2D correlation. In this simple sample we wish to demonstrate the feasibility of observing cross peaks to facilitate dipolar coupling assignments. Using the pulse sequence of Figure 4.10 on the same sample as shown in Figure 4.3, C_6F_5Cl in I52, the first order 2D correlation of Figure 4.11 was obtained. The angle θ_R for the initial dipolar evolution was set to 50° to scale the couplings sufficiently to obtain a readily interpretable first order spectrum as seen in Figure 4.3. In Figure 4.11 the observed cross peaks of different spins reveal not only the coupled spins but also the coupling values in a clearly separated manner. The furthest downfield ortho ^{19}F has an observable cross peak only with the upfield meta ^{19}F, and the single midfield para ^{19}F has an observable cross peak to two neighboring meta ^{19}F. The para-meta cross peaks are not as well resolved due to the one-half intensity of the para peak; however the cross peak on the right of the spectrum clearly shows the expected +/- pattern. The +/- pattern of the cross peaks results from the modulation of the transferred coherence as $\sin(Dt_1)$ instead of the familiar in phase $\cos(Dt_1)$. The sign difference also helps to clearly separate the two overlapping doublets of the meta and para ^{19}F which are difficult to distinguish in the 1D spectrum. By utilizing the separation provided in Figure 4.11, the observed couplings at the cross peaks were determined to be $D^{obs}_{ortho,meta} = 272 \pm 6$ and $D^{obs}_{meta,para} = 181 \pm 5$ Hz. The measured value of $D^{obs}_{ortho,meta}$ from the 2D data spectrum is within experimental error of the 1D data. Since only the $D^{obs}_{ortho,meta}$ was readily measurable from the 1D data, we do not compare the value of $D^{obs}_{meta,para}$.

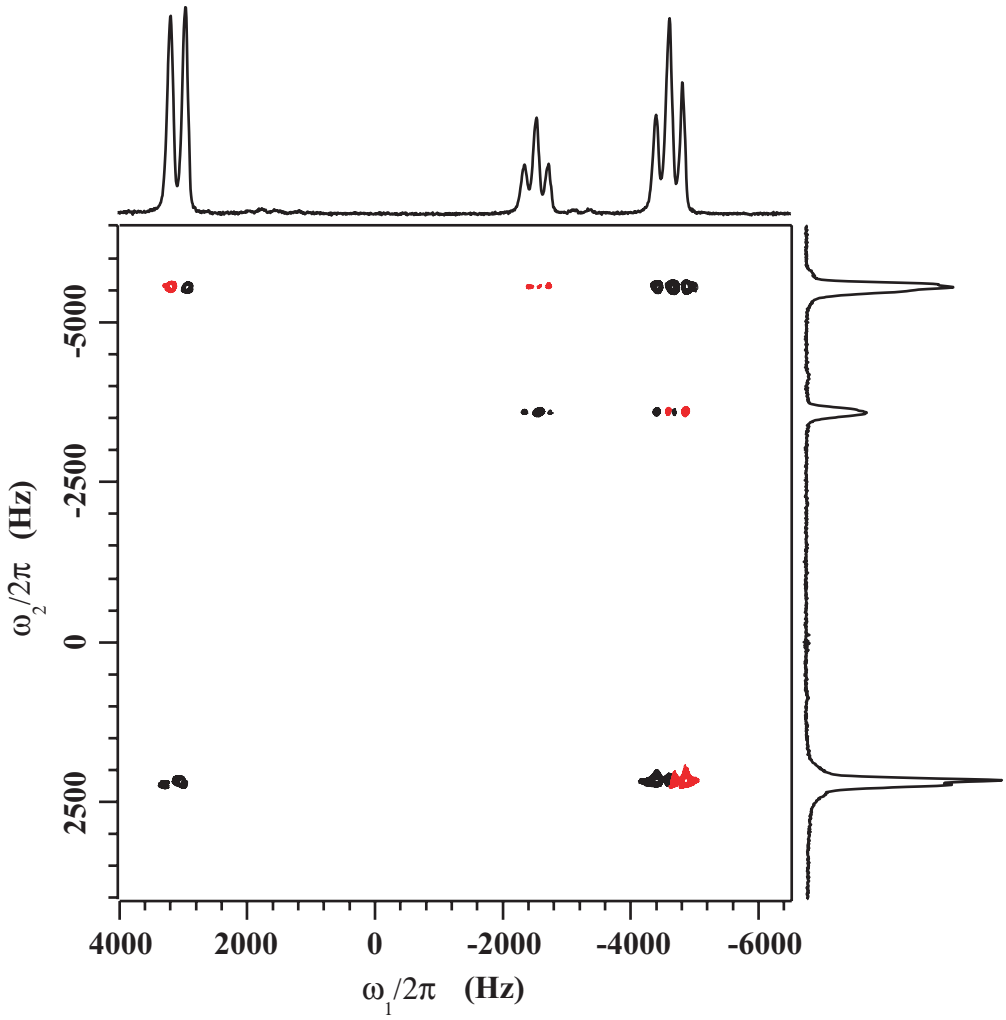

Figure 4.11: ^{19}F SAS-COSY 2D spectrum of C_6F_5Cl in the liquid crystal I52 obtained with the pulse sequence of Figure 4.10. The sample was spinning at 4 kHz and switching angles (θ_R) from 50° in ω_1 to the magic angle in ω_2.

Another notable point in Figure 4.11 is the fact that there is a slight shift from the isotropic chemical shift values in the indirect dimension due to the non-zero contribution from the chemical shift anisotropy according to Eq. (4.6). By comparing the resonance frequencies of the diagonal peaks in the isotropic and anisotropic dimensions, the CSA contributions were fit to Eq. (4.6) to gives values within the error of the measurements from the 1D data. Although the isotropic shift, δ^{iso}, was directly determined from the isotropic dimension, the values were identical to those fit in the previous section and observed in Figure 4.3c. In combination with a quantitative determination of the order parameter of the liquid crystalline phase, structural information could be readily obtained from the CSA and dipolar couplings as determined from the cross peaks in this method. Overall, Figure 4.11 successfully assigns the first order couplings to the appropriate isotropic chemical shifts.

Although the analysis of the first order couplings could be easily assigned in Figure 4.11, the correlation of the second order spectrum obtained at 40° with the isotropic spectrum, shown in Figure 4.12, demonstrates how rapidly the spectrum becomes difficult to interpret. Again, using the pulse sequence of Figure 4.10, the characteristics of the first order spectrum are evident as a doublet and two triplets with some sub-structure due to coupling beyond the nearest neighbor ^{19}F. This is observed directly by the appearance of additional cross peaks where there were previously none in the first order correlation; however it is difficult to quantitatively determine the strength of all of the couplings in the sub-structure. Although the value of τ could be adjusted to emphasize a particular strength coupling in the correlation, we instead used a value determined by the average of the three largest perfluorochlorobenzene couplings.

Adding to the difficulty in the interpretation of the cross peaks is a phase distortion

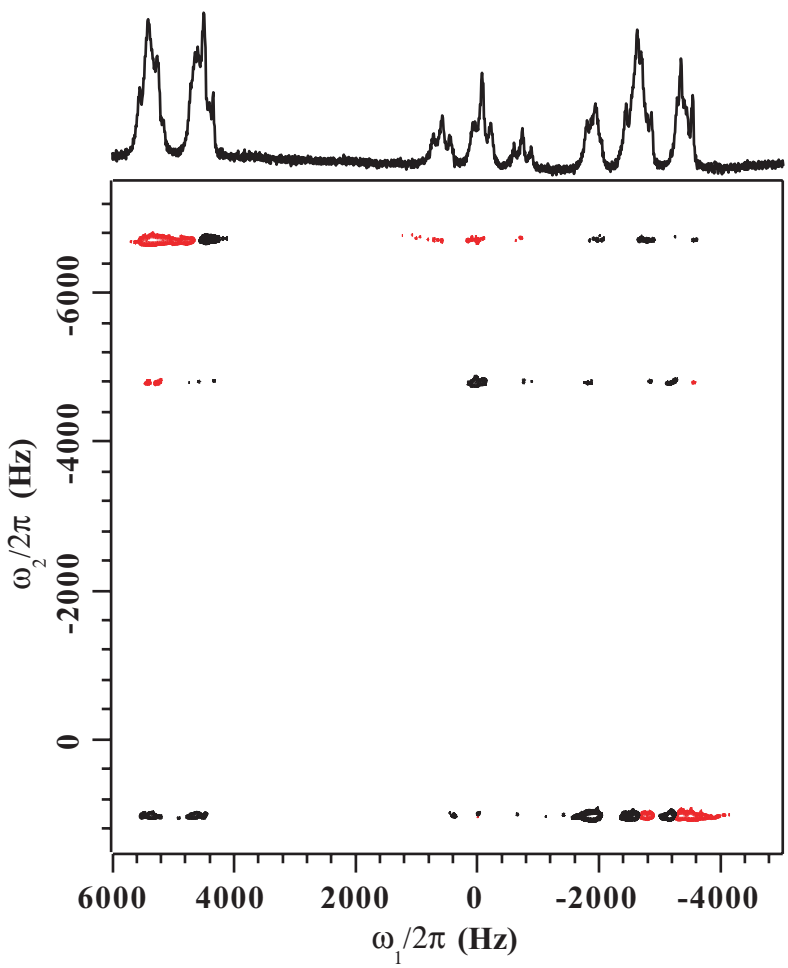

Figure 4.12: ^{19}F SAS-COSY 2D spectrum of C_6F_5Cl in the liquid crystal I52 obtained with the pulse sequence of Figure 4.10. The sample was spinning at 4 kHz and switching angles (θ_R) from 40° in ω_1 to the magic angle in ω_2.

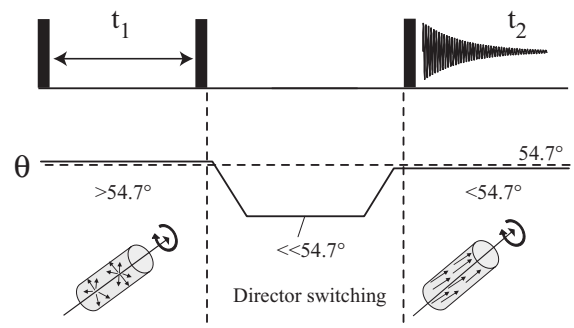

Figure 4.13: Director reorienting pulse sequence which first evolves with the directors aligned perpendicular to the spinning axis in t_1 near the magic angle and then with the director parallel to the spinning axis in t_2 also near the magic angle.

which most likely arises because of ill-defined pulse angles due to the near second order type coupling system[27]. It should be noted that the 1D spectrum shown at the top of the 2D contour plot is not a projection but instead is the 1D spectrum obtained under the SAS-2D conditions. However, in both the first order and second order 2D correlations, the indirect evolution is clearly separated by each of the isotropic chemical shifts.

4.5 SAS: Switched Director Alignment

4.5.1 Introduction

The pulse sequence in Figure 4.13 was used to produce an alternate anisotropic-isotropic spectrum. This correlation was obtained with the liquid crystal directors aligned perpendicular to the spinning axis in t_1 and again with the directors aligned with the magic angle in t_2. In this experiment, spinning sidebands resulting from the time dependent director alignment in t_1 are correlated with the isotropic chemical shifts.

4.5.2 Results

The previous section described a method for obtaining correlations where the director alignment is maintained parallel to the spinning axis while the director is manipulated between the magic angle and 0°. However, the director alignment in this liquid crystal can also be reoriented to the perpendicular phase via spinning the sample at angles 54.7° < θ_R < 90° to provide spinning sidebands of the anisotropic interactions as shown in Figure 4.14a. In this spectrum the spinning sidebands of the ^{19}F appear at $2\omega_r$ for all of the resonances. The spectrum demonstrates how the directors of the sample have oriented at 90° with respect to the spinning axis, and the signal is modulated according to Eq. (4.10). Instead of a simple scaling of the interactions with a change in θ_R as in Eq. (4.7), the signal now has a time dependence of the form:

$$\begin{aligned} S(t,\theta_R,\eta,\psi,\omega_R) &\propto \frac{1}{2}(3\cos^2(\theta_{Lab}(t))-1) \\ &\propto \frac{1}{4}\left(3\cos^2\theta_R-1\right)\left(3\cos^2\eta-1\right) \\ &\quad +\frac{3}{4}\sin^2\theta_R\sin^2\eta\cos(2\omega_R t+2\psi) \\ &\quad +\frac{3}{4}\sin 2\theta_R\sin 2\eta\cos(\omega_R t+\psi) \end{aligned} \tag{4.10}$$

which for θ_R=54.7° reduces to:

$$\begin{aligned} S(t,\theta_R,\eta,\psi,\omega_R) &\propto +\frac{1}{6}\sin^2\eta\cos(2\omega_R t+2\psi) \\ &\quad +\frac{3}{4}\sin 2(54.7^\circ)\sin 2\eta\cos(\omega_R t+\psi) \end{aligned} \tag{4.11}$$

Thus, when spinning this sample at an angle slightly larger than the magic angle, η changes from zero to 90°, the $\cos(\omega_R t)$ vanishes, and all of the anisotropic interactions are modulated by $\cos(2\omega_R t)$ and scaled by a factor of $\frac{1}{6}$. Then interactions can be determined from the analysis of the sideband intensities in a manner similar to that used in the solid state[49]. However, the sidebands tend to overlap, making this type of analysis difficult.

A method to aid in resolving the overlapping sidebands of Figure 4.14a would be to correlate a spinning sideband spectrum with an isotropic spectrum in a SAS experiment similar to the one described in the previous section. In order to perform this type of experiment, the directors must be reoriented parallel to the spinning axis to yield an isotropic dimension. Assuming the director reorientation is rapid, this can be accomplished by the SAS experiment shown in Figure 4.13. The experiment begins with the directors aligned perpendicular to the spinning axis, and t_1 is evolved. Then the angle is switched to 50° to rapidly orient the directors parallel to the spinning axis. Finally, the angle is switched again to slightly less that the magic angle to observe the isotropic spectrum for the direct dimension. Following acquisition, the spinning axis is switched back to 55° for relaxation and reorientation to the perpendicular phase. The perpendicular evolution is obtained at an angle of 55° to keep resonances sharp since they otherwise broaden due to other terms arising from a non-zero value of $P_2(cos\theta_R)$.

The 2D correlation obtained using the sequence of Figure 4.13 is shown in Figure 4.14b. The sideband patterns are now clearly separated by their isotropic chemical shifts, and the anisotropic information encoded in the sidebands can be easily fit. However, the anisotropic information is actually a combination of CSA and dipolar couplings as scaled by the factor $P_2(cos\theta_R)$ and modulated according to Eq. (4.11). In order to sep-

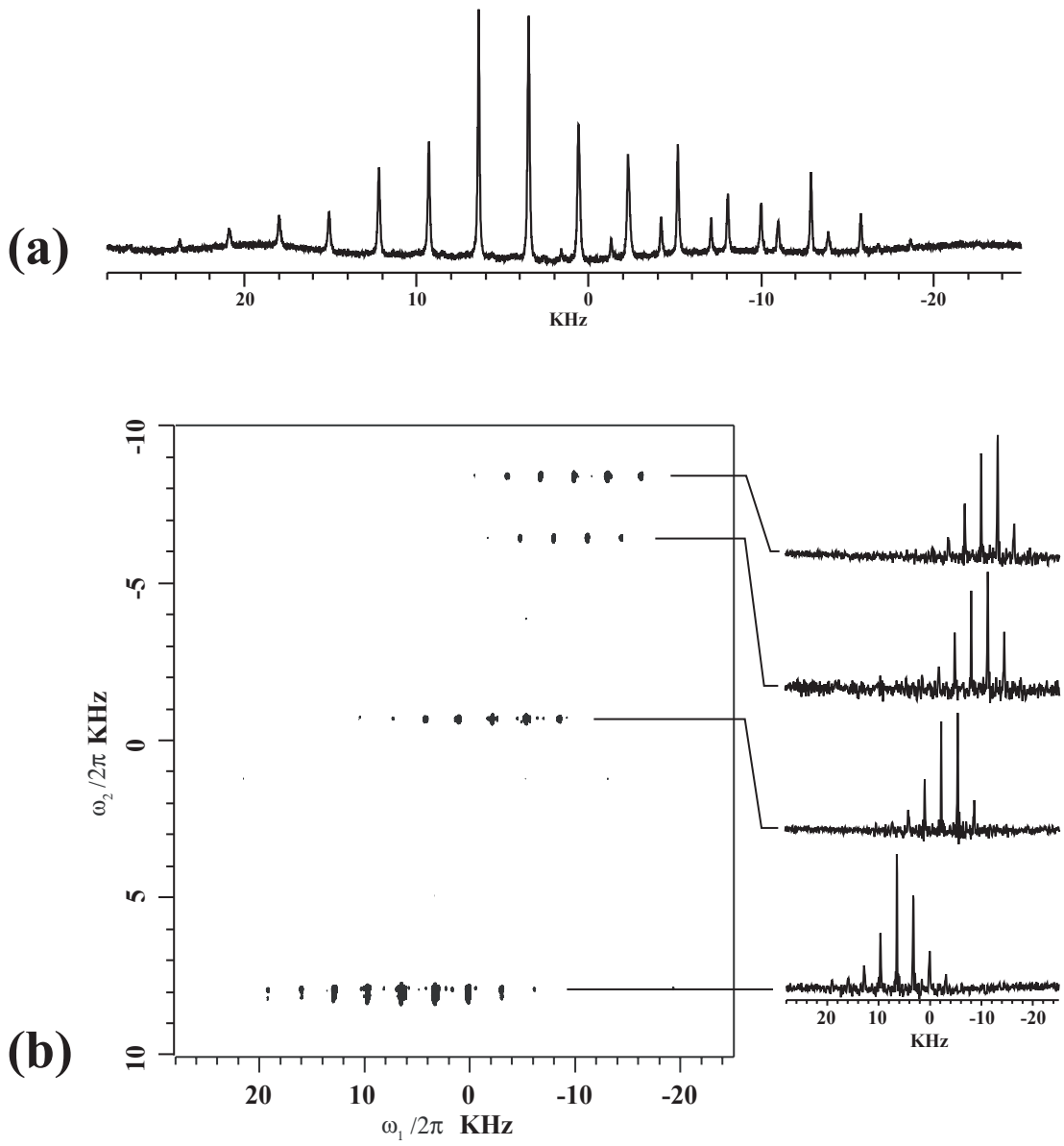

Figure 4.14: (a) The 1D perpendicular phase spinning sideband spectrum with θ_R=55°. (b) 2D SAS isotropic-sideband correlation generated with the pulse sequence in Figure 4.13.

arate the contributions from these two interactions, RF pulses could be applied during t_1 evolution to refocus the chemical shift. Alternatively, a homonuclear decoupling sequence such as Lee-Goldburg[34] could be applied to remove the homonuclear couplings and leave the chemical shift. In Figure 4.14b the principle is easily demonstrated. To the right of the 2D contour plot are 1D slices showing the sideband patterns for each spin. The furthest downfield resonance again corresponds to the liquid crystal background and has significantly more intensity than the three resonances from the perfluorochlorobenzene. In this case we expect many sidebands for all of the resonances in the sample due to the presence of both large dipolar couplings as well as large ^{19}F CSAs.

Although this 2D correlation is of limited use in the case of this sample, quantitative determination of the CSA could be performed for samples containing natural abundance ^{13}C under ^{1}H decoupling where only the CSA contributes to the sideband pattern. This type of experiment could prove extremely valuable for protein structure determination in ^{13}C labeled samples.

4.6 Conclusions

With experimental ease, the second order dipole coupled spectrum can be reduced to a first order spectrum, and then the couplings can be assigned via their isotropic chemical shifts. This method takes the laborious task of assigning the numerous peaks in the second order spectrum and reduces it to the simple task of reading off cross peaks in the 2D SAS correlation. Some would argue that much of the valuable structural information has been lost by reducing the couplings to first order; however this method has the flexibility

to perform as much or as little averaging as the experimenter desires. By performing a SAS correlation between 0° and the magic angle, all of the spectral complexities of the non-spinning case may be recovered.

These methods are applicable to many types of liquid crystals whether they are strongly or weakly oriented, and it is not limited to liquid crystals whose directors can be aligned with sample spinning. For example, samples that achieve alignment through polymer alignment can simply be reoriented by moving the polymer alignment axis. There exist several possible opportunities to utilize switched angle correlation experiments to obtain valuable structural insight into aligned samples.

Implementation of the techniques described here may be beneficial for the interpretation of dipolar couplings and CSAs in liquid crystalline phases. A technique where correlations are performed at successively smaller angles would provide insight into the mechanism by which a first order spectrum transitions into a second order spectrum.

A further application of this technique is to explore interesting systems, for example proteins associated in an oriented bicelle phase. This technique could provide the great benefit of maintaining the isotropic chemical shift for assignment while having the flexibility to scale the dipolar couplings for optimal structural interpretation in a single sample.

4.7 Future Directions

One of the goals of studying oriented systems with SAS correlations was to apply the newly developed methodologies to systems of interest such as membrane proteins. It has been known for some time that lipid bicelles made up of a particular ratio of long and

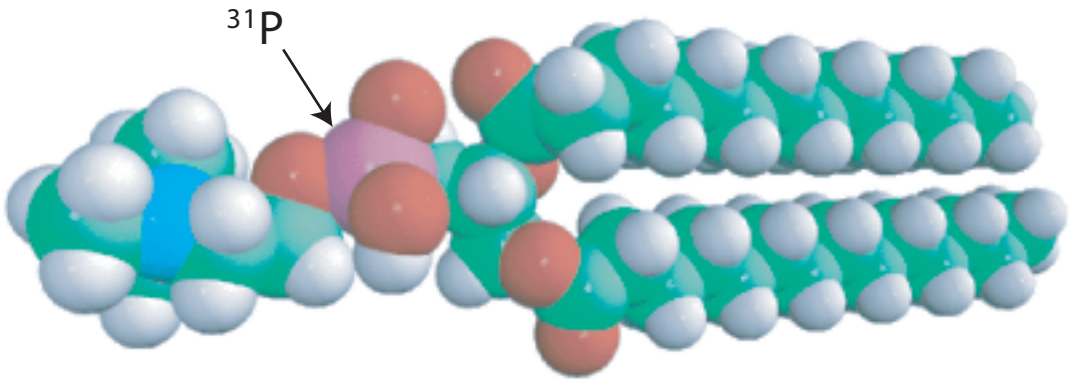

Figure 4.15: 1,2-Dimyristoyl-sn-Glycero-3-Phosphocholine (DMPC) molecule which is a lipid component of bicelles

short chain lipids (such as DMPC in Figure 4.15) can form a pancake-like mesogen which orients in a magnetic field[31, 50].

By utilizing the aligned bicelle phase, the dipolar couplings can again be turned off and on as demonstrated in the previous section. Unlike what is achievable using RF homonuclear decoupling, such as MREV-8 (shown in Figure 4.16), MAS of the oriented phase eliminates the couplings without any associated scaling factor. Without the improved performance offered by MAS, a relatively low resolution spectrum is obtained; this can be observed when the static MREV-8 spectrum of Figure 4.16 is compared to the 5 kHz MAS spectrum of the same sample. In this way, we are able to obtain isotropic liquid-state resolution while being able to turn the couplings off and on.

In addition, the interactions in the bicelle sample can be scaled at will by changing the spinning axis. As is shown in Figure 4.17, a splitting of the ^{2}H signal from water exchanging on and off the surface of the oriented bicelles reveals the averaged quadrupolar interaction. Just as in the case with the dipolar couplings previously discussed, this splitting dependence is a function of $P_2(\cos\theta_R)$. This dependence is plotted in Figure 4.18.

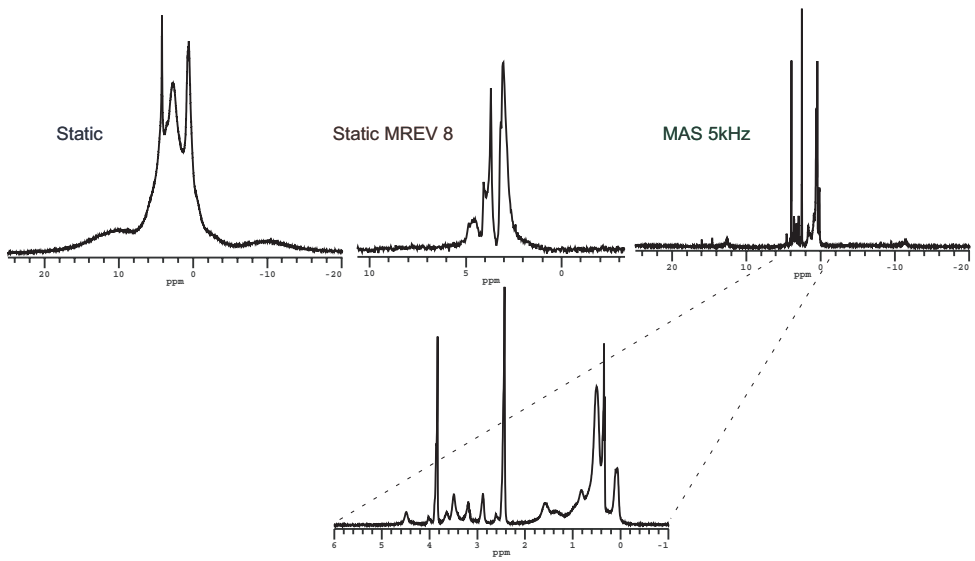

Figure 4.16: The ^{1}H NMR spectrum of oriented bicelles. Using the MREV-8 homonuclear decoupling sequence and also MAS to remove the strong ^{1}H-^{1}H dipolar couplings in the oriented sample.

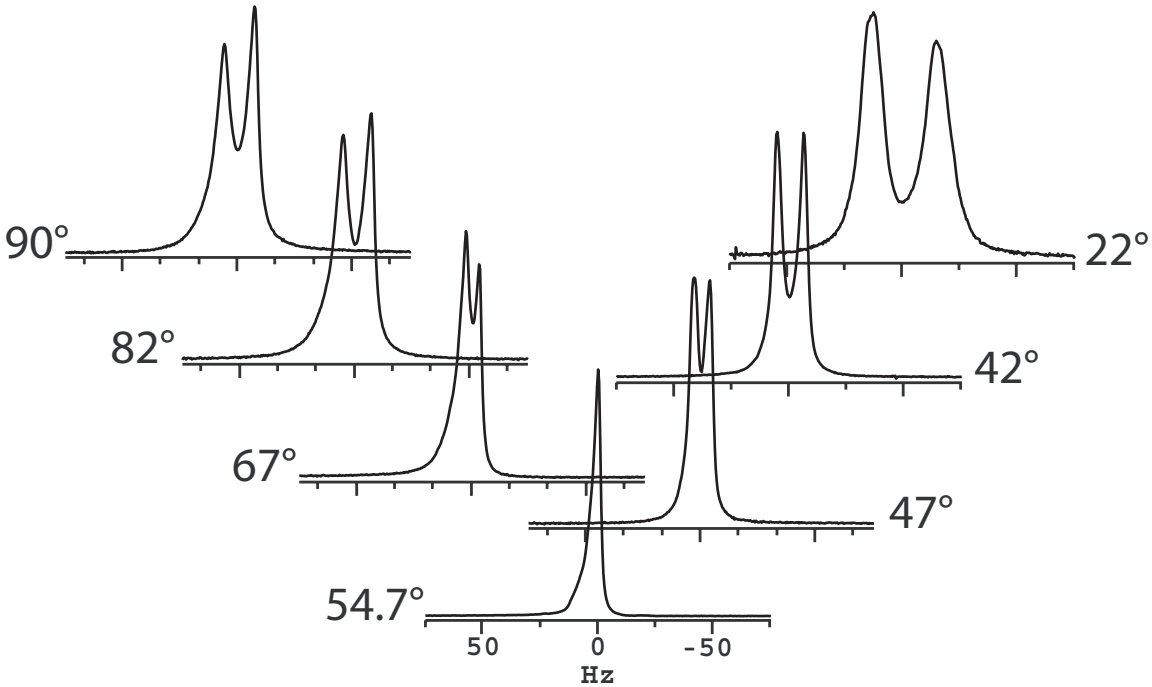

Figure 4.17: ^{2}H NMR of the ^2H_2O in an oriented 2.7 kHz spinning bicelle sample

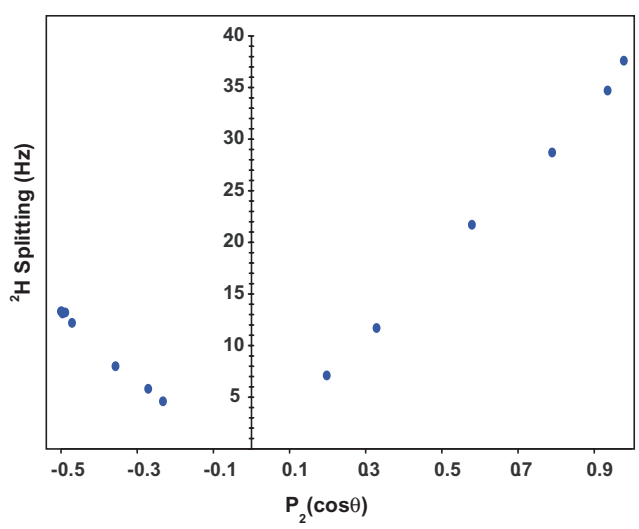

Figure 4.18: Correlation plot of the ^{2}H NMR splitting of the spectra in Figure 4.17 as a function of $P_2(\cos\theta)$

To demonstrate the abilities of SAS local-field experiments, Figure 7.4.4 shows a 7-spin simulation of the expected spectra in a SAS proton detected local-field experiment. The 2D correlation reveals each of the individual ^{31}P-^{1}H couplings in the lipid molecule (see Figure 4.15) which is separated by the corresponding proton's isotropic chemical shift.

The continuation of this work might provide interesting structural information about the conformation of lipids in bicelles; however we eventually hope to incorporate membrane proteins into the bicelle's lipid bi-layer. In this way, a PDLF experiment similar to Figure 7.4.4 could be performed on the associated membrane protein while assigning potentially all of the ^{15}N-^{1}H and ^{13}C-^{1}H dipolar couplings. With the ability to assign long-range dipolar couplings, this method would provide strong structural constraints which are difficult to determine by any other method.

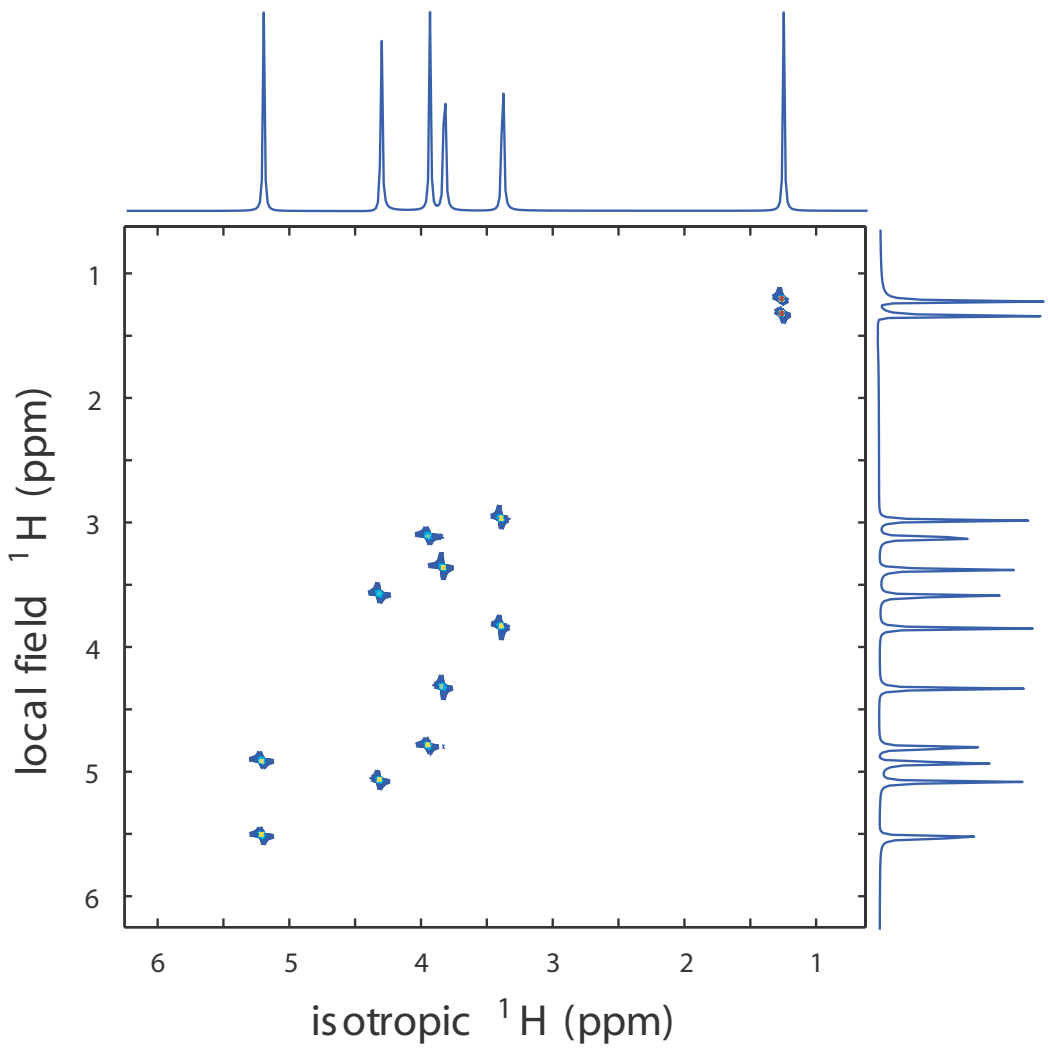

Figure 4.19: SAS-PDLF Simulation of an oriented bicelle

Chapter 5

Solid State NMR

As was clearly demonstrated in the phase cartoons of Figure 3.1 the solid phase is different from the liquid crystalline phase discussed in Chapters 3 and 4. With the lack of molecular tumbling of the solid state relative to liquids and liquid crystals, the interactions observed are in their full anisotropic form as was briefly introduced in Chapter 2.

5.1 Issues in the Solid State

The challenge with solid state NMR is how to observe accurately a single interaction among a chorus of very strong interacting ones. Take for example a simple hydrocarbon molecule in the solid state and attempt to observe the proton NMR signal. Due to the ^{1}H-^{1}H dipolar coupling of 120.12 $\frac{kHz}{\mathring{A}^3}$ any system with more than a few protons is a strongly coupled many body spin system. Even when a solid sample is a simple two spin system the resonance lines are typically very broad compared to what is observed in liquids or liquid crystals. The static NMR spectrum of an isolated dipole coupled pair, usually termed a

Pake-doublet, is depicted for the homonuclear case in Figure 5.1. The range of frequencies in Figure 5.1 are due to the θ dependence in Eq. (2.37) which ranges from $-\frac{3}{2}d$ (where $d = \frac{-\gamma_i \gamma_j \hbar}{r_{ij}^3 \frac{\mu_0}{4\pi}}$) to $\frac{3}{4}d$, and the negative of this is obtained by a change in spin state of one of the two spins. With dipolar interactions typically on the order of kilohertz, having more than a few *isolated pairs* of spins having overlapping Pake-doublets would be difficult to deconvolute. Since most samples of interest are not sets of isolated pairs, but are instead a network of strongly coupled spins, in order to observe high resolution spectra this broadening must be overcome.

In addition to the lineshapes obtained due to dipolar coupling, the chemical shift anisotropy (CSA) also has an orientation dependence with respect to the field as was described by Eq. (2.18). This orientation dependence is depicted in Figure 5.2, where as the molecule changes orientation in the field, the resonance frequency changes according to the chemical shift tensor PAS components σ_{11}, σ_{22}, and σ_{33}.

The combination of broadening due to a non-ideal dipole coupled spin system and the chemical shift anisotropy make for a static solid spectrum which would be extremely broad for powders of rigid crystals. Of course, if the sample were a single crystal and all of the molecules were aligned in an identical fashion, this would make for a much sharper spectrum with relatively narrow resonance lines. However, sufficiently large single crystals are often difficult to grow for any given sample of interest, therefore, randomly distributed crystallites in the form of a powder are usually what is studied.

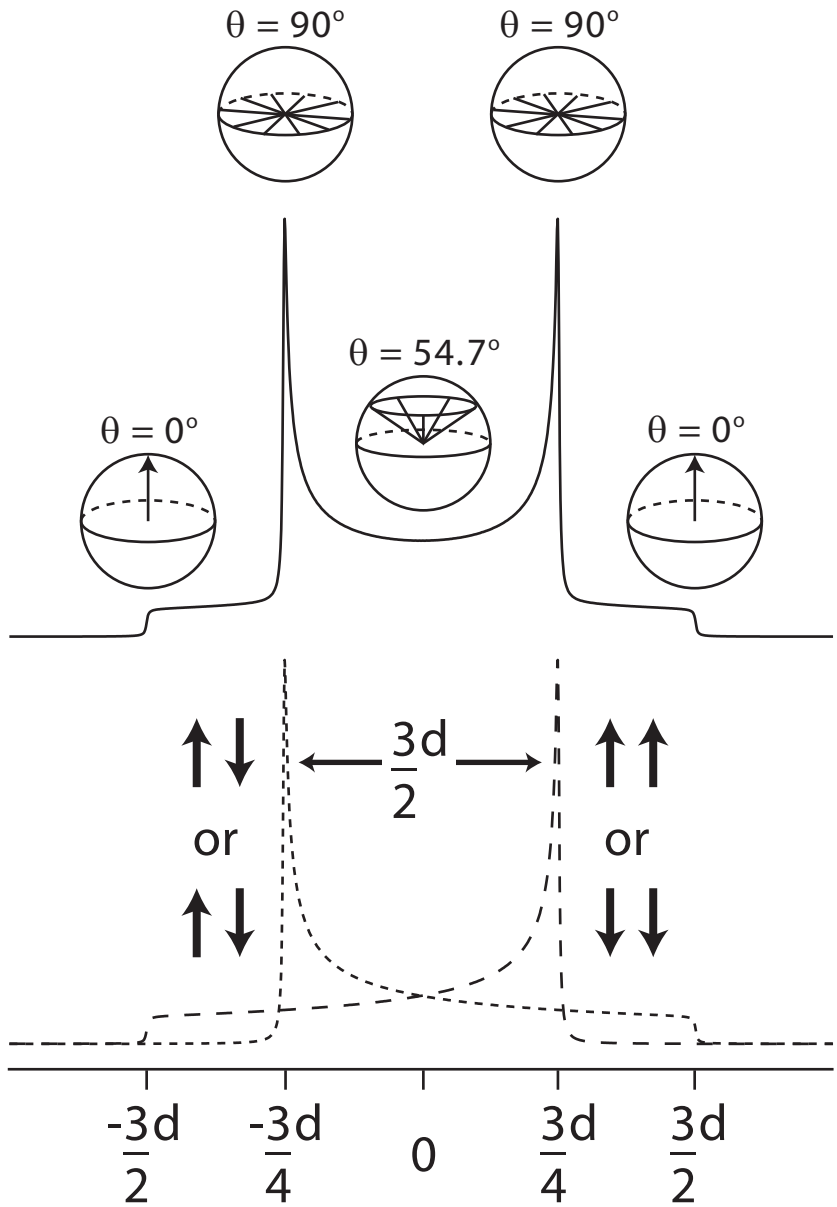

Figure 5.1: Diagram of the homonuclear dipolar powder pattern. The spheres at the top of the figure indicate what frequency components the spatial powder contributes to the lineshape.

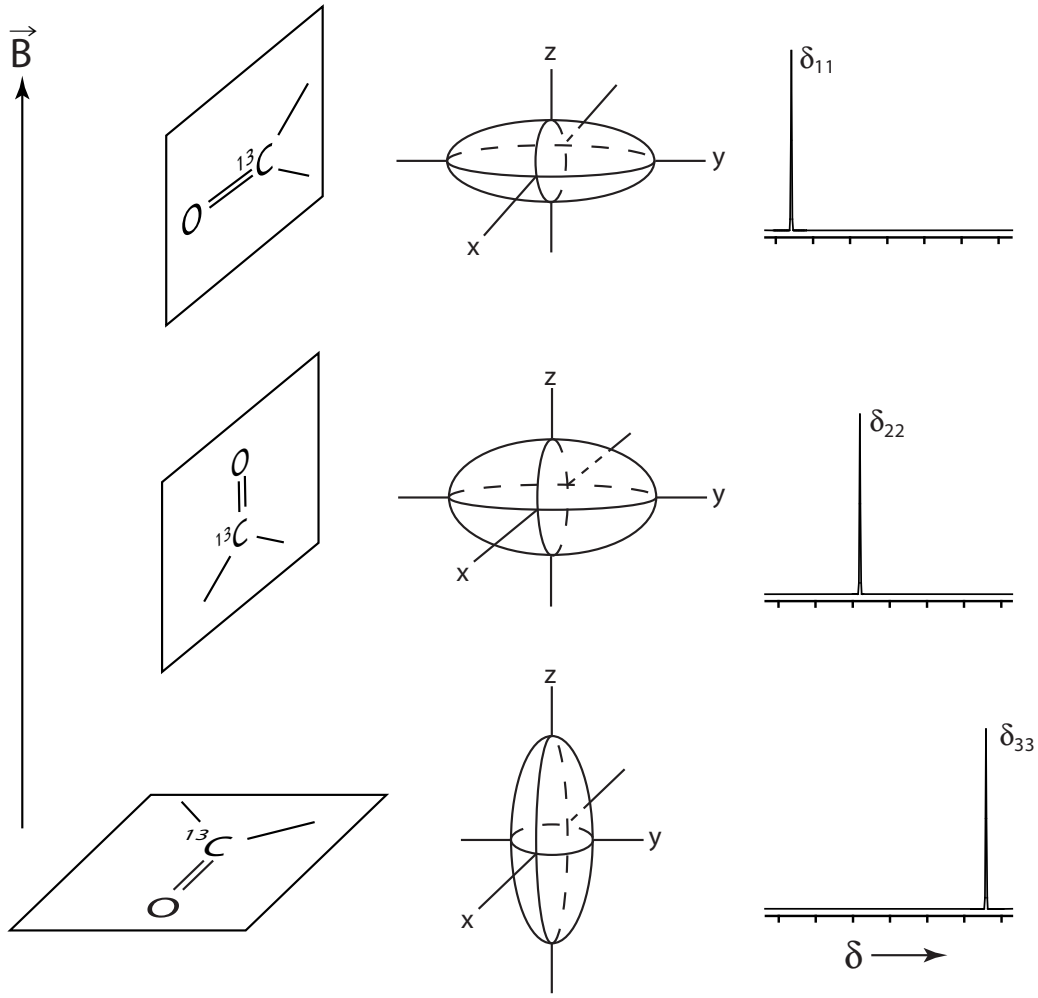

Figure 5.2: Diagram of the principal elements of the CSA tensor

5.1.1 Decoupling Strong Interactions

Given the broad nature of solid state NMR, in order for studies to provide spectroscopic information about the structure of the molecules studied, the resolution must be improved. Aside from CW and homonuclear decoupling which were mentioned in Chapter 3 the most utilized decoupling method in solids is magic angle spinning (MAS). By spinning the sample at the magic angle, spin interactions such as dipolar coupling and CSA become time dependent. If the spinning speed is much larger than the interactions, only the time independent parts survive and the spectrum is that of the isotropic chemical shift (for spin-$\frac{1}{2}$ nuclei). When the interactions are on the order of the spinning speed, spinning sidebands occur at frequencies ω_r which map out the time dependent interaction. Details on the origin of the sidebands can be found in Mehring's book[3]. It is sufficient to realize that by measuring the intensities of all of the sidebands from a given spin, the spin interaction can be reconstructed if all other spin interactions are completely decoupled. For example the method for reconstructing the principal components of the chemical shift tensor from spinning sidebands is widely used[49, 51]. As depicted in Figure 5.3 the static spectrum can be reconstructed from a series several MAS experiments.

5.2 Current Abilities

Some of the most important developments in modern solid state NMR are related to the ability to increase resolution to levels similar to that found in the liquid state. Tremendous effort has been expended to improve decoupling abilities whether it be through faster spinning speeds[52] or multiple pulse sequences[53]. Perhaps ironically, another area

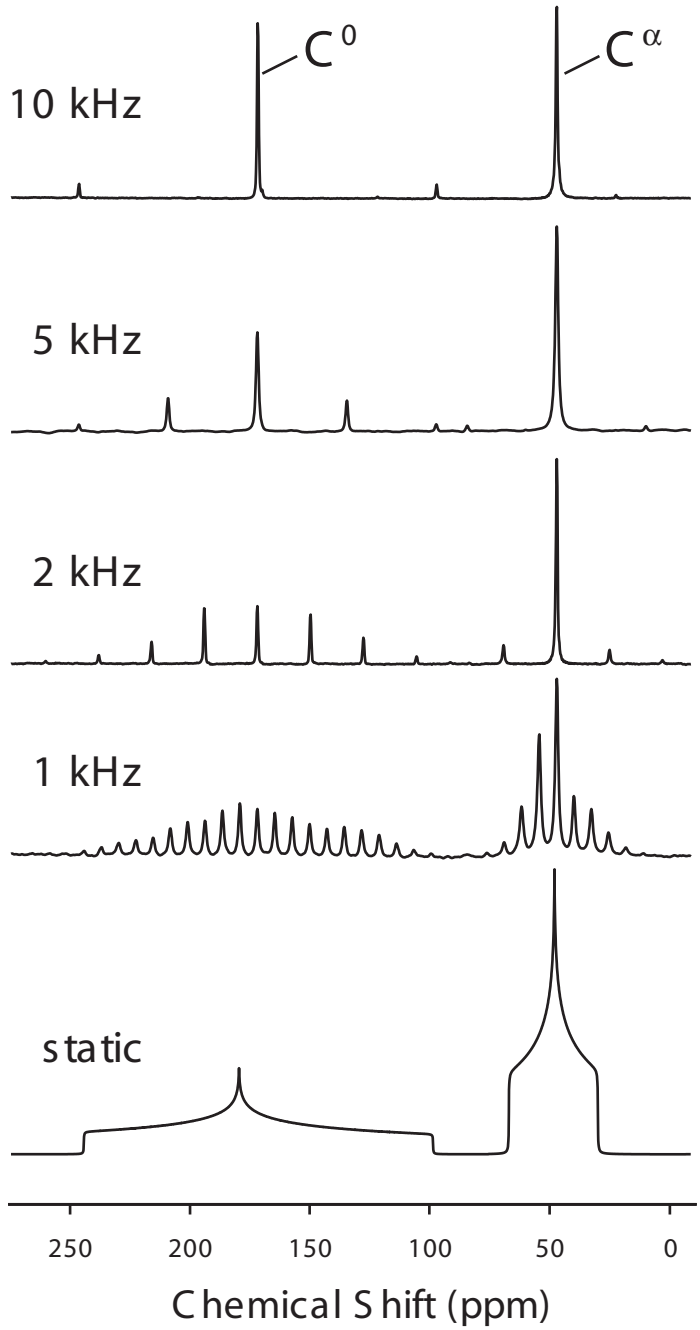

Figure 5.3: ^{13}C CP-MAS spectra of labeled glycine with ^{1}H CW decoupling at 125 MHz, the spinning speeds are as indicated on the figure. The static spectrum is a simulation based on the CSA tensor derived from the spinning spectra.

of developments in modern solid state NMR is the ability to reintroduce (or recouple) the interactions that were initially removed to provide high-resolution.

The recoupling of the dipolar interaction has received much attention in solid state studies due to the $\frac{1}{r^3}$ dependence of the interaction. These dipolar recoupling methods often have the drawback of producing a recoupled interaction which has an orientation dependence and does not directly yield the desired dipole coupling. There has been much progress in this area in the last few years [54, 55, 56, 57] and Chapter 7 introduces new methodologies that extract only the desired isotropic value of the coupling. These methods are then applied to study the uncertain structure of ferrocene in the solid state.

Although the CSA in solids has been well studied, it's use for determining structure has been somewhat limited. Although this interaction is highly correlated with the environment of the nucleus, there is no direct route to structure. There have been many advances in the area of making links between the CSA and structure, and we present contributions to this area in the next chapter.

Chapter 6

Using the CSA to Determine Structure

6.1 Introduction

Considering the available interactions in NMR, the chemical shift has perhaps the greatest potential to reveal detailed information about the bonding environment and geometry of a given nucleus. The isotropic part of the chemical shift is the most widely utilized interaction in NMR, however, the isotropic chemical shift, δ^{iso}, has very limited information about the three-dimensional environment that the nucleus resides in. Alternatively, the chemical shift anisotropy (CSA) is strongly correlated with the three-dimensional electronic environment of the nucleus.

The problem with harnessing the CSA to provide specific structural information lies with the interpretation. Since the chemical shielding is directly related to the electronic properties of a molecule, in principle, the shielding could be calculated for a variety of

geometries and (overlooking any degeneracies, etc.) structure determined via comparison with the experimental determination. However, determination of the electronic structure of molecules and thus the shielding is not an exact calculation. Instead, the methods used in electronic calculations rely on some approximations which might provide poor correlation with the experiments[58, 59]. Nevertheless, rapid progress and new approaches have been made recently in both computational methods and hardware which allows for more accurate calculations[60, 61, 62]. In this section, modern *ab initio* computational methods are combined with developments in experimental determinations of the CSA to provide structural information in proteins and peptides.

6.2 Proteins and Peptides

Fortunately, proteins are a polymer composed of monomeric units (called a peptide) which have limited conformational variability along the polymer main chain (called the backbone). The majority of a protein's conformation and 3D fold is determined by the backbone dihedral angles ϕ and ψ as depicted in Figure 6.1. Peptides generally fall into approximately one of two conformation categories α-helix or β-sheet as determined by the dihedral angles ϕ and ψ. Due to the fact that the peptide dihedral (O=C-N-H) is always nearly 180°, the conformational space is somewhat restricted to ϕ, ψ variations. There also exists an additional dihedral χ which determines the rotation about the C^{α}-R bond, where R is the sidechain of the amino acid (as indicated in Figure 6.1). It is thought that by studying the chemical shift changes of the C^{α} and possibly the C^{β} (first carbon of the sidechain R), structural information can be obtained.

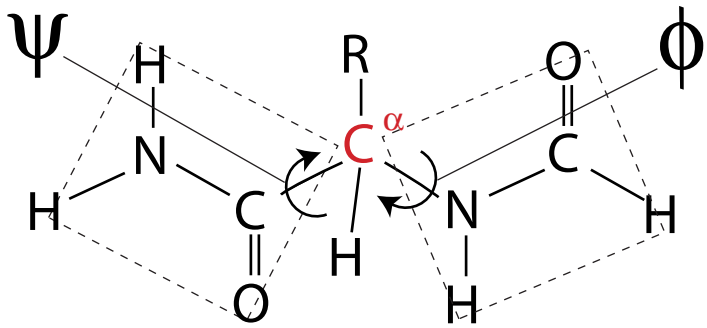

Figure 6.1: Diagram of ϕ, ψ dihedral angles in an amino acid. The two angles are central to the C^{α} and are essentially determined by the rotation of the peptide planes indicated by the dashed lines.

6.3 CSA Tensors in Proteins and Peptides

Over the past few years, there has been an increased interest in the use of the isotropic chemical shift and the chemical shift (or shielding) tensor in investigating peptide and protein structure. This work has included a number of *ab initio* and density functional theory quantum chemical investigations aimed at relating chemical shifts and shift anisotropies to structure[63, 64, 65, 66, 67, 68]. In early work, Spera and Bax[69] reported clear differences between isotropic C^{α} and C^{β} shifts in helical and sheet geometries, and these shifts have been quite accurately predicted by using quantum chemical methods[70]. Recent work shows experimental and theoretical shift (or shielding) tensor results, σ_{ii}, for a series of alanine-containing peptides[71]. Other work also demonstrated that peptide backbone ϕ,ψ angles could be derived from the experimental shift tensor results, using a Bayesian probability method[71]. In addition, results of a theoretical study of the C^{α} shielding tensors in Gly, Ala, Val, Ser, Thr and Ile containing peptide fragments were also reported[72]. In this work, it was noted that for C^{β}-substituted amino-acids (valine,

isoleucine, serine and threonine) not only was the ∼4-5 ppm increase in isotropic shielding of sheet conformations over helical ones observed, but in addition there was in general a large increase in overall tensor span ($\Omega = \sigma_{33}$-σ_{11}), and a change in tensor orientation, for sheet versus helical residues[72]. More recently, this difference in tensor span has been used in the identification of protein secondary structure in the solid-state using a CSA-based spectral editing technique[73].

In solution NMR, CSA information can be gleaned from cross-correlated relaxation measurements [74], Tjandra and Bax [75] also obtained quantitative experimental information on the $^{13}C^{\alpha}$ CSA which correlated with backbone structure: on average in α-helices, σ_{orth}-σ_{par} = 6.1 ± 4.9 ppm whereas in β-sheets, σ_{orth}-σ_{par} = 27.1 ± 4.3 ppm, where σ_{par} is the shielding in the direction parallel to the C-H bond and σ_{orth} is the average shielding orthogonal to this bond. This effect was first predicted theoretically by Walling et al.[76], who investigated "idealized" helical (ϕ = -60°, ψ = -60°) and sheet (ϕ = -120°, ψ = 120°) geometries for 18 amino-acids, then Sitkoff and Case[66] made a direct comparison of the $^{13}C^{\alpha}$ CSA values for ubiquitin and calmodulin/M13 using an alanine fragment[66].

There are, however, a number of apparently striking observations. First of all, Sitkoff and Case[66] were able to reproduce reasonably well the entire set of reported ubiquitin and calmodulin CSA values ($\Delta\sigma^* = \sigma_{orth}$-$\sigma_{par}$) just by using alanine as a model for all amino-acids, but alanine is known to have about the same CSA, Ω, in both helical and sheet geometries[72]. This suggests that the "CSAs" measured in solution are overwhelmingly dominated by a change in shift tensor orientation, as first suggested by Walling et al.[76] not by any change in the span (Ω) seen in solid-state NMR, or from $\Omega = \sigma_{33}$-σ_{11} = $\Delta\sigma$ values obtained from calculation. Second, in recent calculations on phenylalanine,

tyrosine, leucine, cysteine and lysine[77], it was reported that C^{α} spans are essentially the *same* in both helical and sheet residues: only C^{α} of threonine, valine and isoleucine appear to show large differences in CSA (Ω) between helical ($\Omega \sim 20$ ppm) and sheet ($\Omega \sim$34 ppm) geometries[72, 77]. In previous work, serine was included as a member of a substituted amino-acid class (Val, Ile, Thr and Ser)[72], but the results of more recent work suggest that a more (NMR) appropriate classification of the amino-acids is: β-branched (two substitution on C^{β}, i.e. Val, Thr and Ile) and non-branched (the remaining amino-acids). If correct, this would have important implications for spectral editing experiments based on Ω, or structural conclusions which might be drawn from Ω.

In this section a route to structure via the chemical shift tensor is presented by carrying out experimental and theoretical investigations of the $^{13}C^{\alpha}$ shielding tensors in two non-branched amino-acids, alanine and leucine, in a series of crystalline peptides. This is in addition to investigating C^{α} shielding in valine in small peptides, to validate the results of the quantum chemical calculations on small molecules. Additional theoretical investigations of the $^{13}C^{\alpha}$ $\Delta\sigma^* = \sigma_{orth}$ - σ_{par} values of these and other peptides were performed for the solid state. The results for leucine are particularly interesting since they show that both helical and sheet fragments have the same CSA (Ω), because leucine is an unbranched amino-acid, but due to tensor rotations, $\Delta\sigma^*$=σ_{orth} - σ_{par} for solid leucine residues range from ~10 to 30 ppm, just as found in solution NMR investigations.

6.3.1 Experimental Section

Synthetic Aspects. Four peptides were synthesized: LL*VY-OMe[78], L*LVY-OMe, Boc-V*AL-Aib-*VAL-OMe, and Boc-VA*L-Aib-VAL-OMe. An "*" placed before an

amino acid letter indicates that it is $^{13}C^{\alpha ?}$labeled. The "Aib" in the Boc peptides indicates an α-aminoisobutyric acid residue. Using different crystallization solvents (methanol / water [79] or DMSO / isopropanol [80]), the Boc-VAL-Aib-VAL-OMe peptides were crystallized in two different conformations.

NMR Spectroscopy. ^{13}C NMR spectra of both Boc-V*AL-Aib-*VAL-OMe conformers and the Boc-VA*L-Aib-VAL-OMe/MeOH-water peptides were obtained at 7.07 Tesla (corresponding to a ^{13}C Larmor frequency of 75.74 MHz) on a home-built spectrometer based on a Tecmag (Houston, Texas) pulse programmer. A Chemagnetics (Fort Collins, CO) 4-mm MAS probe was used for these experiments. Spinning speeds were controlled to ± 1 Hz using a home-built spinning-speed controller. The CP contact time was 2.5 ms, the ^{1}H decoupling field strength was 108 kHz, and the recycle delay was 1.5 seconds. Spectra of the Boc-VA*L-Aib-VAL-OMe/DMSO-isopropanol peptide, as well as both LLVY-OMe peptide ^{13}C NMR spectra, were obtained at 11.72 Tesla (corresponding to a ^{13}C Larmor frequency of 125.75 MHz) using a Varian/Chemagnetics (Fort Collins, CO) Infinity spectrometer with a 4mm MAS probe. Spinning speeds were controlled to within ± 3 Hz using a Chemagnetics spinning-speed controller. The CP contact time was 2.0 ms, the ^{1}H decoupling field strength was 104 kHz, and the recycle delay was 2 seconds. The experimental spectra were taken at a range of sample-spinning speeds and fitted by using the Herzfeld-Berger method[49]. An average of the CSA values derived from each spinning speed was used to compare with the theoretically calculated values. Isotropic shift values were measured relative to the carbonyl carbon of glycine in a reference sample, taken as 176.04 ppm downfield from tetramethylsilane (TMS; IUPAC δ-scale).

Computational Aspects C^{α} shieldings for alanine, valine and leucine were evaluated

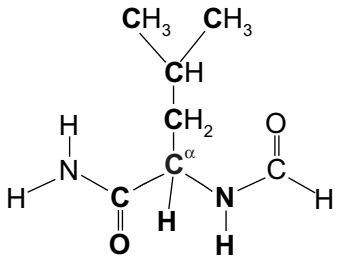

Figure 6.2: Leucine fragment used in the *ab initio* calculations of the chemical shielding tensor. The bold atoms used the basis 6-311G(2d,2p) while the remainder used 6-31G.

by using Hartree-Fock theory and the gauge-including atomic orbitals[81] (GIAO) approach. Full Ramachandran chemical shielding surfaces were calculated for leucine in the three most probable conformers found in rotamer libraries:[82, 83] χ_1 = -60°, χ_2 = 180° (**mt**, 59% of rotamer library); χ_1 = 180°, χ_2 = 60° (**tp**, 29%); and χ_1 = 180°, χ_2 = 180° (**tt**, 2%). Here **t** = trans, **p** = +60° and **m** = -60° torsion angles, following Lovell et al.[83] and for valine in the three most probable χ_1 conformers: χ_1 = 180 (**t**, 73% of rotamer library); χ_1 = -60 (**m**, 20%); and χ_1 = +60 (**p**, 6%). The methods used to compute these shielding surfaces have been described previously[72]. Calculations used a series of *N*-formyl-L-amino acid amide fragments, which are energy minimized by using an AMBER[84, 85] forcefield in the Discover module imbedded in Insight II (Molecular Simulations, Inc., San Diego, CA). The energy minimized structures were then used as input structures for evaluation of the chemical shielding surfaces using Gaussian-98[86]. A locally dense basis set approach[87] was employed using a 6-311++G(2d,2p)/6-31G scheme, with the larger basis placed on C^α and its neighboring atoms, as depicted in the following diagram for the leucine fragment: These shielding surfaces along with the previously reported alanine surfaces[72] can be found at http://waugh.cchem.berkeley.edu/~bob.

res.	compound	δ_{11}	δ_{22}	δ_{33}	δ_{11-33}
Ala	**1** Boc-V*AL-Aib-VAL-OMe[a]	73.8	52.0	32.5	41.3
	2 Boc-V*AL-Aib-VAL-OMe[b]	73.0	51.3	32.6	40.4
	3 G*AV[c]	76.9	55.4	25.5	51.4
	4 A*AA[c]	70.2	54.9	23.6	46.6
	5 A*AA hemihydrate[c]	71.0	55.8	24.0	47.0
Val	**6** Boc-VAL-Aib-*VAL-OMe[a]	79.1	62.8	38.2	40.9
	7 Boc-VAL-Aib-*VAL-OMe[b]	78.7	61.8	38.0	40.7
	8 LL*VY-OMe	79.3	57.1	39.8	39.5
Leu	**9** Boc-VA*L-Aib-VAL-OMe[a]	71.4	54.8	40.2	31.2
	10 Boc-VA*L-Aib-VAL-OMe[b]	71.5	57.7	36.1	35.4
	11 L*LVY-OMe	71.6	50.9	31.3	40.3

Table 6.1: Experimentally Measured $^{13}C^{\alpha}$ Chemical Shift Tensor Information for Ala-, Val-, and Leu-containing Peptides. [a]Crystallized from MeOH-H_2O. [b]Crystallized from DMSO-2-propanol. [c]Experimental values from Ref.[71]

In order to obtain the tensor orientations necessary for conversion of solid state δ_{ii} to solution $\Delta\sigma*_{exp}$ values, individual calculations were performed for the eleven labeled sites in the polypeptides of interest, shown in Table 6.1. These calculations utilized the energy minimized amino acid model compound with the ϕ,ψ torsion angles set to corresponding crystallographic values, while the χ_1/χ_2 torsion angles were set to the nearest staggered energy minimum value ($\pm 60°$, $180°$).

Calculations were performed on Silicon Graphics Origin 200 (Mountain View, CA) computers and on the Silicon Graphics Origin 2000 and HP-Convex Exemplar SP-2000 (Hewlett Packard Company, Palo Alto, CA) computers located in the National Center for Supercomputing Applications (NCSA) in Urbana, IL.

6.3.2 Results and Discussion

We first investigated the $^{13}C^{\alpha}$ shift tensor elements in the following peptides (Table 6.2): Boc-V*AL-Aib-*VAL-OMe (MeOH/water) (**1**,**6**), Boc-V*AL-Aib-*VAL-OMe

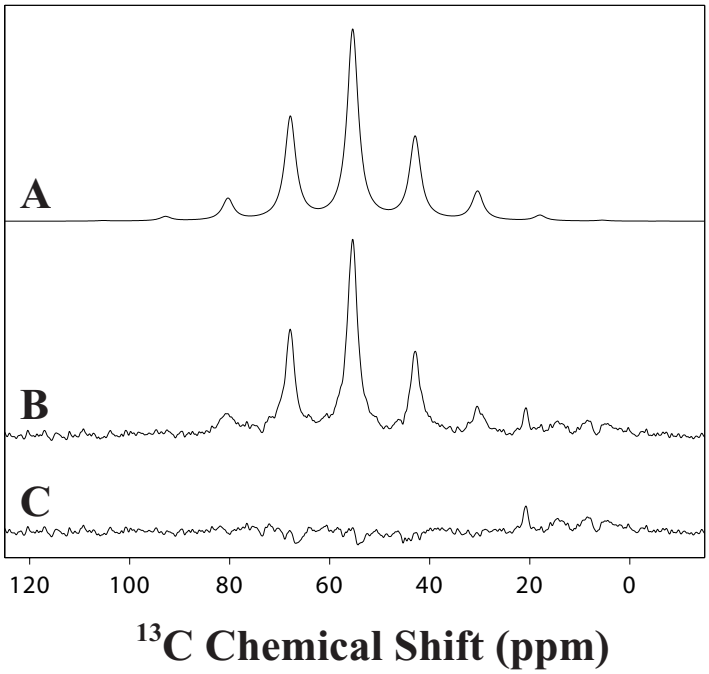

Figure 6.3: ^{13}C CP-MAS NMR results for ^{13}C-labeled Boc-VA*L-Aib- VAL-OMe. (A), Computer simulation of experimental spectrum, (B). The MAS spinning rate was 935 Hz, and the spectrum in (B) was referenced to $^{13}C_o$ in glycine taken to be at 176.04 ppm downfield from TMS. (C) Difference between (A) and (B).

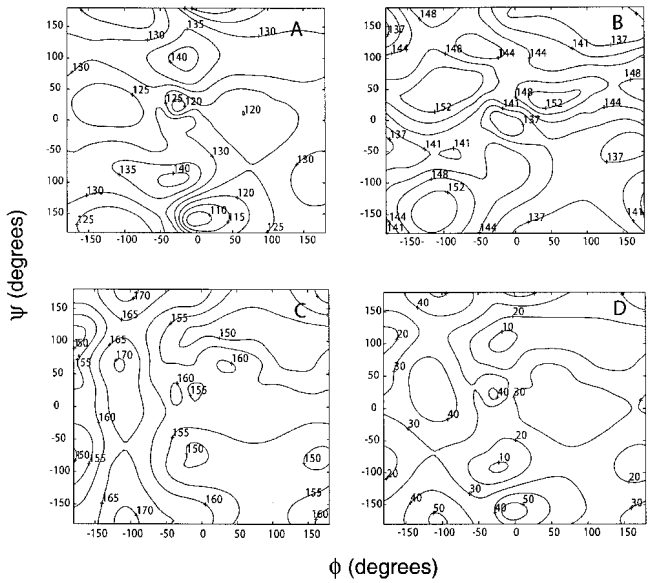

Figure 6.4: Computed shielding surfaces for $^{13}C^{\alpha}$ in N-formyl leucine amide ($\chi_1 = -60°, \chi_2 = 180°$, **mt**, 59% of the protein database), computed by using a Hartree-Fock method with gauge-including atomic orbitals and a locally dense basis set: (A) σ_{11}; (B) σ_{22}; (C) σ_{33}; and (D) $\sigma_{33} - \sigma_{11}$.

(DMSO/isopropanol) (**2,7**), G*AV (**3**), A*AA (**4**) A*AA-hemihydrate (**5**), LL*VY-OMe (**8**), Boc-VA*L-Aib-VAL-OMe (MeOH/water) (**9**), Boc-VA*L-Aib-VAL-OMe (DMSO/isopropanol) (**10**) and L*LVY-OMe (**11**), where the asterisk preceding a letter indicates the presence of a $^{13}C^{\alpha}$-labeled residue. We used magic-angle sample-spinning NMR to obtain spectra at a series of spinning speeds, then used the Herzfeld-Berger[49] method to deduce the principal elements of the $^{13}C^{\alpha}$ shift tensor: δ_{11}, δ_{22} and δ_{33}. A spectrum of Boc-VA*L-Aib-VAL-OMe (**9**) obtained with high-power proton-decoupling is shown in Figure 6.3B, together with its computer simulation (Figure 6.3A) and the difference spectrum, Figure 6.3C. The experimentally determined shift tensor elements for the eight $^{13}C^{\alpha}$ labeled sites in the new compounds together with results for the three alanine-containing peptides reported previously,[71] are shown in Table 6.2.

res.	compound	ϕ	ψ	χ_1	χ_2	σ_{11}	σ_{22}	σ_{33}	Ω	$\Delta\sigma*_{theory}$	$\Delta\sigma*_{exp}$
Ala	**1** Boc-V*Al-Aib-VAL-OMe[a]	-65.4	-44.5			129.30	147.0	162.3	33.0	2.5	1.5
		-61.0	-44.4								
	2 Boc-V*Al-Aib-VAL-OMe[b]	-76.0	-44.0			130.4	145.0	165.2	34.8	7.6	4.4
	3 G*AV	-68.7	-38.1			129.5	146.2	164.5	35.0	6.6	9.2
	4 A*AA	-143.4	160.2			132.9	148.2	165.9	33.0	23.0	28.5
		-164.1	149.0								
	5 A*AA hemihydrate	-145.7	145.5			133.8	149.0	164.7	30.9	22.0	29.1
		-156.2	149.9								
Val	**6** Boc-VAL-Aib-*VAL-OMe[a]	-90.9	1.5	-58.5		121.8	133.6	159.3	37.5	25.0	27.5
		-87.2	-10.8	-61.0							
	7 Boc-VAL-Aib-*VAL-OMe[b]	-109.0	17.0	-56.0		116.7	139.7	164.0	47.3	32.0	28.3
	8 LL*VY-OMe	-123.9	119.7	-179.9		118.9	143.8	158.5	39.6	24.4	29.4
Leu	**9** Boc-VA*L-Aib-VAL-OM[a]	-68.2	-38.4	-176.2	57.3	130.0	142.2	158.5	28.5	11.0	9.1
		-70.8	-35.2	-168.9	61.0						
	10 Boc-VA*L-Aib-VAL-OMe[b]	-62.0	-29.0	-60	180[c]	128.4	141.6	160.4	32.0	7.8	8.6
	11 L*LVY-OMe	-129.4	123.7	-60	180[c]	130.5	146.7	161.3	30.8	26.0	30.1

Table 6.2: X-ray ϕ, ψ, χ_1, χ_2 values[71, 78, 79, 80] and computed $^{13}C^{\alpha}$ shielding tensor values determined from Ramachandran shielding surfaces. [a] Crystallized from MeOH-H2O. [b] Crystallized from DMSO-2-propanol. [c] From molecular mechanics results.

In order to evaluate the theoretical shieldings, we used the alanine shielding surfaces reported previously[72], together with the new leucine and valine surfaces. The individual shielding tensor surfaces $\sigma_{ii}(\phi,\psi)$ and the shielding tensor span surface $\Omega(\phi,\psi)$ for the three most probable conformations of leucine are shown in Figures 6.4-6.7. In Table 6.2, we show the crystallographic ϕ, ψ and χ values and computed shielding tensor values for the 11 C^{α} labeled sites. For alanine, we predicted 15 shielding tensor elements from the experimental ϕ,ψ results for **1-5** and these are shown in Table 6.2 and Figure 6.5A. From Figure 6.5A, we deduce the following relationship between the theoretical shielding tensor elements (σ_{ii}) and the experimental shift tensor elements (δ_{ii}):

$$\sigma_{ii}^{A} = -0.72\delta_{ii}^{A} + 184.6 \quad (R^2 = 0.97) \tag{6.1}$$

where is the theoretical shielding tensor element for $^{13}C^{\alpha}$ in an alanine peptide (in ppm from the bare nucleus) and δ_{ii}^{A} is the experimental chemical shift tensor element (in ppm from tetramethylsilane, TMS). Two shielding surfaces, with χ_1 = -60° and χ_1 = 180°, were then used to evaluate the nine valine $^{13}C^{\alpha}$ shielding tensor elements shown in Tables 6.1 and 6.2 and these results are plotted in Figure 6.5B. From this we deduce the relation:

$$\sigma_{ii}^{V} = -1.03\delta_{ii}^{V} + 200.8 \quad (R^2 = 0.99) \tag{6.2}$$

Clearly, in both alanine and valine, the R^2 values are excellent, with the rms deviations from the fitted line being on average ~2.0 ppm, indicating that the theoretical predictions correlate well with those determined experimentally. For leucine, we computed the three

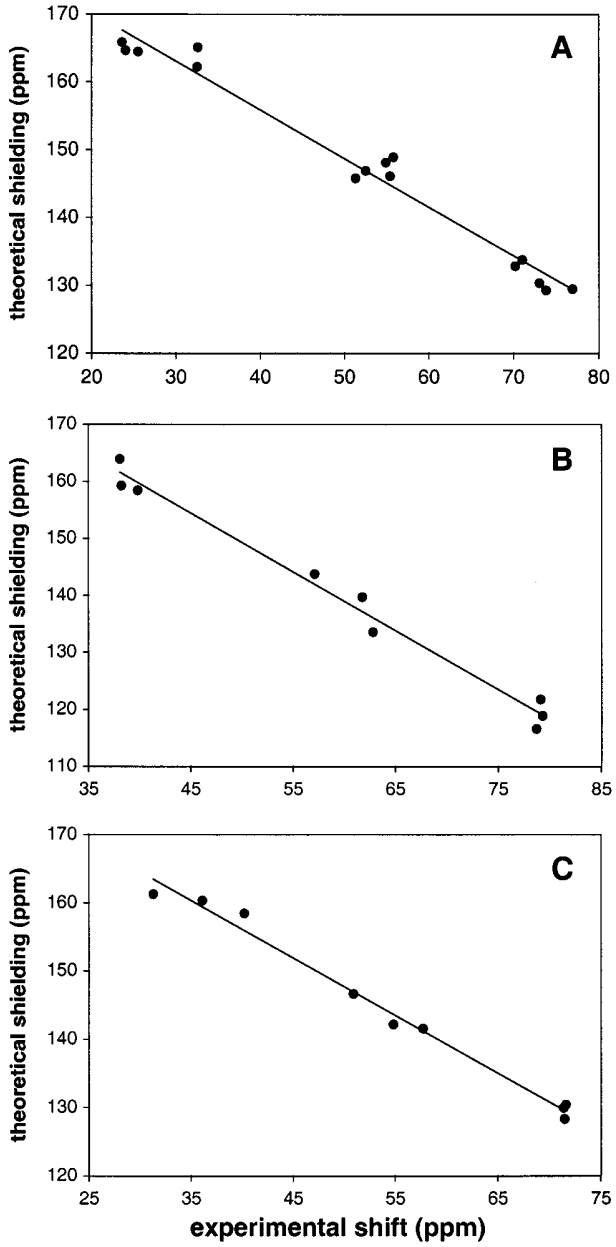

Figure 6.5: Graph showing theoretical $^{13}C^{\alpha}$ chemical-shielding tensor elements for alanine (A), valine (B), and leucine (C) peptides plotted versus the experimentally determined chemical-shift tensors. For (A): slope = -0.72, y-intercept = 184.6ppm, R^2 = 0.97, and rmsd = 2.4 ppm (B): slope = -1.03, y-intercept = 200.8 ppm, R^2 = 0.98, and rmsd = 2.5 ppm. For (C): slope = -0.84, y-intercept = 189.9 ppm, R^2 = 0.99, and rmsd = 1.5 ppm.

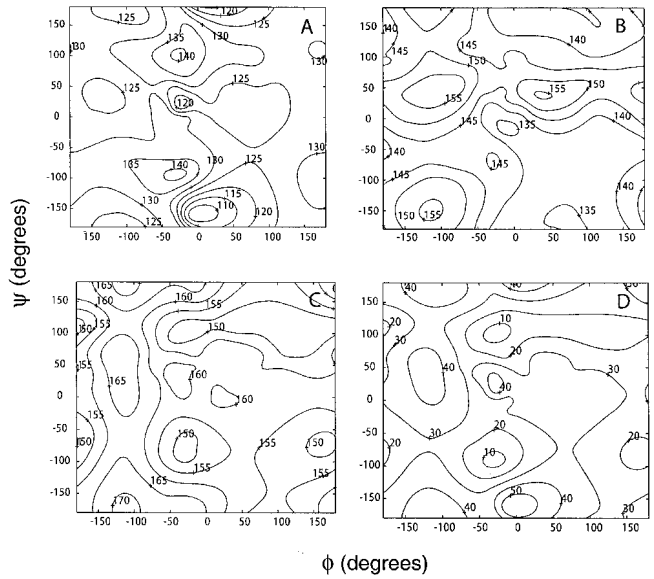

Figure 6.6: Computed shielding surfaces for $^{13}C^{\alpha}$ in N-formyl leucine amide ($\chi_1 = 180°, \chi_2 = 60°$, **tp**, 29% of the protein database), computed by using a Hartree-Fock method with gauge-including atomic orbitals and a locally dense basis set: (A) σ_{11}; (B) σ_{22}; (C) σ_{33}; and (D) $\sigma_{33} - \sigma_{11}$.

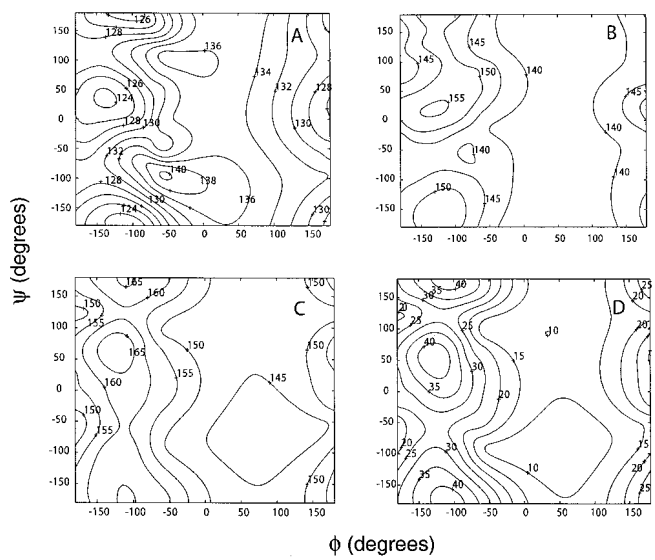

Figure 6.7: Computed shielding surfaces for $^{13}C^{\alpha}$ in N-formyl leucine amide ($\chi_1 = 180°, \chi_2 = 180°$, **tt**, 2% of the protein database), computed by using a Hartree-Fock method with gauge-including atomic orbitals and a locally dense basis set: (A) σ_{11}; (B) σ_{22}; (C) σ_{33}; and (D) $\sigma_{33} - \sigma_{11}$.

major shielding surfaces[83][84]: χ_1 = -60°, χ_2 = 180° (**mt**, 59% of the protein data base); χ_1 = 180°, χ_2 = 60° (**tp**, 29% of the data base) and χ_1 = 180°, χ_2 = 180° (**tt**, 2% of the protein data base). Unlike the situation found with the two valine-containing peptides, the x-ray crystallographic results for leucine showed leucine sidechain disorder in two out of three three peptides investigated, and we did not obtain crystals suitable for a re-analysis of this question. Fortunately, however, the shielding surfaces for the major conformations, Figures 6.4-6.7, are rather similar and we find good correlations between all nine experimental shifts and their corresponding computed shielding tensor elements when using either the most probable **mt** or **tp** surfaces. That is, the $^{13}C^{\alpha}$ shielding tensor is primarily sensitive to ϕ,ψ changes, not to differences in χ_1 and χ_2. In **9**, only the **tp** conformers are present (2 molecules per unit cell) but in **10** there are four conformers (including the most populated **mt** and **tp** species) and in **11** there are two. Fortunately, however, as noted above and as shown in Figures 6.4-6.7, the $^{13}C^{\alpha}$ shielding tensors are relatively insensitive to χ_1/χ_2 for this amino-acid (unlike the situation with e.g. isoleucine), and use of either of the most populated (**mt**, **tp**) surfaces produces very similar $^{13}C^{\alpha}$ shielding tensor results. For example, using the **mt** (χ_1 = -60°, χ_2 = 180°) surface we obtain a slope = -0.87, an intercept = 191.5 ppm and an R^2 value = 0.97, and a rmsd from the fitted line of 2.4 ppm. For the **tp** surface (χ_1 = 180°, χ_2 = 60°) we obtain a slope = -0.82, an intercept = 188.9 ppm, an R^2 value = 0.98 and an rmsd = 1.7 ppm.

However, it is of course most appropriate to try to use the actual or most probable conformers. For **9**, we used the **tp** surface to generate the theoretical shielding results shown in Table 6.2, since there is only a single conformer in the crystal. For **11**, there are two conformers present, however, one of these appeared to have a bad steric contact with the

tyrosine ring in the peptide and on molecular mechanics geometry optimization adopted the **mt** conformation, which was used to generate the shielding results given in Table 6.2. Similarly, **10** was also subjected to molecular mechanics optimization and yielded **mt** as the preferred conformation, again resulting in the shielding results shown in Table 6.2. A graph of the experimental shift versus theoretical shielding tensor elements is shown in Figure 6.5C and can be fitted by:

$$\sigma_{ii}^{L} = -0.84\delta_{ii}^{L} + 189.8 \quad (R^2 = 0.99) \tag{6.3}$$

with an rms error of 1.5 ppm.

When considering all 33 shift tensor element results, we conclude that the quantum chemical shielding calculations generate good correlations between the experimental shift and theoretical shielding tensor values. However, while the R^2 values are in all cases very good (R^2 values of ∼0.99, on average), there are clearly small systematic errors in the slopes, which range from –0.72 to –1.03 (versus the ideal value of –1.00). This effect has been discussed previously[64] and we have proposed that since the R^2 values are so good, it is appropriate to simply use regression curve slopes and intercepts to scale the quantum chemical results in order to arrive at accurate predicted shift values.

Using the appropriate scalings from the regression curves (Equations 6.1 -6.3), we obtained the experimental shift versus theoretical shift tensor element results shown in Figure 6.8, where there is clearly very good agreement for all 33 $^{13}C^{\alpha}$ shift tensor elements in alanine, valine and leucine fragments. Also of interest from these results, and those shown in Table 6.2, is the observation that while the expected isotropic shift/shielding difference between helical and sheet residues is seen in each case, i.e. the sheets are ∼3-4

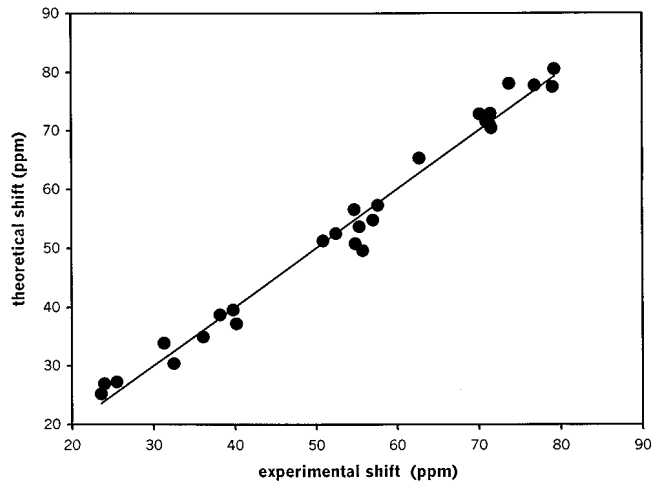

Figure 6.8: Theory versus experiment comparison of chemical shift tensor elements for Ala, Val and Leu peptides. The theoretical chemical shifts are corrected by use of Equations 6.1-6.3. Slope = 1.00, y-intercept = -0.12 ppm, R^2 = 0.99, and rmsd = 2.7 ppm.

ppm more shielded than are helical $^{13}C^{\alpha}$ residues, there is no evidence for any "narrow" helical $^{13}C^{\alpha}$ CSAs or Ωs. The reasons for the lack of large helix-sheet CSA differences are as follows. First, in the case of alanine, we have already demonstrated both experimentally and theoretically that there are no major helix/sheet tensor anisotropy differences seen[71, 72]. Second, in the case of the three valine residues investigated, **6** is a χ_1 = **-60**° distorted helix (ϕ = -87°, ψ = -11°, molecule 1; ϕ = -91°, ψ = 2°, molecule 2). The average Ω for these two species (from the shielding surfaces) is 38.8 ppm. The second valine species, **7**, is a χ_1 = -60° distorted sheet (ϕ = -109°, ψ = 17°). The Ω for **7** from the shielding surfaces is 47.3 ppm. The final valine species, **8**, is a χ_1 = 180° sheet (ϕ = -124°, ψ = 120°). The Ω for **8** from the shielding surfaces is 39.6 ppm, in general accord with the 37.4 previously reported for the ϕ = -120°, ψ = 120° χ_1 = 180° sheet[72]. In the case of the three leucine species, **9-11**: **9** and **10** have helical ϕ,ψ values while **11** has sheet values (Table 6.2). However, as demonstrated by both experiment (Table 6.1) and theory (Table 6.2) there are in fact no

major differences in Ω between helical and sheet geometries. In sharp contrast, helical and sheet leucine $\Delta\sigma^*$s determined via solution NMR do vary widely with conformation. The reason for these differences must therefore reside in the definition of the "CSA".

According to Jameson[88], Ω is the difference between the most shielded (σ_{33}) and the least shielded tensor component (σ_{11}), corresponding to the width of the resonance powder pattern in ppm, Ω=(σ_{33}-σ_{11}), where $\sigma_{33} \geq \sigma_{22} \geq \sigma_{11}$ and σ is the chemical *shielding*, and Ω=(δ_{11}-δ_{33}), where δ is the chemical *shift*.

Previously, Ω was to describe shielding tensor differences between helices and sheets, which is used in CSA-based dephasing experiments[73], where the dephasing observed is a function of Ω. Relaxation based measurement of the CSA in solution NMR is, however, sensitive to different components of the CSA. Here, a CSA or $\Delta\sigma^*$ has been defined as $\Delta\sigma^* = \sigma_{orth}$-$\sigma_{par}$, where σ_{par} is the shielding parallel to the C^α-H^α bond vector and σ_{orth} is the average shielding orthogonal to the C^α-H^α bond vector. However, if we know the angles between σ_{ii} and the C^α-H^α bond vector, the shielding tensor can be projected onto this axis by using the following rotation:

$$\sigma_{par} = \begin{bmatrix} d_1 & d_2 & d_3 \end{bmatrix} \begin{bmatrix} \sigma_{11} & 0 & 0 \\ 0 & \sigma_{22} & 0 \\ 0 & 0 & \sigma_{33} \end{bmatrix} \begin{bmatrix} d_1 \\ d_2 \\ d_3 \end{bmatrix} \tag{6.4}$$

where σ_{ii} are the shielding tensor elements in the principal axis system and d_i are the direction cosines of the C^α-H^α bond with respect to the principal axes. When combined

with Eq. (6.5)[75]:

$$\Delta\sigma* = \sigma_{orth} - \sigma_{par} = 1.5 * (\sigma_{iso} - \sigma_{par}) \tag{6.5}$$

$\Delta\sigma^*$ can therefore in principle be calculated from σ_{11}, σ_{22}, σ_{33} and the direction cosines. Unfortunately, in simple solid state MAS NMR experiments, only the magnitudes of the shift tensor elements are obtained in the PAS and not the molecular frame, so the solid state NMR Ω information cannot immediately be transformed to the solution NMR $\Delta\sigma^*_{\text{exp}}$ by means of Equations 6.4 and 6.5. However, it seems reasonable to utilize the tensor orientations (d_1, d_2, d_3) we obtain from *ab initio* calculations to effect this transformation, since in previous work there has been excellent agreement between single crystal shielding tensor results and theoretical shielding tensor results in the amino-acid threonine[89]. Therefore, using Eq. (6.6), $\Delta\sigma^*{}_{exp}$ for the eleven labeled sites can be computed from the solid-state NMR $\delta_{ii}{}^{exp}$ results as:

$$\Delta\sigma^*_{par} = -1.5 \times \left(\delta^{exp}_{iso} - \begin{bmatrix} d_1 & d_2 & d_3 \end{bmatrix} \begin{bmatrix} \delta^{exp}_{11} & 0 & 0 \\ 0 & \delta^{exp}_{22} & 0 \\ 0 & 0 & \delta^{exp}_{33} \end{bmatrix} \begin{bmatrix} d_1 \\ d_2 \\ d_3 \end{bmatrix} \right) \tag{6.6}$$

Clearly, from Eq. (6.6) above, the orientation of the principal axis can significantly affect the values of $\Delta\sigma^*$. As may be seen in Figure 6.9, the computed C^α shielding tensor orientations in leucine do vary dramatically with ϕ,ψ, and consequently the shieldings along the C^α-H^α bond axis also vary considerably. This of course explains why *ab initio* quantum chemical calculations of protein solution NMR $\Delta\sigma^* = \sigma_{orth}$-$\sigma_{par}$ values using an alanine model are in

generally good agreement with experiment[66], even though the $\Delta\sigma \approx \Omega = \sigma_{33}$-$\sigma_{11}$ values are relatively insensitive to ϕ,ψ, both experimentally[71] and theoretically[71, 72]. That is, the alanine tensor orientation changes overwhelmingly dominate the helical/sheet $\Delta\sigma^*$ changes, because alanine is not a β-branched amino-acid and is therefore a good model for the great majority of amino-acids.

To demonstrate this effect more clearly, shown in Figure 6.10 is the $\Delta\sigma^*{}_{exp}$ (Eq. (6.6) and purely theoretical $\Delta\sigma^*$ values (Table 6.2) for the eleven labeled sites investigated, together with solution NMR results for Ala, Val and Leu in the protein ubiquitin. The solid state $\Delta\sigma^*{}_{exp}$ values were obtained by combining the experimental δ_{ii} with the theoretical direction cosines, as shown in Eq. (6.6). The ubiquitin solution $\Delta\sigma^*{}_{exp}$ values are those reported by Tjandra and Bax[75]. The $\Delta\sigma^*$ (theoretical) values were read from the theoretical $\Delta\sigma^*$ surfaces. When cast in terms of solution $\Delta\sigma^*$ values, the solid-state results are clearly indistinguishable from the solution NMR results. Thus, although $\Delta\sigma = \Omega$ for leucine is essentially independent of whether $^{13}C^{\alpha}$ is in a helical or sheet conformation (Ω ~37 ppm on average from experiment, ~30 ppm from calculation), $\Delta\sigma^*$ (solution) varies from ~5 to 38 ppm (from Ref. 12), as does the solid-state derived $\Delta\sigma^*$ (~10-30 ppm, Table 6.2). These results have important implications for investigations of Ω in other amino-acids in peptides or proteins, in particular for their use in spectral editing or in deriving structural information. For example, in recent solid-state NMR studies of ubiquitin,[73] it has been shown that there are large differences in signal dephasing which depend on Ω, with β-sheet $^{13}C^{\alpha}$ signals decaying first. In one spectral region, Gln-40, Glu-41 and Phe-4 all decayed rapidly, consistent with a large Ω (all are non β-branched residues). Similarly, in another spectral region, Val-70 (sheet, $\chi_1 = 180°$) and Ile-13 (sheet, $\chi_1 = 126°$) also

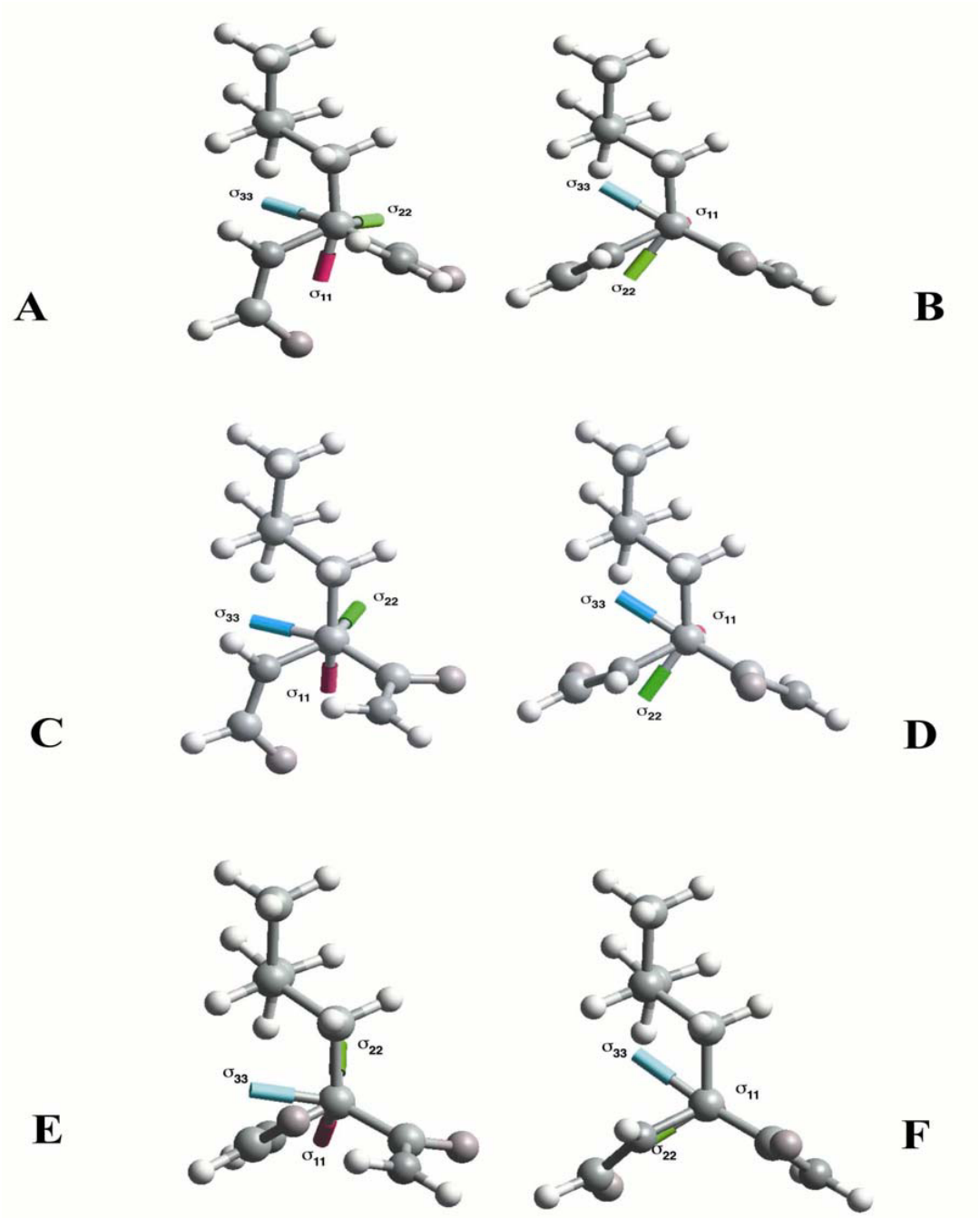

Figure 6.9: ^{13}C shielding tensor orientations for fragments investigated. (A) Ideal leucine helix geometry (ϕ= -60, ψ= -60); $\Delta\sigma$= 28.1 ppm, $\Delta\sigma*$= 1.34 ppm; (B) Ideal sheet geometry (ϕ= -120, ψ= 120); $\Delta\sigma$= 34.8 ppm, $\Delta\sigma*$= 26.8 ppm; (C) Compound 10 (ϕ= -62, ψ= -29); $\Delta\sigma$= 32.0 ppm, $\Delta\sigma*$= 7.8 ppm; (D) Compound 11 (ϕ= -129, ψ= 124); $\Delta\sigma$= 30.8 ppm, $\Delta\sigma*$= 26.0 ppm; (E) Ubiquitin Leu56 (ϕ= -61, ψ=-36); $\Delta\sigma$= 32.0 ppm, $\Delta\sigma*$= 6.5 ppm and (F) Ubiquitin Leu 69 (ϕ= -107, ψ= 116); $\Delta\sigma$= 34.1 ppm, $\Delta\sigma*$= 25.7 ppm.

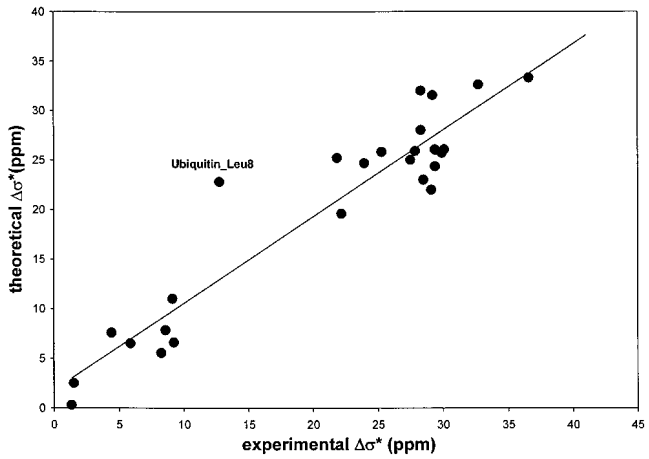

Figure 6.10: Theory versus experiment comparison of the C^{α} solution CSA ($\Delta\sigma^* = \sigma_{orth}$-$\sigma_{par}$) for Ala, Val, Leu in ubiquitin and 9 peptides. Slope = 0.87, y-intercept = 1.8 ppm, $R^2 = 0.90$, and rmsd = 3.4 ppm. The outlier is in ubiquitin.

decayed rapidly (sheet Ωs, even for β-branched amino-acids, are large), while Ile-23 (helix), Val-26 (helix) and Ile-30 (helix) all remained prominent, consistent with small Ωs. The helical residues Lys-33, Glu-34 and Tyr-59 were apparently exceptions, however, this may be attributable to the fact that all three amino-acids have similarly large helix, sheet tensor spans, since they are not β-branched[77].

6.3.3 Conclusions

The results presented above are of interest for a number of reasons. Not only have we obtained experimental $^{13}C^{\alpha}$ shielding tensor results for unbranched (alanine, leucine) and β-branched (valine) amino-acids in peptides using magic-angle sample spinning techniques, but we find good correlations between these experimental shielding results and those computed theoretically. Our results with the unbranched amino-acids alanine and leucine show very similar $^{13}C^{\alpha}$ tensor magnitudes for helical and sheet conformations, but with different

tensor orientations. This is to be compared with previous results with valine, isoleucine and threonine, in which small $^{13}C^{\alpha}$ tensor spans (Ω) were predicted for helical (but not sheet) residues, for the most popular conformations. The lack of large variations in Ω for non-β branched amino-acids may be a general one and has implications for structural studies or solid-state spectral editing experiments based on Ω. Finally, we were able to clarify differences between the solution state derived $\Delta\sigma^*$ and the solid state definition of the CSA. Our results show that there is good agreement between experimental and theoretical $\Delta\sigma^*$ values for alanine, valine and leucine residues in ubiquitin (solution NMR) and in a series of peptides (solid-state MAS NMR σ_{ii} determination, ab initio tensor orientation). The broad range of $\Delta\sigma^*$ but essentially constant Ω values are well reproduced in the calculations. The range in $\Delta\sigma^*$ in solution NMR experiments is overwhelmingly dominated by changes in the $^{13}C^{\alpha}$ tensor orientation with ϕ,ψ. An exciting prospect of the sensitivity of the CSA tensor and its orientation to ϕ and χ is that this may allow the CSA to be used as an effective structural refinement tool. Advances in cross-correlated relaxation measurement in solution have shown that both the shift tensor and its orientation can be determined in proteins[90] and further work utilizing the results presented here is currently underway.

Chapter 7

Dipolar Coupling Measurements in the Solid State

7.1 Introduction

As mentioned in previous chapters, many interactions, such as the dipole-dipole interaction, depend upon the orientation of the Zeeman field with respect to the Principal Axis System (PAS) of the particular interaction. The resulting "secular" contributions from these interactions are typically anisotropic which leads to broad spectra when dealing with powdered samples. In the past, there have been numerous attempts to make anisotropic interactions isotropic without removing the interaction. These methods can be put into three different directions of approach. The first approach was introduced by Bloom in the early 80's and involved a mathematical transformation of the NMR powder spectrum, a method referred to as "de-Pake-ing"[91]. These transforms suffered from noise contamination which sometimes gave unreliable results. The second method was introduced by the Pines' group

and involved actually having the system evolve in zero-field[92, 21]. The spin system was prepolarized in a high-field magnet and then mechanically shuttled outside of the magnet to evolve under the zero-field Hamiltonian. The same was then shuttled back into high-field for detection. This method has been demonstrated in a variety of experiments, and it has been shown to be successful in a variety of applications. However, it is experimentally quite demanding, and zero-field manipulations of spin interactions tend to be more complex than their high-field counterparts. Finally, the third class of experiments have dealt with trying to remove the anisotropy using mechanical rotation and radiofrequency (RF) pulses while still staying in high-field. Tycko showed in a series of papers how an average Hamiltonian proportional to the zero-field Hamiltonian could be constructed in high-field for a dipole-coupled spin system via a suitable choice of rotor synchronized RF pulses[93, 94, 95]. In this chapter,an alternative to Tycko's zero-field in high-field methodology is presented which produces an isotropic dipolar spectrum for a pair of dipole coupled spins while in high-field. This method, called HOMonuclear Isotropic Evolution (HOMIE) works by removing the anisotropic component of the dipolar frequencies by a suitable combination of average Hamiltonians and evolution pathways. In the following chapter, Tycko's Zero-Field in High-Field methodology is first briefly reviewed. Next, the theory and implementation of HOMIE is presented which provides isotropic dipolar spectra for a homonuclear spin pair. Then, an extension of the method to obtain isotropic local field spectra for an $I_N S$ spin system is presented.

7.2 Tycko's Zero-Field in High-Field

As was shown in an earlier chapter, the zero-field Hamiltonian for a dipole coupled spin pair is given by In zero magnetic field, the dipolar Hamiltonian for a pair of spins is given by

$$\begin{aligned} H_D^{\mathrm{ZF}} &= -\omega_D(\vec{I^1}\cdot\vec{I^2} - 3(\vec{I^1}\cdot\hat{r}_{12})(\vec{I^2}\cdot\hat{r}_{12})) \\ &= \omega_D \sum_{m=-2}^{2} (-1)^m A_{2,m}^{12}(\theta_{12},\phi_{12}) T_{2,-m}^{12} \end{aligned} \tag{7.1}$$

where $\hat{r}_{12}$ is the internuclear unit vector between spins 1 and 2, $\omega_D = \frac{\gamma_1\gamma_2}{|r_{12}|^3}$ is the dipole coupling, $A_{2,m}^{12}(\theta_{12},\phi_{12})$ and $T_{2,m}^{12}$ are second rank spatial and spin tensors respectively, and (θ_{12},ϕ_{12}) are polar angles relating the magnetic field quantization axis to the internuclear vector. As can be shown by using the rotation operators (described in more detail in [96]), H^{ZF} is a scalar , i.e., it is invariant to rotations to the combined rotation of space and spin. This can be seen as follows: H^{ZF} transforms under the rotation $R = R_{\mathrm{Space}}R_{\mathrm{Spin}}$ as follows:

$$\begin{aligned} R^\dagger H^{\mathrm{ZF}} R &= \sum_{n=-2}^{2} R_{\mathrm{Space}}^\dagger (-1)^n A_{2,n} R_{\mathrm{Space}} R_{\mathrm{Spin}}^\dagger T_{2,-n} R_{\mathrm{Spin}} \\ &= \sum_{n=-2}^{2}\sum_{m=-2}^{2}\sum_{p=-2}^{2} (-1)^n A_{2,p} T_{2,m} R_{p,n} R_{m,-n} \\ &= \sum_{m=-2}^{2}\sum_{p=-2}^{2} (-1)^p \delta_{m,-p} A_{2,p} T_{2,m} \\ &= \sum_{m=-2}^{2} (-1)^m A_{2,m} T_{2,-m} \end{aligned} \tag{7.2}$$

For two spin 1/2 particles, the eigenvalues of H_D^{ZF} are independent of θ_{12} and ϕ_{12}, which even for a powdered sample, result in three sharp lines, as shown in Figure 7.1A.

Under high-field conditions ($\gamma B \gg \omega_D$) the Hamiltonian is truncated by the Zeeman interaction which is typically the case for NMR experiments. However, the Zeeman interaction, $H_{\text{Zeeman}} = \gamma \vec{B_0} \cdot \vec{I}$, destroys the isotropy of spin and space. In high magnetic fields where $|\gamma B_0| \gg |\omega_D|$, the dipolar interaction is treated as a perturbation to the Zeeman interaction, causing H_D^{ZF} in Eq. (7.2) to be effectively truncated along the Zeeman field. Taking the Zeeman field, $\vec{B_0}$ to be along the z axis, the "secular" part of the dipolar Hamiltonian, H_D^{HF}, is given by

$$H_D^{\text{HF}} = \omega_D A_{2,0}^{12}(\theta_L, \phi_L) T_{2,0}^{12} = \omega_D \frac{3\cos(\theta_L)^2 - 1}{2}(3I_Z^1 I_Z^2 - \vec{I^1} \cdot \vec{I^2}) \tag{7.3}$$

where θ_L is the angle that the internuclear vector makes with respect to the Zeeman field. For two spin 1/2 nuclei, the resulting spectra under H^{HF} gives a "Pake" pattern for a powdered sample as shown in Figure 7.1B.

The high-field Hamiltonian does contain a component of the zero-field Hamiltonian. If H^{HF} is represented by the vector $\langle H^{\text{HF}}| = (0,0,1,0,0)$ and $\langle H^{\text{ZF}}| = (1,-1,1,-1,1)$, where $\langle A_{2,2}T_{2,-2}| \equiv (1,0,0,0,0)$,$\langle A_{2,1}T_{2,-1}| \equiv (0,1,0,0,0)$, etc. Then the amount of zero-field Hamiltonian contained in the high-field Hamiltonian is simply given by

$$\begin{aligned} \sigma &= \frac{\langle H^{\text{ZF}}|H^{\text{HF}}\rangle}{\langle H^{\text{ZF}}|H^{\text{ZF}}\rangle} \\ &= \frac{1}{5} \end{aligned} \tag{7.4}$$

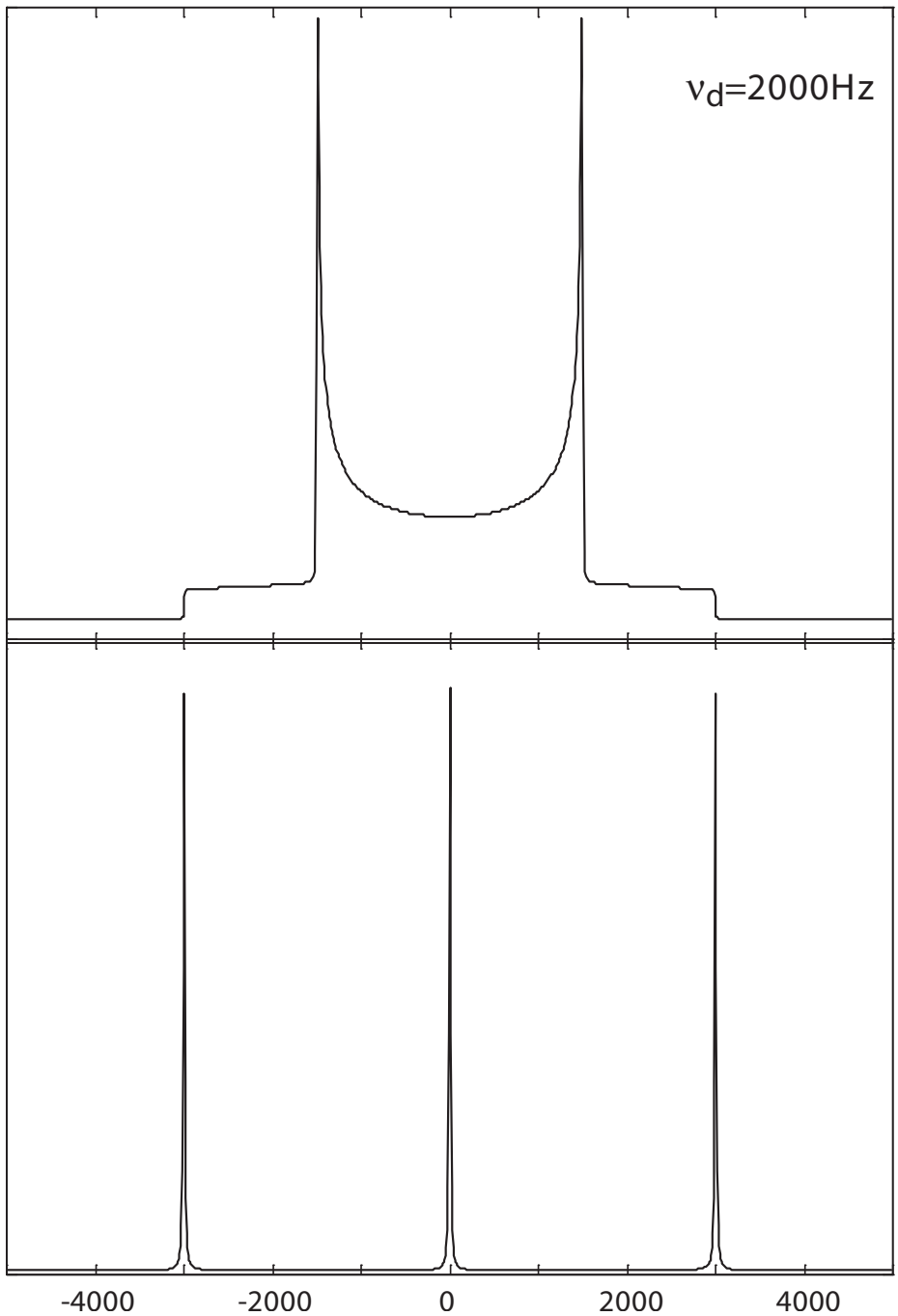

Figure 7.1: Simulated spectra for a dipole coupled spin system in (A) zero-field and (B) high-field conditions. An $\omega_D/(2\pi) = 2000$ Hz was used. (A) The zero-field consists of three sharp lines at frequencies at 0 Hz and ± 3000 Hz. (B) Pake pattern for a dipole coupled spin system, where the spread in frequencies is due to the anisotropy of H_D^{HF} in Eq. (7.3).

Thus H^{HF} can be written as

$$\begin{aligned} H^{\mathrm{HF}} &= \frac{1}{5}H^{\mathrm{ZF}} + \left(H^{\mathrm{Rest}}\right) \\ H^{\mathrm{Rest}} &= H^{\mathrm{HF}} - \frac{1}{5}H^{\mathrm{ZF}} \end{aligned} \tag{7.5}$$

This means that the zero-field Hamiltonian can be obtained from the high-field Hamiltonian with maximum scaling of $\sigma = 1/5$ if H^{Rest} could be removed from H^{HF}. To see how this can be accomplished, it is useful to rewrite H^{HF} in the coupled "basis" of space and spin, following the original derivation given by Tycko. H^{HF} can be written in the coupled basis of spin-space as

$$\begin{aligned} H^{\mathrm{HF}} &= \omega_D A_{2,0} T_{2,0} \\ &= \omega_D \sum_{l=0,2,4} C(l,0,2,0,2,0) F_{l,0} \end{aligned} \tag{7.6}$$

where $C(l,0,2,0,2,0)$ are the Clebsch-Gordan coefficients relating the spin and space Hamiltonian to the spin-space Hamiltonian. By the addition of angular momentum, the only possible total angular momentum values are $l = |2+2| = 4,3,2,1,|2-2| = 0$. However, due to the fact H^{HF} is even under parity ($I \to -I$ and $\theta_{12} \to \pi - \theta_{12}, \phi_{12} \to \pi + \phi_{12}$), all odd l terms are zero (i.e., the corresponding Clebsch-Gordan coefficients are zero).

Thus H^{HF} can be written as the sum of zeroth, second, and fourth rank terms. The zeroth order term is proportional to H^{ZF} by the normalization factor of $1/\sqrt{5}$. As expected, $C(0,0,2,0,2,0) = 1/\sqrt{5}$, which again gives the total amount of zero-field Hamiltonian in H^{HF} as $1/5$, consistent with Eq. (7.4). The second and fourth rank terms can be removed

by a combination of rotor synchronized pulses as was numerically discovered by Tycko[95]. Under the constraint of mechanically spinning the sample about only one rotor axis, Tycko found a solution that gave a corresponding scaling factor of $\sigma_{Tycko} = 0.089$. However, this scaling is less than the theoretical maximum of $\sigma = 1/5$. It was later realized by Tycko and Sun and Pines that the maximum scaling could be obtained by forcing the spins to evolve under "Dynamic-Angle Spinning" (DAS) like trajectories or "Double-Rotation" (DOR) like trajectories. Such techniques were used previously[97] to remove the anisotropic second and fourth rank components of the second order quadrupolar interaction, while keeping the chemical shift and isotropic second order quadrupolar interaction. However, actual implementations of such trajectories to create the zero-field Hamiltonian are not experimentally feasible for a variety of reasons. First of all, unless the RF powers are exceedingly large, the scaling factor will always be less than 1/5. . Second of all, the DOR technique suffers from instability of the sample rotation since the sample has to simultaneously rotate about two axes at once, thus requiring very slow spinning speeds in order to work stably. A DAS solution, however, suffers from the necessity to hop back and forth between angles repeatedly in order for the average Hamiltonian treatment to be valid. To see this, assume that for two separate angles, θ_1 and θ_2, one creates $\overline{H}(\theta_1)$ for a time t_1 and $\overline{H}(\theta_2)$ for a time t_2 respectively such that an average Hamiltonian

$$\begin{aligned} \overline{H} &= \frac{1}{(t_1+t_2)}(t_1\overline{H}(\theta_1)+t_2\overline{H}(\theta_2)) + O[\omega_D(t_1+t_2)] \\ &= \sigma H_D^{\mathrm{ZF}} + O[\omega_D(t_1+t_2)] \end{aligned} \tag{7.7}$$

is created. The validity of the average Hamiltonian treatment requires that the cycle time,

$t_c = t_1 + t_2$ be small enough such that $|\omega_D t_c| \ll 1$. Due to the fact that switching sample rotation between the angles θ_1 and θ_2 takes on the order of tens of milliseconds, the sample cannot be repeatedly switched between the two angles during the course of the experiment. For typical dipolar couplings, in order to maintain the condition $|\omega_D t_c| \ll 1$ many angle switching periods would be required for the average Hamiltonian treatment, which is unrealistic experimentally. Hence there appears to be no clear way to implement experimentally a DAS-like trajectory in order to obtain the zero-field Hamiltonian.

Therefore, we develop the HOMonuclear Isotropic Evolution (HOMIE) method which works by removing the anisotropic component of the dipolar frequencies by a suitable combination of average Hamiltonians and evolution pathways described below.

7.3 Isotropic Homonuclear Recoupling (HOMIE)

The general method for obtaining isotropic dipolar spectra is shown in Figure 7.2. Consider a pair of homonuclear dipole coupled spins with the initial density matrix, $\rho(0) = I_Z = I_Z^1 + I_Z^2$, evolving under the Hamiltonian, H, which is given by

$$H = \omega_D h(\theta) \left(3 I_X^1 I_X^2 - \vec{I}^1 \cdot \vec{I}^2 \right) \tag{7.8}$$

where $h(\theta) = k \frac{3\cos^2(\theta) - 1}{2}$, and k is the scaling factor associated with the particular RF pulse sequence used to generate H from H_D^{HF}. After evolution under H for a time t, $\rho(t)$ is given

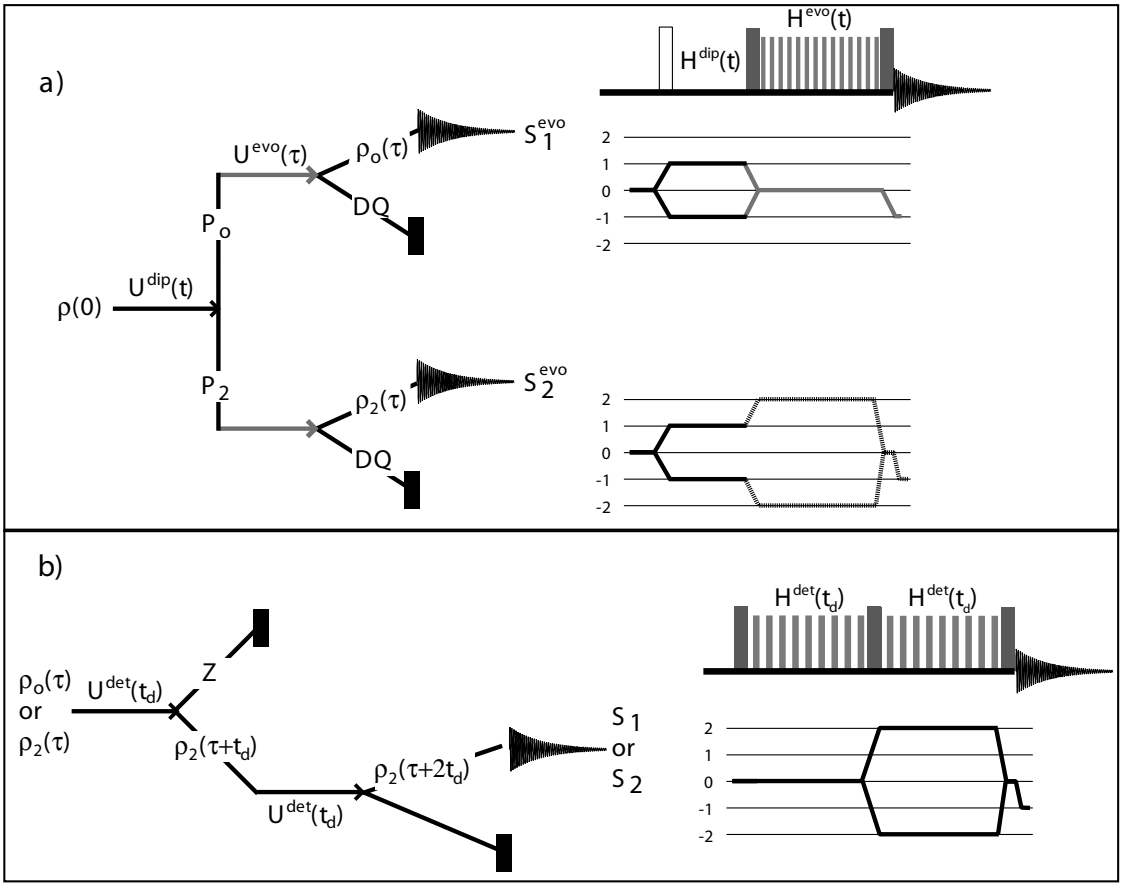

Figure 7.2: The Basic procedure in order to obtain isotropic dipolar spectra. An initial density matrix, $\rho(0) = I_Z$ evolves under H [Eq. (7.8)] to give a z-magnetization (Z) term, (ρ_0), and double-quantum (DQ) term, (ρ_2). Both of these terms then evolve under H^{EVO} [Eq. (7.10)] and only the Z components are kept. Next, evolution occurs from Z_0 and Z_2 under H_1^{DET} into DQ coherence. The DQ coherences are then converted back into z-magnetization for detection, using either H_1^{DET} for the pathway originating from ρ_0 or H_{-1}^{DET} for the pathway originating from ρ_2.

by:

$$\begin{aligned}\rho(t) &= \cos\left(\frac{3}{2}\omega_D h(\theta)t\right) I_Z + i\sin\left(\frac{3}{2}\omega_D h(\theta)t\right)(T_{2,2} - T_{2,-2}) \\ &= \rho_0(t) + \rho_2(t) \end{aligned} \tag{7.9}$$

where $T_{2,\pm 2} = I^1_\pm I^2_\pm$, $\rho_0(t) = \cos\left(\frac{3}{2}\omega_D h(\theta)t\right) I_Z$, and $\rho_2(t) = i\sin\left(\frac{3}{2}\omega_D h(\theta)t\right)(T_{2,2} - T_{2,-2})$. The signal originating from either ρ_0 or ρ_2 can be distinguished by phase cycling, so in the following the evolution along each pathway will be considered separately.

Consider next the average Hamiltonian, H^{EVO}, of the form

$$H^{\mathrm{EVO}} = \omega_D(gA_{2,-2}T_{2,2} + gA_{2,2}T_{2,-2}) \tag{7.10}$$

where $A_{2,\pm 2} = \frac{3}{4}\sin(\theta)^2 e^{\pm i2\phi}$, and g is a scaling factor that depends on the particular sequence used to generate H^{EVO} from H^{HF}_D. The eigenvalues for H^{EVO} are $\pm\frac{3}{4}g\omega_D\sin(\theta)^2$, which can be used to cancel the anisotropic terms of $h(\theta)$. Evolution of $\rho_0(t)$ under H^{EVO} for a time τ gives

$$\begin{aligned}\langle I_Z(t,\tau)\rangle_0 &= Tr(\rho_0(t,\tau)I_Z) \\ &= \cos(\frac{3}{2}\omega_D h(\theta)t)\cos(\omega_D w(\theta)\tau) \end{aligned} \tag{7.11}$$

where $w(\theta) = \frac{3}{2}g\sin(\theta)^2$. Evolution of $\rho_2(t)$ under H^{EVO} for a time τ gives

$$\begin{aligned}\langle I_Z(t,\tau)\rangle_2 &= Tr(\rho_2(t,\tau)I_Z) \\ &= -\cos(2\phi)\sin(\frac{3}{2}\omega_D h(\theta)t)\sin(\omega_D w(\theta)\tau)\end{aligned} \tag{7.12}$$

The θ dependence in both Eq. (7.11) and Eq. (7.12) involve terms proportional to $\omega_D[h(\theta)t \pm w(\theta)\tau]$ and can be cancelled if

$$\frac{9}{4}kt = \pm\frac{3}{2}g\tau \tag{7.13}$$

Neglecting the trivial solution when $k = g = 0$, Eq. (7.13) implies that at most half of the signal can be made isotropic. Specifically, if the + solution is satisfied from Eq. (7.13), the frequency terms proportional to $\omega_D[h(\theta)t + w(\theta)\tau]$ will be independent of θ, whereas the frequency terms proportional to $\omega_D[h(\theta)t - w(\theta)\tau]$ will not be independent of θ.

Another difficulty arises due to the ϕ dependence of Eq. (7.12). If the $\cos(2\phi)$ factor were absent from Eq. (7.12), then Eq. (7.11) and Eq. (7.12) could be added or subtracted together to give $\cos(\frac{3}{2}\omega_D h(\theta)t)\cos(\omega_D w(\theta)\tau) \mp \sin(\frac{3}{2}\omega_D h(\theta)t)\sin(\omega_D w(\theta)\tau) = \cos[\omega_D(h(\theta) \pm w(\theta)\tau)]$, thus requiring only one of the equations in Eq. (7.13) to be satisfied.

The ϕ dependence in Eq. (7.12) can be overcome by evolution under the Hamiltonians, $H^{\mathrm{DET}}_{\pm 1}$, given by

$$H^{\mathrm{DET}}_{\pm 1} = \omega_D f(A_{2,\pm 1}T_{2,2} - A_{2,\mp 1}T_{2,-2}) \tag{7.14}$$

where $A_{2,\pm 1} = \pm\frac{3}{2}\sin(\theta)\cos(\theta)e^{\pm i\phi}$, and f is some scaling factor that is dependent on the

particular pulse sequence used to generate $H_{\pm 1}^{\mathrm{DET}}$ from H_D^{HF}. After application of H_1^{DET} for a time τ_{DET}, a double-quantum filter is then applied. For the double-quantum coherences originating from $\rho_0(t,\tau)$, H_1^{DET} is applied for a time τ_{DET} to convert the double-quantum coherence into z-magnetization, giving:

$$\langle I_Z(t,\tau,\tau_{\mathrm{DET}})\rangle_0 = -\cos(\frac{3}{2}\omega_D h(\theta)t)\cos(\omega_D w(\theta)\tau)\sin(\omega_D p(\theta)\tau_{\mathrm{DET}})^2 \tag{7.15}$$

where $p(\theta) = 3f\sin(\theta)\cos(\theta)$. For the double-quantum coherences originating from $\rho_2(t,\tau)$, H_{-1}^{DET} is applied for a time τ_{DET} to convert the double-quantum coherence into longitudinal z-magnetization, giving:

$$\langle I_Z(t,\tau,\tau_{\mathrm{DET}})\rangle_2 = \sin(\frac{3}{2}\omega_D h(\theta)t)\sin(\omega_D w(\theta)\tau)\cos(2\phi)^2\sin(\omega_D p(\theta)\tau_{\mathrm{DET}})^2 \tag{7.16}$$

where τ_{DET} is fixed for the experiment. Since to lowest order the frequencies in the t and τ dimensions are independent of ϕ, the powder average over ϕ can be easily performed. For a cylindrically symmetric sample, the signal from Eq. (7.15) is multiplied by $1/2\pi\int_0^{2\pi} d\phi = 1$ whereas the signal in Eq. (7.16) is multiplied by $1/2\pi\int_0^{2\pi}\cos(2\phi)^2 d\phi = 1/2$. The signals originating from ρ_0 [Eq. (7.15)] and ρ_2 [Eq. (7.16)] can then be combined to give

$$\begin{aligned} S_1 \pm 2S_2 &\propto \cos(\omega_D[h(\theta)t \pm w(\theta)\tau]) \\ &= C\cos\left[\frac{3}{4}k\omega_D t(3\cos(\theta)^2 - 1) \pm \frac{3}{2}\omega_D g\sin(\theta)^2\tau\right] \end{aligned} \tag{7.17}$$

where t and τ are chosen to satisfy only *one* of the equations in Eq. (7.13). This gives a

scaling factor σ of

$$\sigma = \frac{3kt}{2(t+\tau)} \tag{7.18}$$

Due to the H_{DET} steps, the total signal is attenuated by the factor C given by

$$\begin{aligned} C &= \frac{1}{3}\left[\frac{1}{2}\int_0^{\pi} \mathrm{d}\theta \sin(\theta)\sin^2\left(\frac{3f\omega_D}{2}\sin(2\theta)\tau_{\mathrm{DET}}\right)\right] \\ &= \frac{1}{6}\left[1+\sum_{n=0}^{\infty}\frac{J_{2n}(Z)}{16n^2-1}\right] \end{aligned} \tag{7.19}$$

where $Z = 3f\omega_D\tau_{\mathrm{DET}}$, and J_{2n} are spherical bessel functions. The signal intensity is a maximum when $Z \approx 3.8$ with $C \approx 0.24$, and $C \to 1/6$ as $Z \to \infty$.

7.3.1 Implementation and Simulation of HOMIE

In order to generate the different θ-dependencies in the Hamiltonians of Eq. (7.8), Eq. (7.10), and Eq. (7.14), the sample must be mechanically rotated. Under sample rotation about one axis, the $A_{2,0}$ term in H_D^{HF} [Eq. (7.3)] becomes time-dependent and is given by

$$\begin{aligned} A_{2,0}(t) &= \frac{1}{2}(3\cos^2(\theta_L(t))-1) \\ &= \frac{1}{4}(3\cos(\theta)^2-1)(3\cos(\theta_r)^2-1)+\frac{3}{4}\sin(\theta)^2\sin(\theta_r)^2\sin(2(\omega_r t+\phi)) \\ &\quad +\frac{3}{4}\sin(2\theta)\sin(2\theta_r)\sin((\omega_r t+\phi)) \end{aligned} \tag{7.20}$$

where θ_r is the angle that the axis of rotation makes with respect to the magnetic field, ω_r is the frequency of sample rotation, and θ and ϕ are the polar angles that the internuclear

vector makes with respect to the axis of rotation. Since for a pair of spin 1/2 nuclei $[T_{2,0}, T_{2,2}] = [T_{2,0}, T_{2,-2}] = 0$, the addition of a $T_{2,0}$ term into either one of the Hamiltonians, H^{EVO} or H^{DET} from the previous section, will not affect the results given in Eq. (7.17).

H^{EVO} can be created by a variety of rotor-synchronized RF pulses, each resulting in a different factor, g. This factor, g, will ultimately limit the achievable scaling factor, σ, in Eq. (7.18). A maximal scaling can be achieved by applying N phase-incremented, rotor-synchronized units, with the kth unit given by $[(\pi/2)_0 - \tau_d - (\pi/2)_\pi]_{\phi_k}$, where $\tau_d = 1/(\omega_r \mathrm{N})$ and $\phi_k = 2\pi/\mathrm{N}$. Here the pulses are assumed to be δ-pulses. Repeating the sequence with an additional π phase shift removes additional terms arising from the CSA and the dipolar interaction to lowest order (e.g., $I_\pm$, $I_Z I_\pm$). Spinning the rotor at an angle θ_r and applying the above sequence gives

$$g = \frac{3N}{16\pi} \sin(\frac{2\pi}{N}) \sin(\theta_r)^2 \tag{7.21}$$

To achieve the maximum scaling factor, σ, consider the following experiment (Figure 7.3A): while spinning at $\theta_r = 0°$, the spins evolve under H (Eq. 7.8) for a time t. H can be generated by sandwiching H_D^{HF} between two $(\frac{\pi}{2})_Y$ pulses, with an additional π pulse at t/2 in order to refocus CSA, giving $k = 1$. Then to generate H^{EVO} the above sequence of $\delta-$pulses is applied after the rotor has been mechanically flipped to $\theta_r = 90°$. In the limit $N \to \infty$, $g = \frac{3}{8}$. In order to cancel the θ dependence, the evolution times must satisfy the condition:

$$t = \frac{2}{3} g\tau \tag{7.22}$$

Using $g = \frac{3}{8}$ gives $\tau = 4t$, and gives a dipolar scaling factor, σ, of:

$$\sigma\omega_D = \frac{\omega_D}{t+\tau}(\frac{3}{4}t(3\cos(\theta)^2 - 1) + \frac{3}{2}g\tau\sin(\theta)^2) = \frac{3\omega_D}{10} \tag{7.23}$$

This methodology does not require repeated switching back and forth between the two rotor angles since it is not the Hamiltonians but the frequencies which are combined in order to get isotropic dipolar spectra. The spectrum contains two peaks with splitting of $\omega = \pm 0.3\omega_D$, which is the predicted maximum splitting obtained by reconstructing the zero-field Hamiltonian, H_D^{ZF}, from the truncated dipole Hamiltonian [93]. Since the limit $N \to \infty$ is not realistic, a finite N must be chosen. For $N = 8$, the maximum scaling for H^{EVO} is $g = 0.337$, giving $\tau = 4.44t$ and $\sigma = 0.28$. In the absence of CSA, the resulting spectrum is shown in Fig. 7.3B. However, in the presence of CSA, the sequence does not perform nearly as well (Figure 7.3C). Better methods are therefore required in order to compensate for CSA and offsets effects during the sequence. The post-$\mathrm{CN}_{\mathrm{n}}^{\nu}$ sequences[98], which are offset and RF-inhomogeneity compensated variants of the $\mathrm{CN}_{\mathrm{n}}^{\nu}$ sequences[55], contain continuous irradiation, rotor-synchronized pulses. The post-$\mathrm{CN}_{\mathrm{n}}^{\nu}$ consists of N, phase-incremented blocks over a period of n rotor cycles, where the kth block is given by $[(\pi/2)_0(2\pi)_\pi(3\pi/2)_0]_{\phi_k}$, where $\phi_k = 2\pi\nu/\mathrm{N}$. The pulse sequence post-CN_2^0 can be used to generate H[Eq. (7.8)]. This gives a scaling factor k of

$$\begin{aligned} k &= -\frac{1}{2}\left(\frac{3\cos^2(\theta_r) - 1}{2}\right) \\ &= \bar{k}\left(\frac{3\cos^2(\theta_r) - 1}{2}\right) \end{aligned} \tag{7.24}$$

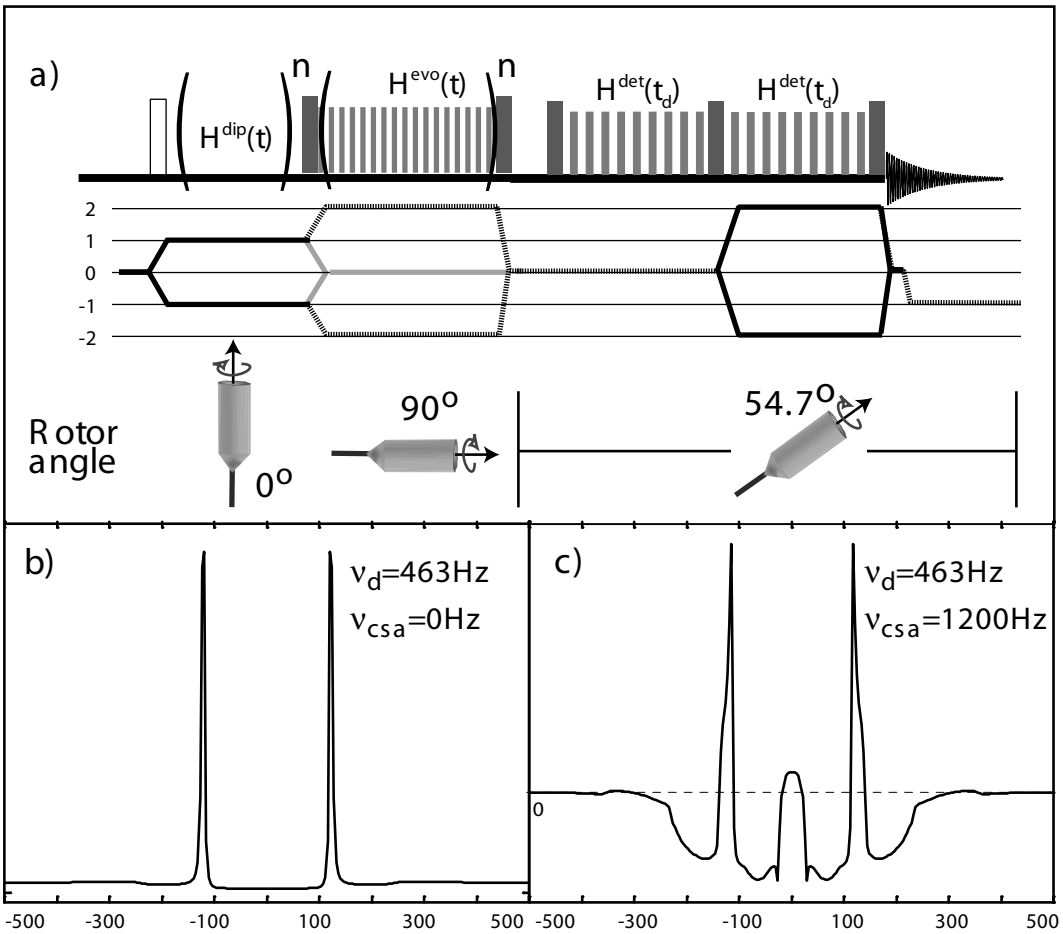

Figure 7.3: (A) An ideal sequence that gives the maximum scaling factor, $\sigma = 0.3$. The spins evolve under H for a time t, with $k = 1$ in Eq. (7.8) while spinning the rotor at $\theta_r = 0°$. Next the rotor is flipped to $\theta_r = 90°$, and the spins evolve under H^{EVO} for a time τ which, as discussed in the text, can be generated with a maximum g of 3/8. Next the rotor is then flipped to the magic angle, and H^{DET} is then applied. (B) Simulation of the above sequence for a pair of dipole coupled spins with $\omega_D/(2\pi) = 463$ Hz, $\omega_{\mathrm{CSA}}/(2\pi) = 0$ Hz, and $\omega_r/(2\pi) = 5$ kHz. $\tau = 4.44$t was used (as described in the text), giving $\sigma = 0.28$. An RF field strength of 150 kHz was used. (C) Same experiment as in (B) but with $\omega_{\mathrm{CSA}} = 1200$ Hz. Notice the deterioration of the isotropic spectrum.

The pulse sequence post-CN_2^2 can be used to create H^{EVO} since it generates terms like $A_{2,\pm 2}T_{2,\mp 2}$ in the Hamiltonian. However, unwanted terms like $A_{2,\pm 1}T_{2,\mp 1}$ and $A_{2,\pm 1}I_{\mp}$ are also generated. These unwanted terms can be removed by applying another cycle of post-$\mathrm{C}N_2^2$ but with an additional π phase shift. The factor, g, for the $(\text{post-}\mathrm{CN}_2^2)_0 - (\text{post} - \mathrm{CN}_2^2)_\pi$ becomes

$$\begin{aligned} g &= \frac{3\sin(\frac{4\pi}{\mathrm{N}})N^3\sin(\theta_r)^2}{32\pi(\mathrm{N}^2-1)} \\ &= \bar{g}\sin^2(\theta_r) \end{aligned} \tag{7.25}$$

Finally, the detection Hamiltonian, $H_{\pm 1}^{\mathrm{DET}}$, can be created by using the post-$\mathrm{C7}_2^{\pm 1}$ sequence [98], with the only requirement being that the sample is not spinning at either $\theta_r = 0°$ or $\theta_r = 90°$, due to the fact that the scaling factor, f, from Eq. (7.14) is zero under these conditions. Evolution under H^{DET} only affects the intensities of the resulting signal [Eq. (7.17)], but not σ.

The requirement of spinning the sample at different angles during the course of the experiment, while leading to a larger σ, can be experimentally demanding. However, the above methodology can also be applied to samples spinning about only one rotor axis. Under this condition, the evolution must satisfy

$$\begin{aligned} &\left|\frac{\omega_D}{t+\tau}\left(\frac{3}{2}\bar{k}t\frac{(3\cos^2(\theta_r)-1)}{2}\frac{(3\cos^2(\theta)-1)}{2} \pm \frac{3}{2}\bar{g}\tau\sin^2(\theta_r)\sin^2(\theta)\right)\right| \\ &= \left|\frac{3k\omega_D t}{2(t+\tau)}\right| \end{aligned} \tag{7.26}$$

When $\theta_r \neq 0°$, t and τ must typically be multiples of the rotor period. From Eq. (7.26),

the rotor angle (θ_r) that the sample must be spun at is given by

$$\theta_r = \arccos\left(\sqrt{\frac{3\bar{k}t \pm 4\bar{g}\tau}{9\bar{k}t \pm 4\bar{g}\tau}}\right) \tag{7.27}$$

7.3.2 Experimental Demonstration of HOMIE

Experiments were performed on a Chemagnetics (now Varian, Palo Alto, CA) spectrometer with a 4.2 T magnet (180 MHz ^{1}H). The sample used was $^{13}C_2$-methyl dimethyl malonic acid (DMMA) diluted to 30 % in natural abundance dimethyl malonic acid and was provided by Herbert Zimmermann. The sample was spun at 5 kHz in a 4mm HX Chemagnetics probe. The spinning angle was set manually. Following a ramped cross polarization period, proton decoupling of 150 kHz was used during the indirect evolution as well as in the directly detected dimension. Eighty t_1 points were collected in the indirect dimension with a dwell of 1.2 ms. The experiment in Figure 7.4 was performed in order to obtain an isotropic dipolar spectrum. H was created by applying the sequence post-$C7_2^0$, with a corresponding scaling factor of $\bar{k} = -1/2$ [Eq. (7.24)]. H^{EVO} was created using a $(\text{post-}C7_2^2)_0 - (\text{post} - C7_2^2)_\pi$ sequence, with a corresponding scaling factor of $\bar{g} = 0.208$[Eq. (7.25)]. Sixteen cycles of $H_\pm^{\mathrm{DET}}$ were used, allowing theoretically $C = 0.23$ amount of the total magnetization to be converted into signal [Eq. (7.48)]. Experimentally, $\approx 16\%$ of the magnetization was converted into signal. With the condition $\tau = 2t$, Eq. (7.27) gives a rotor axis of $\theta_r = 64.7°$, and Eq. (7.26) gives a scaling factor of $\sigma = -0.0566$. Figure 7.5 shows the experimental and simulated spectra. The spectrum consists of two peaks at $\pm(26.3 \pm 3.3)$ Hz. Using the scaling factor $\sigma = -0.0566$ results in an estimated distance between the two ^{13}C nuclei of 2.54 ± 0.16 $\mathring{A}$, which is in good agreement with the previously reported

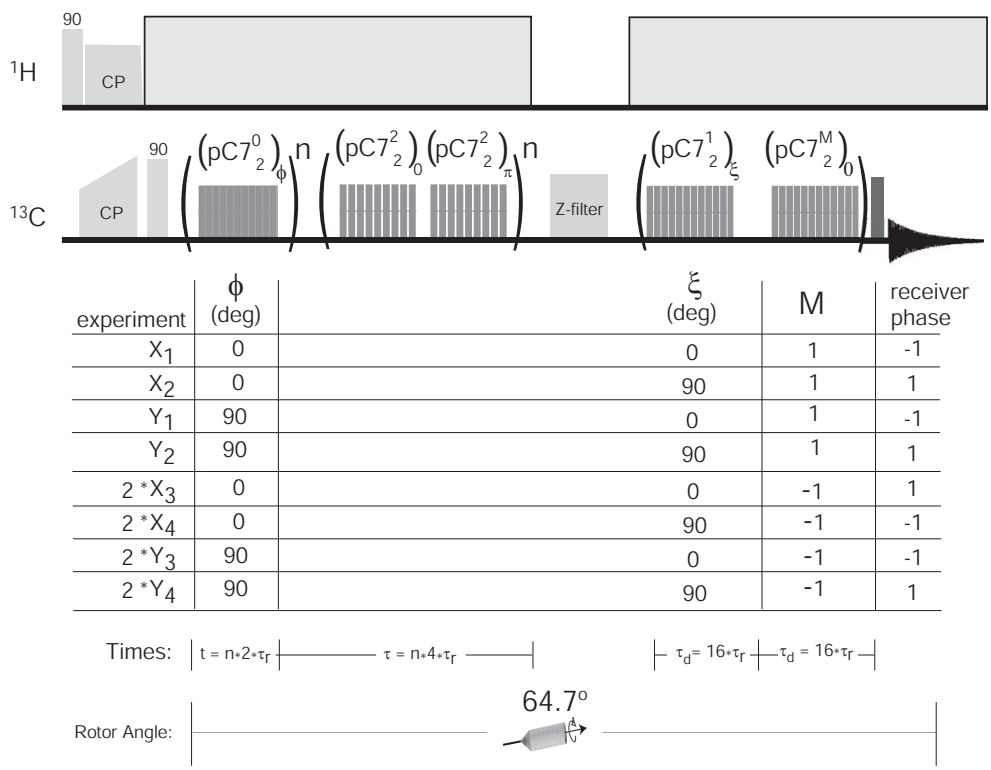

experiment	ϕ (deg)	ξ (deg)	M	receiver phase
X_1	0	0	1	-1
X_2	0	90	1	1
Y_1	90	0	1	-1
Y_2	90	90	1	1
$2*X_3$	0	0	-1	1
$2*X_4$	0	90	-1	-1
$2*Y_3$	90	0	-1	-1
$2*Y_4$	90	90	-1	1

Figure 7.4: Actual experiments performed in order to obtain isotropic dipolar spectra. The pulse sequence along with the corresponding phase cycle is presented. The first four experiments correspond to evolution from ρ_0 in Figure 7.2. The last four experiments correspond to evolution from ρ_2 in Figure 7.2. The last four experiments have to be performed twice as required from Eq. (7.17).

distance[99] of 2.541 $\AA$. Angle missettings, pulse imperfections, and higher-order terms in the average Hamiltonians could all contribute to deviations from the predicted behavior. Homonuclear isotropic evolution works by refocusing the anisotropic contributions of the dipolar interaction by generating a series of various Hamiltonians whose frequencies can be used to cancel the anisotropic terms. Although the experimental scaling of the dipolar couplings was roughly a factor of two lower than the experimentally observed scalings for the previous ZFHF experiments, it was shown that both methods give the same theoretical maximum scaling of $\sigma = 0.3$. Larger scaling factors can be obtained by spinning the sample at multiple angles as discussed earlier. Since the refocusing of the anisotropy comes from combining the frequencies and not the Hamiltonians, the sample does not have to be repeatedly switched between different angles, which is experimentally feasible but still difficult. The ability to switch between multiple spinning angles would be useful in correlating the isotropic dipolar spectra to the magic-angle spinning isotropic chemical shift spectra, which can be done by applying H^{DET} at the magic-angle as shown in Figure 7.3.

There are several limitations that the HOMIE method has that the ZFHF does not. First of all, HOMIE only works for pairs of homonuclear coupled spins, whereas ZFHF constructs the zero-field Hamiltonian for any number of spins. Although it may be possible to extend HOMIE to higher number of spins, HOMIE would only be useful in samples of randomly labelled spin pairs. Secondly, only a fraction of the magnetization, C (Eq. (7.48)) is used in the HOMIE experiment, whereas all the magnetization is potentially used in the ZFHF experiment.

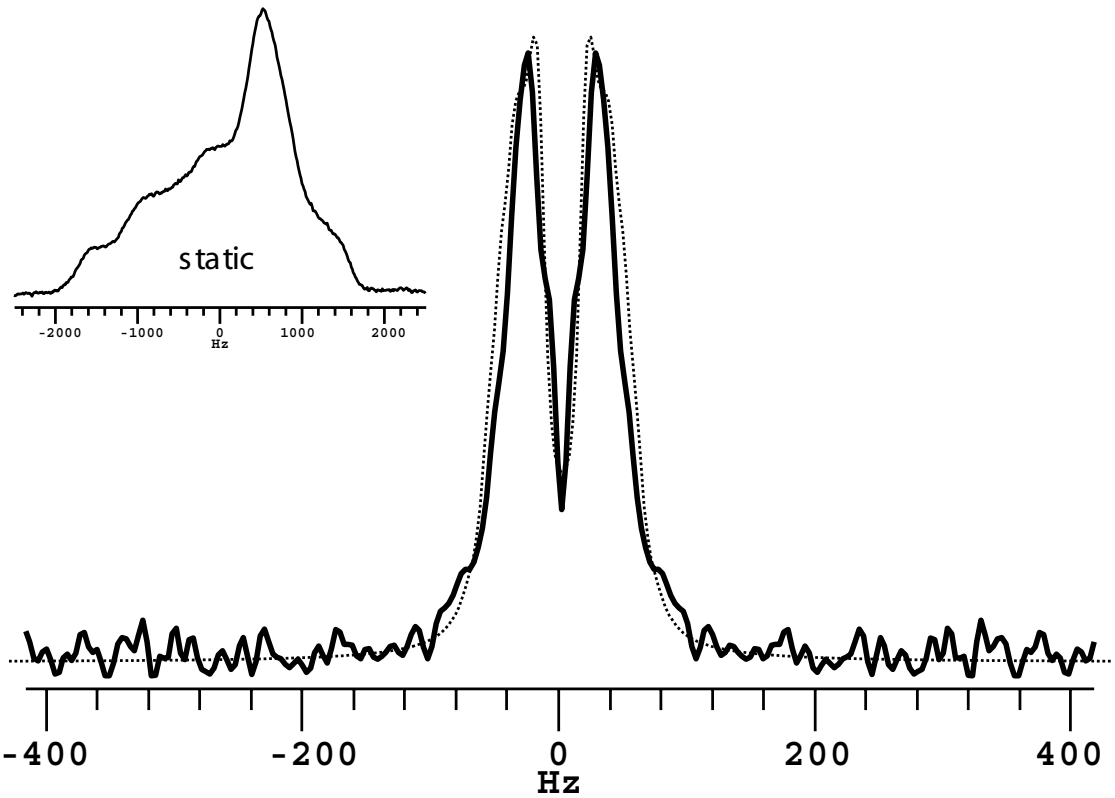

Figure 7.5: Simulation (dashed line) and experimental (solid line) data of the sequence shown in Figure 7.4 on $^{13}C_2$-methyl dimethyl malonic acid (DMMA). Simulation attempted to model DMMA with $\omega_D/2\pi = 463\text{Hz}, \omega_{\text{CSA}}/2\pi = 1200\text{Hz}$, while spinning at 5 KHz. A 10 Hz line broadening was added to the simulation to match the experiment as best as possible. Both the simulated and the experimental spectra give a good match to the scaling factor of $\sigma = 0.0566$. The small spectrum in the left hand corner is the static experimental spectrum of DMMA.

7.4 Isotropic PDLF Spectroscopy (HETIE)

One of the limitations of the HOMIE methodology is that it appears to be only applicable for a pair of homonuclear dipole coupled spins, although extensions of the methodology to larger number of spins may be possible. In contrast, Tycko's zero-field in high-field is applicable to any number of spins, since the zero-field Hamiltonian is generated. Although Tycko's methodology has just been demonstrated for homonuclear systems, it is possible to extend the method to create the isotropic heteronuclear zero-field Hamiltonian. To see this consider the following. The heteronuclear dipole interaction between an I and S spin is given by

$$H^{\mathrm{HF}} = \omega_D A_{2,0}(\theta_L) 2 I_Z S_Z \tag{7.28}$$

where θ_L is the angle that the internuclear vector makes with respect to the Zeeman field. Note that the "flip-flop" terms are not secular in high-field and therefore are effectively not present as shown in the above Hamiltonian. To see that Tycko's methodology can be applied to generate the zero-field Heteronuclear dipolar Hamiltonian, H^{HF} can be rewritten a

$$\begin{aligned} H^{\mathrm{HF}}_{\mathrm{HET}} &= \frac{2}{3}\omega_D A_{2,0}(\theta_L)\left(3 I_Z S_Z - \vec{I}\cdot\vec{S}\right) + \frac{2}{3}\omega_D A_{2,0}(\theta_L)\vec{I}\cdot\vec{S} \\ &= \frac{2}{3}\omega_D A_{2,0}(\theta_L) T_{2,0} + \frac{2}{3}\omega_D A_{2,0} T_{0,0} \\ &= \frac{2}{3}\omega_D \left[\sum_{l=0,2,4} C(l,0,2,0,2,0) F_{l,0} + C(2,0,2,0,0,0) F_{2,0}\right] \end{aligned} \tag{7.29}$$

If a pulse sequence is applied on both the I and S spins that removed the second and fourth rank terms from H^{HF} in the homonuclear case, the heteronuclear zero-field Hamiltonian is obtained with a maximum scaling factor now given by $\sigma_{\mathrm{MAX}} = 2/15$ due to the extra factor of 2/3 in the above Hamiltonian. The homonuclear couplings can in principle be removed without removing the heteronuclear interactions since the I and S spins can be independently manipulated. However, consider the following best case scenario. Look at the case when there are two I spins and one S spin and for the moment assume that the dipole-dipole coupling between the I spins has been removed. The resulting zero-field Hamiltonian is given by

$$H^{\mathrm{ZF}} = \sum_{m=-2}^{2} \left[\omega_D^{1,2} (-1)^m T_{2,m}^{1,2} A_{2,-m}^{1,2} + \omega_D^{1,3} (-1)^m T_{2,m}^{1,3} A_{2,-m}^{1,3} \right] \tag{7.30}$$

where spin 1 is the S spin, and spins 2 and 3 are the I spins. The spectra corresponding to evolution of total magnetization of spins 2 and 3 are shown in Figs. 7.6A and 7.6C for two different sets of dipolar couplings. The spectra contains features that are not simply related to the couplings. This is due to the fact that in general, the zero-field couplings do not commute between spins, i.e., $[H_{1,2}^{\mathrm{ZF}}, H_{1,3}^{\mathrm{ZF}}] \neq 0$. The spectra contain features that are not linear in the number of spins (similar to the second order spectra of Chapter 3), making interpretation of the resulting spectra difficult.

This is in contrast to standard proton-detected local field (PDLF) spectroscopy as shown in Figs. 7.6B and 7.6D. Here the high-field Hamiltonian (Eq. (7.28)) was used instead. In the absence of homonuclear dipolar couplings, the resulting spectra are linear in the number of spins, with the splitting of the lines about zero giving the effective

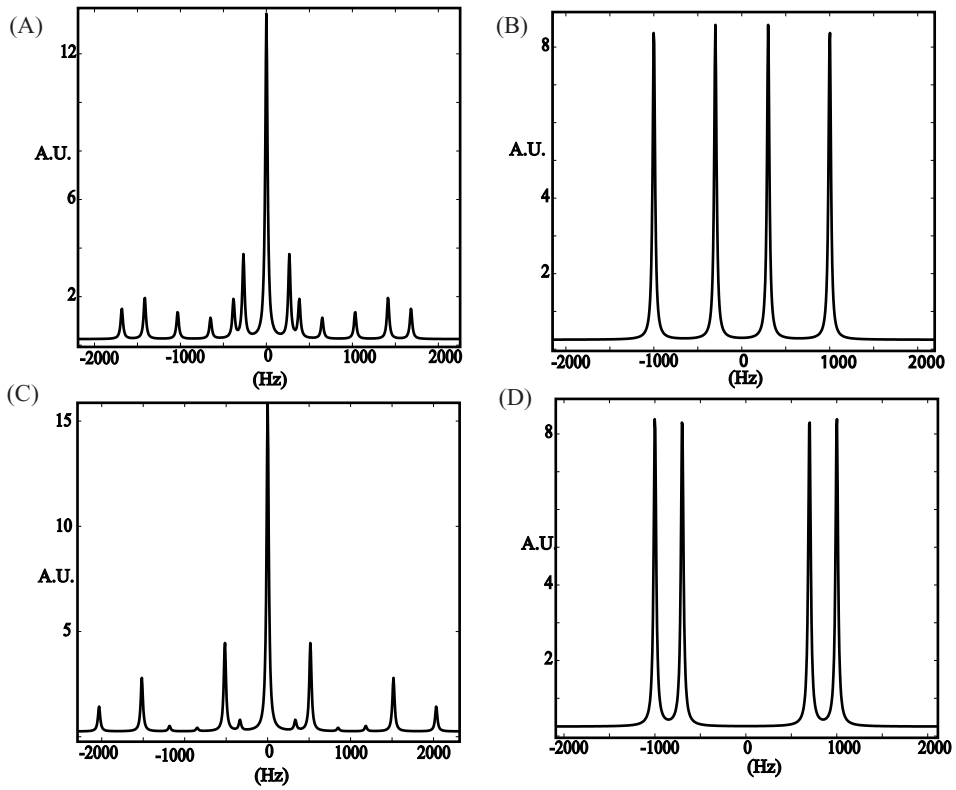

Figure 7.6: Comparison of zero-field proton-detected local field spectroscopy with high-field proton-detected local field spectroscopy for two sets of couplings. In (A) and (B), $\omega_D^{1-3}/(2\pi) = 700$ Hz and $\omega_D^{1-3}/(2\pi) = 300$ Hz in (C) and (D). $\omega_D^{1-2}/(2\pi) = 1000$ Hz in all cases. The zero-field Hamiltonian (Eq. (7.30)) was used in (A) and (C), and the spectra corresponding to evolution of the total magnetization of spins 2 and 3 are shown, with intensity in arbitrary units (A.U.). The high-field Hamiltonian, $H = 2\omega_D^{1-2} I_Z^1 I_Z^2 + 2\omega_D^{1-3} I_Z^1 I_Z^3$, was used to calculate the evolution of transverse magnetization of spins 2 and 3, with intensity shown in arbitrary units.

heteronuclear coupling. In most PDLF experiments, the protons are decoupled from one another and evolve under the heteronuclear coupling to another nucleus, typically a ^{13}C. PDLF experiments typically are implemented in oriented phases as discussed in Chapter 3 where non-zero dipolar couplings exist, but the couplings are motionally averaged to a single value, i.e., there is no powder averaging. This results in N sharp doublets where the spectral information (the motionally averaged heteronuclear dipolar couplings) can be read off quite readily. Applications of PDLF spectra to solids have been performed; however, the resulting spectra are typically broad and difficult to interpret.

So the question remains: is it possible to produce an isotropic heteronuclear dipolar spectra while maintaining the linearity in the number of couplings? The answer is no if the route taken is to produce the zero-field heteronuclear Hamiltonian, due to the fact that the zero-field couplings do not commute. However, a HOMIE-like method could potentially work. In the following, an alternative method, called Heteronuclear Isotropic Evolution, HETIE, will be introduced. Like the HOMIE methodology introduced earlier, HETIE relies on the removal of the anisotropic part of the frequency by evolving under two different Hamiltonians and detecting under a third. First the theory for HETIE is presented along with a direct comparison with HOMIE. Finally, pulse sequences are described which are then used to observe the HETIE technique on an ideal sample.

7.4.1 Theory of heteronuclear isotropic spectra

In the previous section about the theory of HOMIE, the Hamiltonians needed in order to create the HOMIE spectra were either purely double-quantum ($H_{\mathrm{EVO}}, H_{\mathrm{DET}}$) or a combination of double- and zero-quantum operators (H). In addition, the evolution

pathways chosen in the HOMIE experiment were restricted to the two-dimensional subspace $\{|\alpha_1,\alpha_2\rangle, |\beta_1,\beta_2\rangle\}$, whereas evolution from the states $|\alpha_1,\beta_2\rangle, |\beta_1,\alpha_2\rangle$ didn't contribute to the HOMIE signal. To see this, look at the matrix forms of H, H_{EVO}, H_{DET} in the basis $|\alpha_1,\alpha_2\rangle, |\beta_1\beta_2\rangle, |\alpha_1,\beta_2\rangle, |\beta_1,\alpha_2\rangle$

$$\begin{aligned} H &= \omega_D \left(3I_X^1 I_X^2 - \vec{I^1}\cdot\vec{I^2}\right) \\ &= \frac{\omega_D}{4}\begin{pmatrix} -1 & 3 & 0 & 0 \\ 3 & -1 & 0 & 0 \\ 0 & 0 & 1 & 1 \\ 0 & 0 & 1 & 1 \end{pmatrix} \end{aligned} \tag{7.31}$$

$$\begin{aligned} H^{\text{EVO,DET}} &= \omega_D \left(gT_{2,2} + g^* T_{2,-2}\right) \\ &= \omega_D \begin{pmatrix} 0 & g & 0 & 0 \\ g^* & 0 & 0 & 0 \\ 0 & 0 & 0 & 0 \\ 0 & 0 & 0 & 0 \end{pmatrix} \end{aligned} \tag{7.32}$$

These Hamiltonians are block-diagonal, and the evolution pathways used in the HOMIE experiment were only in the $\{|\alpha_1,\alpha_2\rangle, |\beta_1,\beta_2\rangle\}$ subspace. The important point is that the relevant subspace is two-dimensional. Thus when considering a spin 1/2 nucleus, the corresponding Hamiltonians can be easily written by analogy by making the following correspondence: $|\alpha_1,\alpha_2\rangle \to |\alpha\rangle$ and $|\beta_1,\beta_2\rangle \to |\beta\rangle$. The corresponding Hamiltonians are (up

to an overall constant)

$$H = \sum_j k\omega_D^j \frac{3\cos^2(\theta_j) - 1}{2} I_X^j 2S_Z \tag{7.33}$$

$$H^{\mathrm{EVO}} = \sum_j g\omega_D^j \sin^2(\theta_j) \left(\exp(i2\phi_j) I_+^j + \exp(-i2\phi_j) I_-^j\right) 2S_Z \tag{7.34}$$

$$H_{\pm 1}^{\mathrm{DET}} = \sum_j f\omega_D^j \sin(2\theta_j) \left(\exp(\pm i\phi_j) I_+^j + \exp(\mp i\phi_j) I_-^j\right) 2S_Z \tag{7.35}$$

since the heteronuclear couplings between I spins commute (i.e., the homonuclear interactions between I spins have been removed).

So starting with $\rho(0) = \sum_j a_j I_Z^j$, evolution under H for a time t gives

$$\begin{aligned}
\rho(t) &= \exp(-itH)\rho(0)\exp(itH) \\
&= \sum_j a_j \left(I_Z^j \cos\left(k(\theta_j)\omega_D^j t\right) - I_Y^j \sin\left(k(\theta_j)\omega_D^j 2S_Z t\right)\right) \\
&= \sum_j a_j \left(\rho_0^j(t) + \rho_1^j(t)\right) \qquad (7.36) \\
\rho_0^j &= I_Z^j \cos\left(k(\theta_j)\omega_D^j t\right) \qquad (7.37) \\
\rho_1^j &= -I_Y^j \sin\left(k(\theta_j)\omega_D^j 2S_Z t\right) \qquad (7.38)
\end{aligned}$$

where $k(\theta) = (3\cos^2(\theta_j) - 1)/2$. Each of the pathways, ρ_0 and ρ_1, can be distinguished by their rotational property under a Z-rotation as discussed earlier in the HOMIE section. Thus each pathway will be considered separately in the following. Evolution for a time τ

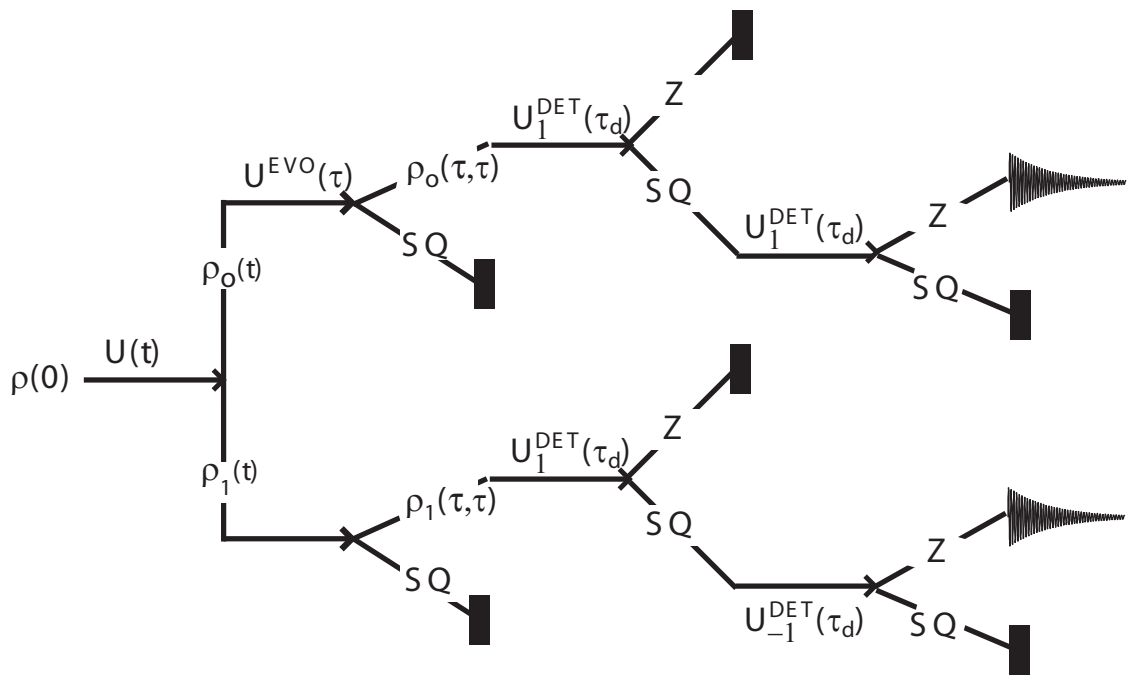

Figure 7.7: The Basic procedure in order to obtain isotropic proton detected local field dipolar spectra. An initial density matrix, $\rho(0) = \sum_j a_j I_Z^j$ evolves under H [Eq. (7.33)] to give a z-magnetization (Z) term, (ρ_0), and single-quantum (SQ) term, (ρ_1). Both of these terms then evolve under H^{EVO} [Eq. (7.34)] and only the Z components are kept. Next, evolution occurs from $\rho_0(t,\tau)$ and $\rho_1(t,\tau)$ under H_1^{DET} [Eq. (7.35)] into SQ coherence. The SQ coherences are then converted back into z-magnetization for detection, using either H_1^{DET} for the pathway originating from ρ_0 or H_{-1}^{DET} for the pathway originating from ρ_1.

under H^{EVO} gives the following:

$$\begin{aligned}
\rho_0(t,\tau) &= \exp\left(-i\tau H^{\mathrm{EVO}}\right)\rho_0(t)\exp\left(i\tau H^{\mathrm{EVO}}\right) \\
&= \sum_j a_j I_Z^j \cos\left(k(\theta_j)\omega_D^j t\right)\cos\left(2g(\theta_j)\omega_D^j\tau\right) \\
&\quad + \frac{i}{2}\exp(-i2\phi_j)\sin\left(2g(\theta_j)\omega_D^j 2S_Z\tau\right)a_j I_+^j \\
&\quad - \frac{i}{2}\exp(i2\phi_j)\sin\left(2g(\theta_j)\omega_D^j 2S_Z\tau\right)a_j I_-^j \qquad (7.39) \\
\rho_1(t,\tau) &= \exp\left(-i\tau H^{\mathrm{EVO}}\right)\rho_1(t)\exp\left(i\tau H^{\mathrm{EVO}}\right) \\
&= -\sum_j a_j I_Y^j \sin\left(k(\theta_j)\omega_D^j 2S_Z t\right)\left[\cos^2\left(2g(\theta_j)\omega_D^j 2S_Z\tau\right)\right. \\
&\quad \left. + \sin^2\left(2g(\theta_j)\omega_D^j 2S_Z\tau\right)\sin(4\phi_j)\right] \\
&\quad + a_j I_X^j \sin\left(k(\theta_j)\omega_D^j 2S_Z t\right)\sin^2\left(2g(\theta_j)\omega_D^j 2S_Z\tau\right)\cos(4\phi_j) \\
&\quad + \sin\left(k(\theta_j)\omega_D^j 2S_Z t\right)\sin\left(2g(\theta_j)\omega_D^j 2S_Z\tau\right)\cos(2\phi_j)a_j I_Z^j \qquad (7.40)
\end{aligned}$$

where $g(\theta_j) = g\sin^2(\theta_j)$, and the identities $\sin(2gS_Z) = 2S_Z\sin(g)$ and $(2S_Z)^2 = 1$ were used. After application of H^{EVO}, the terms proportional to $I_\pm$ are phase-cycled away, leaving only the Z components of the density matrix. As before, the Z-magnetization at the end of H^{EVO} is given by

$$\begin{aligned}
\langle I_Z(t,\tau)\rangle_0 &= \mathrm{Tr}\left(\rho_0(t,\tau)I_Z\right) \\
&= \sum_j a_j \cos\left(k(\theta_j)\omega_D^j t\right)\cos\left(2g(\theta_j)\omega_D^j\tau\right) \qquad (7.41) \\
\langle I_Z(t,\tau)\rangle_1 &= \mathrm{Tr}\left(\rho_1(t,\tau)I_Z\right) \\
&= \sum_j a_j \sin\left(k(\theta_j)\omega_D^j t\right)\sin\left(2g(\theta_j)\omega_D^j\tau\right)\cos(2\phi_j) \qquad (7.42)
\end{aligned}$$

The θ_j dependence in both Eq. (7.41) and Eq. (7.42) could be cancelled if

$$\frac{3}{2}kt = \pm 2g\tau \tag{7.43}$$

Since both of these equations can't be satisfied simultaneously, at most half of the signal can be made isotropic, as in the HOMIE case. Similar to the HOMIE experiment, the anisotropic portion of the signal can be eliminated by removing the ϕ_j in Eq. (7.42), such that the signals could be added or subtracted to give

$$\cos(k(\theta_j)t)\cos(2g(\theta_j)\tau) \pm \sin(k(\theta_j)t)\sin(2g(\theta_j)\tau) = \cos(k\theta_j t \mp 2g(\theta_j)\tau). \tag{7.44}$$

By evolving under $H_{\pm 1}^{\mathrm{DET}}$ given in Eq. (7.35) the ϕ_j is removed. The pathway originating from ρ_0 evolves for a time τ_{DET} under H_1^{DET}. Next a filter is applied that only allows single-quantum coherences through as shown in Figure 7.7. Finally H_{DET} is applied again for a time τ_{DET}, the Z component of magnetization is measured to give the corresponding signal of

$$\begin{aligned} S_0 &= \mathrm{Tr}\left[I_Z \rho_0(t, \tau, \tau_{\mathrm{DET}})\right] \\ &= \sum_j a_j \cos(k(\theta_j)t)\cos(2g(\theta_j)\tau)\sin^2(2f(\theta_j)\tau_{\mathrm{DET}}) \end{aligned} \tag{7.45}$$

The pathway originating from ρ_1 first evolves for a time τ_{DET} under H_1^{DET}. Next a filter is applied that only allows single-quantum coherences through as shown in Figure 7.7. Finally, H_{-1}^{DET} is applied for a time τ_{DET} and the z component of magnetization is measured

to give

$$\begin{aligned} S_1 &= \mathrm{Tr}\left[I_Z \rho_1(t,\tau,\tau_{\mathrm{DET}})\right] \\ &= -\sum_j a_j \sin(k(\theta_j)t)\sin(2g(\theta_j)\tau)\sin^2(2f(\theta_j)\tau_{\mathrm{DET}})\cos^2(2\phi_j) \end{aligned} \tag{7.46}$$

Taking into account the factor of 1/2 from the powder average over ϕ_j, the signals from the two experiments can be combined as

$$S_0 \pm 2S_1 = \sum_j a_j C_j(\tau_{\mathrm{DET}})\left[\cos(k(\theta_j)t \pm 2g(\theta_j)\tau)\right] \tag{7.47}$$

where $a_j C_j$ are the corresponding signal intensities for spin j given by

$$\begin{aligned} a_j C_j &= \frac{1}{3}\left[\frac{1}{2}\int_0^{\pi} \mathrm{d}\theta \sin(\theta_j)\sin^2\left(2f\omega_D^j \sin(2\theta_j)\tau_{\mathrm{DET}}\right)\right] \\ &= \frac{a_j}{6}\left[1+\sum_{n=0}^{\infty}\frac{J_{2n}(Z_j)}{16n^2-1}\right] \end{aligned} \tag{7.48}$$

where $Z_j = 4f\omega_D^j\tau_{\mathrm{DET}}$, and J_{2n} are spherical bessel functions. The signal intensity is a maximum when $Z \approx 3.8$ with $C \approx 0.24a_j$, and $C \to a_j/6$ as $Z \to \infty$.

7.4.2 Implementation and Simulation of HETIE

There exist two additional challenges in implementing the requisite Hamiltonians for the HETIE experiments over that of the HOMIE experiments. First of all, the homonuclear dipole-dipole interactions between the I spins (and the S spins if there are more than one present) must be removed, since the above theory deals only with isolated I spins coupled to an S spin. The second requirement is that the chemical shift anisotropy (CSA) of

the I spins must also be removed. Since the heteronuclear dipolar coupling and the CSA both have second-rank spatial components and are linear in the spin operator I_Z, they can only be separately manipulated by applying pulses on the S spin.

H^{EVO} can be created by a variety of rotor-synchronized RF pulse sequences, each resulting in a different scaling factor , g. For the moment, consider the case where there is only an IS spin pair. A maximal scaling can be achieved for g by applying N, phase-incremented, rotor-synchronized units, with the kth unit given by

$$[(\pi/2)_0 - \tau_d - (\pi/2)_\pi]_{\phi_k} \tag{7.49}$$

where $\tau_d = 2\pi/(\omega_r N)$ and $\phi_k = 4\pi/N$. Here the pulses are assumed to be perfect δ-pulses. Next the sequence is repeated with an extra π phase shifted added and is sandwiched between two 180° pulses on the S spin. This helps to refocus the CSA terms while keeping the heteronuclear couplings to lowest order. Spinning the rotor at an angle $\theta_r = 0$ and applying the above sequence for a time τ gives

$$g = \frac{3N\sin^2(\theta_r)}{32\pi}\sin\left(\frac{2\pi\omega_r\tau_d}{N}\right) \tag{7.50}$$

To achieve the maximum scaling, σ, consider the following hypothetical experiment: the sample first spins along θ_r for a time t while the sequence

$$[(\pi/2)^I_{\pi/2}\left(-t^{"} - (\pi)^I_0(\pi)^S_0 - 2t^{"} - (\pi)^I_\pi(\pi)^S_\pi - t^{"} -\right)^N (\pi/2)^I_{3\pi/2}] \tag{7.51}$$

is performed, where $t = 4Nt^{"}$. This produces the average Hamiltonian, H, with $k = 1$.

Next the rotor axis is flipped down to $\theta_r = 90°$, and H^{EVO} is created using the sequence described using Eq. (7.49) for a time $\tau = 2m\pi/\omega_r$, where m is some integer due to the fact that H^{EVO} must be created over some integer multiple of the rotor period. In the limit that $N \to \infty$, Eq. (7.50) shows that $g \to 3/16$. From Eq. (7.43), the anisotropic component of the heteronuclear dipole interaction can be removed when $\tau = +3t/(4g)$. Using $g = 3/16$ gives $\tau = 4t$ and gives a dipolar scaling factor, σ, of

$$\sigma\omega_D = \frac{\omega_D}{t+\tau}\left(\frac{t}{2}(3\cos^2(\theta) - 1) + 2g\tau\sin^2(\theta)\right) = \frac{\omega_D}{5} \tag{7.52}$$

which is the theoretical maximum scaling factor for creating the zero-field Hamiltonian for a heteronuclear spin pair.

The above result is purely hypothetical since the limit $N \to \infty$ is not realistic. In addition, for a system of I spins coupled to an S spin, the obtainable scaling factor is reduced due to any homonuclear decoupling method used since some of the experiment has to be performed away from the magic angle. It can be imagined that an extremely large RF is used to decouple the I spins from each other on a faster time scale than that used to create H, H^{EVO}, and H^{DET}. In this scenario, the scaling factor would be reduced by at least a factor of $1/\sqrt{3}$, since that is the largest scaling factor any pure multipulse homonuclear decoupling sequence can have.

A more realistic set of pulse sequences that can be used to create H,H^{EVO}, and $H^{\mathrm{DET}}_{\pm 1}$ while removing both the CSA and homonuclear dipolar interactions are shown in Figure 7.8.

Each of these pulse sequences are composed of small blocks which can be repre-

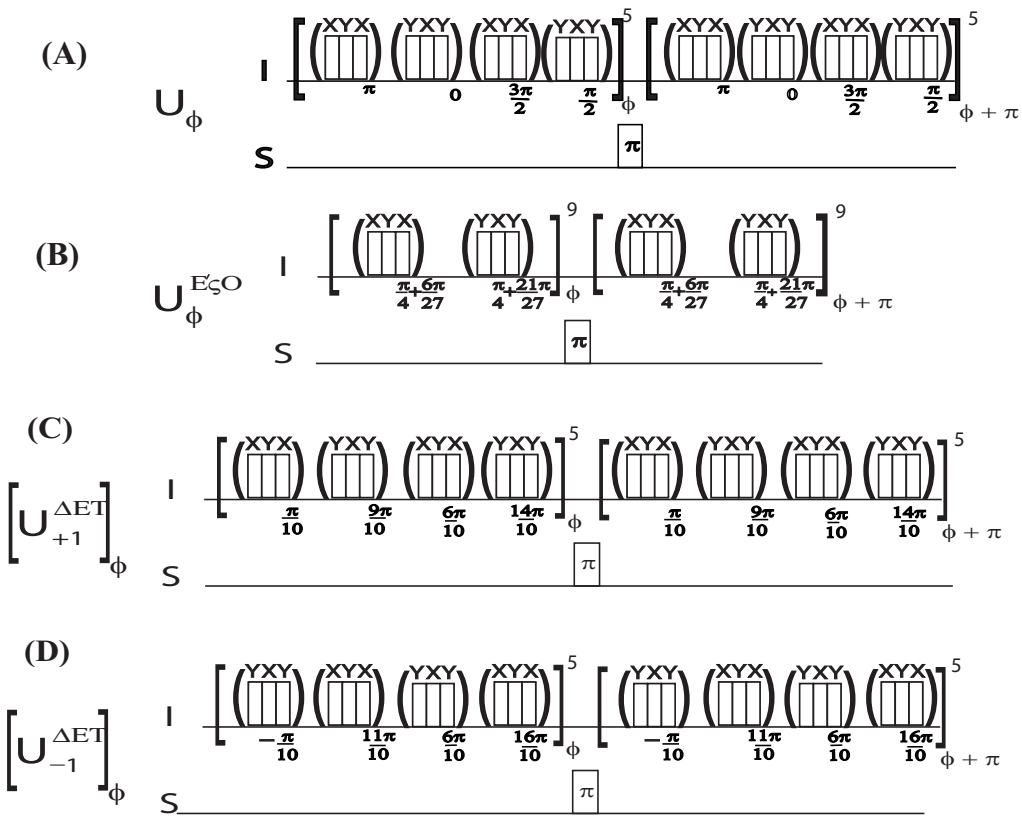

Figure 7.8: Basic pulse sequences used to create $H, H^{\mathrm{EVO}}, H_{\pm}^{\mathrm{DET}}$ needed for HETIE. (A)The pulse sequence which creates H (Eq. (7.33)) to lowest order and the corresponding propagator U(t). $\omega_{RF} = (15/2)\omega_r$, and the total time step for propagator U(t) is $t = 8\pi/\omega_r$. (B) The pulse sequence which creates H^{EVO} to lowest order and the corresponding propagator, $U^{\mathrm{EVO}}(\tau)$. $\omega_{RF} = (27/4)\omega_r$ and the total time step for the propagator $U^{\mathrm{EVO}}(\tau)$ is $\tau = 8\pi/\omega_r$. (C) and (D) are the pulse sequences and corresponding propagators for H_{+}^{DET} and H_{-}^{DET} respectively. $\omega_{RF} = (15/2)\omega_r$ and the time step for the propagators $U_{\pm}^{\mathrm{DET}}(\tau_{\mathrm{DET}})$ is $\tau_{\mathrm{DET}} = 8\pi/\omega_r$

sented by the sequence

$$[(\pi/2)_X - (\pi/2)_Y - (\pi/2)_X]_\phi \, [(\pi/2)_Y - (\pi/2)_X - (\pi/2)_Y]_{\phi_1} \tag{7.53}$$

$$\begin{aligned} U(t) &= \exp\left(-2i[\phi_1 - \phi]\right) \exp(-it_{cyc}\overline{H}) \\ \overline{H} &= \sum_{n=0}^{\infty} \overline{H}^{(n)} \end{aligned} \tag{7.54}$$

where t_{cyc} is the total time of the block of pulses $(3\pi/(\omega_{RF})$, and $\overline{H}$ is the average Hamiltonian theory over the time t_{cyc}, where $\overline{H}^n$ is the nth order average Hamiltonian. The zeroth order average Hamiltonian is given by

$$\overline{H}^{(0)} = \sum_{k=-2}^{2} \sum_{p=-2}^{2} \sum_{l=0,1,2} \bar{b}^{(0)}_{k,p,l} A_{2,k} C_{l,p} \tag{7.55}$$

where $A_{2,k}$ are spatial tensors and $C^{l,p}$ are spin tensors, l is the rank of the spin tensor in the I space (i.e., both I_Z and $I_Z S_Z$ are first rank terms, whereas $3I_Z^i 3I_Z^j - \vec{I}^i \cdot \vec{I}^j$ are second rank terms). The coefficients, $b^{(0)}_{k,p,l}$ can be determined by average Hamiltonian theory. The coefficients, $b^{(0)}_{k,\pm1,1}$, for terms like I_+^j and $I_\pm^j S_Z$ are given by

$$\begin{aligned} b^{(0)}_{k,\pm1,1} &= -d^2_{k,0}(\theta_r) v^{\frac{3}{2}} \exp(\mp i\phi) \exp\left(\pm i\frac{\pi}{4}\right) \left(\exp(\mp i[\phi - \phi_1]) v^3 - 1\right) \\ & X \quad \cos\left(\frac{\pi}{4} \mp \frac{\pi k Z}{4}\right) \cos\left(\frac{\pi k Z}{2}\right) \frac{2}{3\pi[(kZ)^2 - 1]} \end{aligned} \tag{7.56}$$

where $Z = \omega_r/\omega_{RF}$, and $v = \exp[i(kZ\pi)/2]$. The coefficients, $b^{(0)}_{k,\pm1,2}$, for terms like $I_Z^i I_\pm^j +$

$I^i_\pm I^j_Z$ are given by

$$\begin{aligned} b^{(0)}_{k,\pm1,2} &= 2d^2_{k,0}(\theta_r)\exp(\mp i\phi)v^{\frac{3}{2}}\exp\left(\mp i\frac{\pi}{4}\right)\frac{\cos\left(\frac{\pi}{4}\pm\frac{\pi kZ}{4}\right)}{} \\ &\quad \pi\left[4-(kZ)^2\right]\left[v^3\exp(\mp i[\phi-\phi_1])+1\right] \end{aligned} \tag{7.57}$$

Note that when $v^3\exp(\pm i[\phi-\phi_1])=1$, $b^{(0)}_{k,\pm1,1}=0$ while $b^{(0)}_{k,\pm1,2}\neq 0$, and when $v^3\exp(\pm i[\phi-\phi_1])=-1$, $b^{(0)}_{k,\pm1,1}\neq 0$ while $b^{(0)}_{k,\pm1,2}=0$. This is due to the units $[(\pi/2)_X(\pi/2)_Y(\pi/2)_X]$ and $[(\pi/2)_Y(\pi/2)_X(\pi/2)_Y]$ acting like composite 180° pulse (with an additional Z rotation). Under a 180° pulse, $I_\pm\rightarrow -I_\mp$, while $I^i_Z I^j_\pm + I^i_\pm I^j_Z \rightarrow I^i_Z I^j_\mp + I^i_\mp I^j_Z$, hence the ability of these sequences to distinguish between odd and even ranked spin tensors. Note also that $b^{(0)}_{0,0,1}=b^{(0)}_{0,0,2}=0$, so that these sequences are compensated for offset and the static portion of the homonuclear dipolar interaction.

The extra Z rotation of phase $-2[\phi_1-\phi]$ in Eq. (7.54) propagates through by repeatedly applying the basic unit, which results in each subsequent $\overline{H}$ to be phase shifted by $\Delta=-2[\phi_1-\phi]$ from the previous Hamiltonian, analogous to the CN^n_ν sequences described earlier in the HOMIE experiments. The propagator over N applications of the basic unit is given by

$$\begin{aligned} U^N &= T\prod_{k=1}^{N}\exp\left(P_Z(\Delta\exp\left(-i\tau_{cyc}\overline{H}_k\right)\right) \\ &= P_Z\left(\Delta N\right)T\prod_{k=1}^{N}\exp\left[-i\tau_{cyc}P_Z\left(-\Delta(N-1)\right)\overline{H}_k P_Z\left(\Delta(N-1)\right)\right] \end{aligned} \tag{7.58}$$

where For $\Delta = 2\pi\nu/N$, only those terms of the form $A_{2,m}C_{l,p}$ with m and p satisfying

$$nm - p\nu = NZ \tag{7.59}$$

where Z is an integer, will be present to lowest order. Notice that this is the exact same selection rule given for the CN_ν^n sequences, which should not be surprising, since Eq. (7.58) looks identical to a pulse sequence where an average Hamiltonian, $\overline{H}$, is created N times but with the kth Hamiltonian phase shifted by $\Delta(k-1)$ with respect to the first Hamiltonian.

Although there exist numerous ways to produce H, one simple way is application of the sequence as shown in Figure 7.8A. This sequence represents a hybrid of the RN_n^ν sequences with a CN_n^ν sequence. Formally, this sequence is equivalent to a $C5_2^0$ sequence, which selects for terms, $A_{2,m}T_{l,p}$ with $p = \{0, \pm1, \pm2\}$ and $m = 0$ as given in Eq. (7.59). In addition, the composite 180° pulses remove any $A_{2,0}T_{2,0}$ and terms such as chemical shift, CSA, and heteronuclear coupling as discussed earlier. Finally, fact that the C unit is made up of a combination of composite 180° helps to remove the $A_{2,0}T_{2,\pm1}$ terms to lowest order (Eq. (7.56) and Eq. (7.57)). The two composite 180° pulses are repeated with an additional phase shift of $\pi/2$ to remove the $A_{2,0}T_{2,\pm2}$ terms. A 180° pulse is applied to the S spin, and the sequence is repeated again with an additional π phase shift in order to refocus any recoupled CSA and shift terms. The zeroth-order average Hamiltonian is given by

$$\begin{aligned} H &= k\sum_j \frac{3\cos^2(\theta_j)-1}{2} 2\omega_D^j I_X^j S_Z \\ k &= \frac{4}{3\pi}\frac{3\cos^2(\theta_r)-1}{2} \\ &= \bar{k}\frac{3\cos^2(\theta)-1}{2} \end{aligned} \tag{7.60}$$

The total time for one cycle of H is $8\pi/\omega_r$.

H^{EVO} can be created by numerous methods, and one such method is shown in Figure 7.8B, which corresponds to two $R18_2^5$ phase shifted by π with respect to one another with a 180° pulse on the S spin in between the two cycles. This gives a zeroth-order average Hamiltonian of

$$\begin{aligned} H^{\mathrm{EVO}} &= g\sum_j \sin^2(\theta_j)2\omega_D^j S_Z\left(I_+^j\exp(i2\phi_j)+I_-^j\exp(-i2\phi_j)\right) \\ g &= \sin^2(\theta_r)\cos\left(\frac{\pi}{4}-\frac{\pi\omega_r}{2\omega_{RF}}\right)\cos\left(\frac{\pi\omega_r}{\omega_{RF}}\right)\frac{\sin^2(\theta_r)}{2\left[4\left(\frac{\omega_r}{\omega_{RF}}\right)^2-1\right]} \\ &= \bar{g}\sin^2(\theta_r) \end{aligned} \tag{7.61}$$

Finally, the detection Hamiltonian, $H_\pm^{\mathrm{DET}}$, can be created using the sequence shown in Figures 7.8C and 7.8D, which formally correspond to the sequence $C5_2^{\mp 4}$ and produce the average Hamiltonian

$$H_\pm^{\mathrm{DET}} = f\sum_j \sin(2\theta_j)2\omega_D^j S_Z\left(I_+^j\exp(\pm i\phi_j)+I_-^j\exp(\mp i\phi_j)\right) \tag{7.62}$$

$$\begin{aligned} f &= \frac{\cos\left(\frac{\pi}{4}\right)\sin(2\theta_r)\cos\left(\frac{\pi}{4}-\frac{\pi\omega_r}{4\omega_{RF}}\right)\cos\left(\frac{\pi\omega_r}{2\omega_{RF}}\right)}{\pi\left[\left(\frac{\omega_r}{\omega_{RF}}\right)^2-1\right]} \\ &= \bar{f}\sin(2\theta_r) \end{aligned} \tag{7.63}$$

Note that to create H_-^{DET} with the same $\bar{f}$ dependence required using switching the order of the composite 180° pulses ind Figure 7.8D.

To simplify the experiment, a solution can be found for a single rotor axis. Under

this condition, the evolution must satisfy

$$\left|\frac{\omega_D}{t+\tau}\left(\bar{k}rt\frac{(3\cos^2(\theta_r)-1)}{2}\frac{(3\cos^2(\theta)-1)}{2}\pm 2\bar{g}\tau\sin^2(\theta_r)\sin^2(\theta)\right)\right|$$

$$= \left|\frac{k\omega_D t}{(t+\tau)}\right| \tag{7.64}$$

When $\theta_r \neq 0°$, t and τ must both be a multiple of the rotor period. In addition, H^{DET} must be able to be created at the given rotor axis, which means solutions near 90° and 0° must be discarded. From Eq. (7.64), the rotor angle (θ_r) that the sample must be spun at is given by

$$\theta_r = \arccos\left(\sqrt{\frac{3\bar{k}t\pm 8\bar{g}\tau}{9\bar{k}t\pm 8\bar{g}\tau}}\right) \tag{7.65}$$

7.4.3 Experimental Demonstration of HETIE

The experimental implementation of the HETIE was tested on a natural abundance sample of ferrocene ($Fe(C_5H_5)_2$) which was doped with 2% by weight cobaltocene ($Co(C_5H_5)_2$) to aid in shortening the T_1 relaxation time of the ferrocene protons to 1 s from what is normally ˜60 s. The sample was prepared by melting the two components together and was ground to a powder and packed into a 4 mm MAS rotor. The experiment was performed at a ^{1}H resonance frequency of 300.986 MHz exactly on resonance for the protons of the ferrocene. The angle was set externally to 73.9° ± 0.2° with the use of a protractor and a long rod which was exactly coaxial with the spinning axis. A ^{1}H spectrum obtained under the conditions of the HETIE experiment is shown in Figure 7.9. The ^{1}H

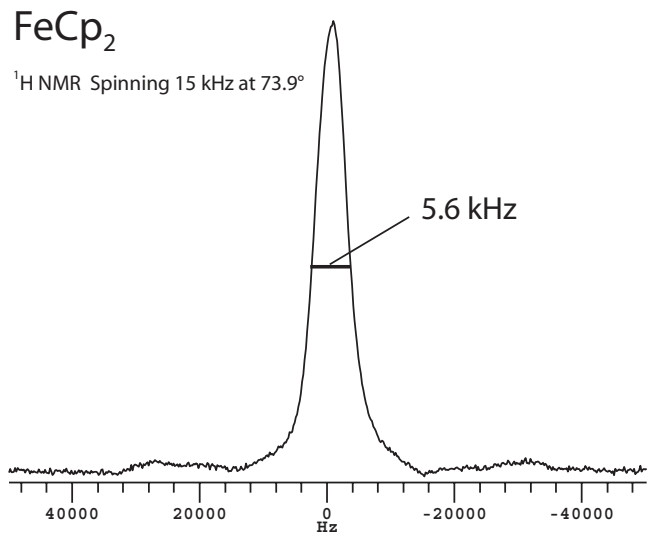

Figure 7.9: 300.986 MHz ^{1}H NMR spectrum of $FeCp_2$ spinning 15 kHz at 73.9°

linewidth is 5.6 kHz and is clearly not isotropic due to the ^{1}H-^{1}H dipolar couplings and ^{1}H CSA which are only scaled when spinning 15 kHz at 73.9°.

The spectrometer used in these experiments was an Infinity-plus spectrometer (Varian Inc., Palo Alto, CA). A Chemagnetics (now Varian Inc., Palo Alto, CA) 4mm Apex-HX MAS probe was used. The RF amplitudes for the sequence were calibrated by finding the maximum intensity of the required $\frac{\pi}{2}$-pulse on proton. The π-pulse on ^{13}C was calibrated using a CP (cross-polarization) and observing where the cross-polarized signal's phase was inverted after the application of a fixed π-pulse. The pulse sequence was rotor synchronized by controlling the spinning speed at 15 kHz $\pm$3 Hz.

One of the difficulties with implementing the HETIE sequence was keeping the requirements of RF and rotor synchronization within experimental reality. The specific experimental limitations that had to be dealt with were the fact that the probe could only spin the sample up to 20 kHz and the maximum achievable RF powers were ν_1= 150 kHz.

While the maximum spinning speed is practically a ceiling, the RF power is more flexible. Although the RF power of 150 kHz could be utilized, the RF pulse quality diminishes with an increasing RF power. For this reason, often time better performance is achieved at lower RF powers such as $\sim$ 100 kHz which was the RF used in the HETIE experiments below. This is due to a fixed pulse rise and fall time of about 300 ns regardless of the RF power. Thus, when the $\frac{\pi}{2}$-pulse is 1.67 μs (as it is in 150 kHz RF) a significant fraction of the applied pulse has an ill-defined phase and amplitude. Although the experiment as written attempts to compensate rise time effects by keeping the pulse in an always-on state, however the phase shifts (although quoted as changing in 50 ns) in actuality occur in over 100 ns. Given these limitations, special pulse sequence design considerations must be addressed when implementing a windowless (RF always on) multiple-pulse sequence such as is presented here (for the pulse sequences see Appendix A.3).

7.4.4 Results

The analytical determination of the scaling factor for the HETIE sequence as implemented and according to Figure 7.10 would yields a scaling factor of σ=0.0817. Unfortunately, although ferrocene is an ideal sample due to the scaled dipolar couplings and symmetry, there exists more than 30 different structures in the Cambridge Structure Database with C-H bond lengths varying in the range of 0.99 to 1.1 Å. We have restricted our analysis of the bond lengths to more modern neutron diffraction studies where the diffraction method has a better chance of detecting the proton positions. In an attempt to predict the expected values for the observed scaled couplings we selected the bond lengths from the neutron structure with the best experimental parameters[100]. In the study we chose, they

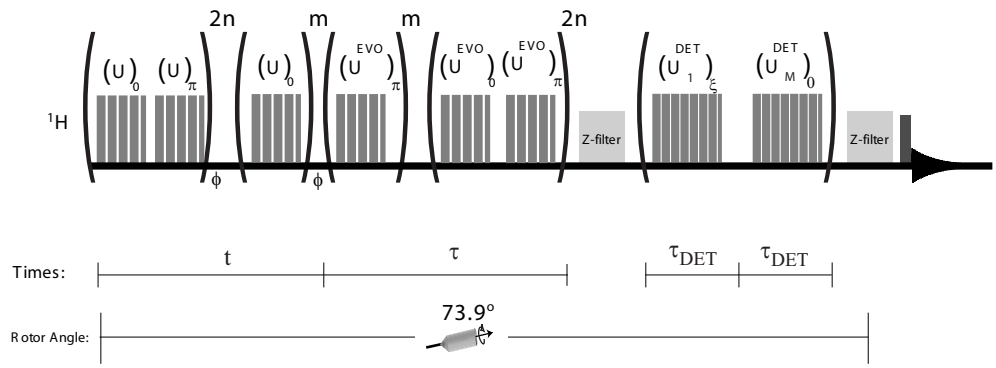

experiment	ϕ (deg)	ξ (deg)	M	receiver phase
X_1	0	0	1	-1
X_2	0	180	1	1
Y_1	180	0	1	-1
Y_2	180	180	1	1
$2*X_3$	0	0	-1	1
$2*X_4$	0	180	-1	-1
$2*Y_3$	180	0	-1	-1
$2*Y_4$	180	180	-1	1

Figure 7.10: Actual experiments performed for demonstration of HETIE methodology to obtain isotropic proton detected local-field spectra. The pulse sequence along with the corresponding phase cycle is presented. Definitions of U, U^{EVO}, and $U_{\pm}^{\mathrm{DET}}$ are given in Figure 7.8, which include the series of 180° pulses which are not explicitly shown in this figure. The points in t_1 are parameterized by $2n+m$, $n = \{0, 1, 2, ...\}$ and $m = 1$ for odd numbered points and $m = 0$ for even numbered points. For the above experiment, $t = \tau = (2n+m) * 16\pi/\omega_r$. The first four experiments correspond to evolution along ρ_0 in Figure 7.7. The last four experiments correspond to evolution along ρ_1 in Figure 7.7. The last four experiments have to be performed twice as required from Eq. (7.17).

attempted to treat the complex Cp motions in their diffraction analysis. Their analysis gave a variable interpretation of the carbon-proton internuclear distances (standard deviation = 0.02 Å) for room temperature samples of ferrocene. We used their structure found in the Cambridge Structure Database (CSD ref. # FEROCE29) which reports C-H distances of 1.04, 2.18, and 3.28 Å. In addition to the work by Brock et al., there has been much discussion on the proper interpretation of the ferrocene diffraction data and we hope that NMR might be able to provide some additional insight[101].

The only C-H couplings necessary to consider are the intra-ring nuclei since the fast motion of the Cp ring effectively decouples each ring from every other including within the $FeCp_2$ molecule. This ring motion also effects the observable couplings since the motional timescale is much greater than that of the couplings; this scales the couplings by a factor $P_2(\cos\theta)$ where θ is the angle between the C-H vector and the axis of fast motion, i.e. 90° and thus scales by $\frac{1}{2}$.

Given the C-H distance uncertainties, it is important to consider the error when comparing expected dipolar coupling results. Using the distances above and the associated standard deviation from the different analyses of the same diffraction data, we expect the unique observed dipolar couplings of room temperature ferrocene between a single ^{13}C on the ring and the protons as scaled by the HETIE experiment to be 1026 ±232, 111.5 ±12, 33 ±2.4 Hz. The error in these scaled couplings may seem quite large, however, the $\frac{1}{r^3}$ dependence of the coupling amplifies errors at small distances.

These scaled coupling values are determined from the ideal scaling factor from above which lacks any inclusion of interactions which might degrade the performance of the sequence. To address this, we have performed simulations of a three spin system both as an

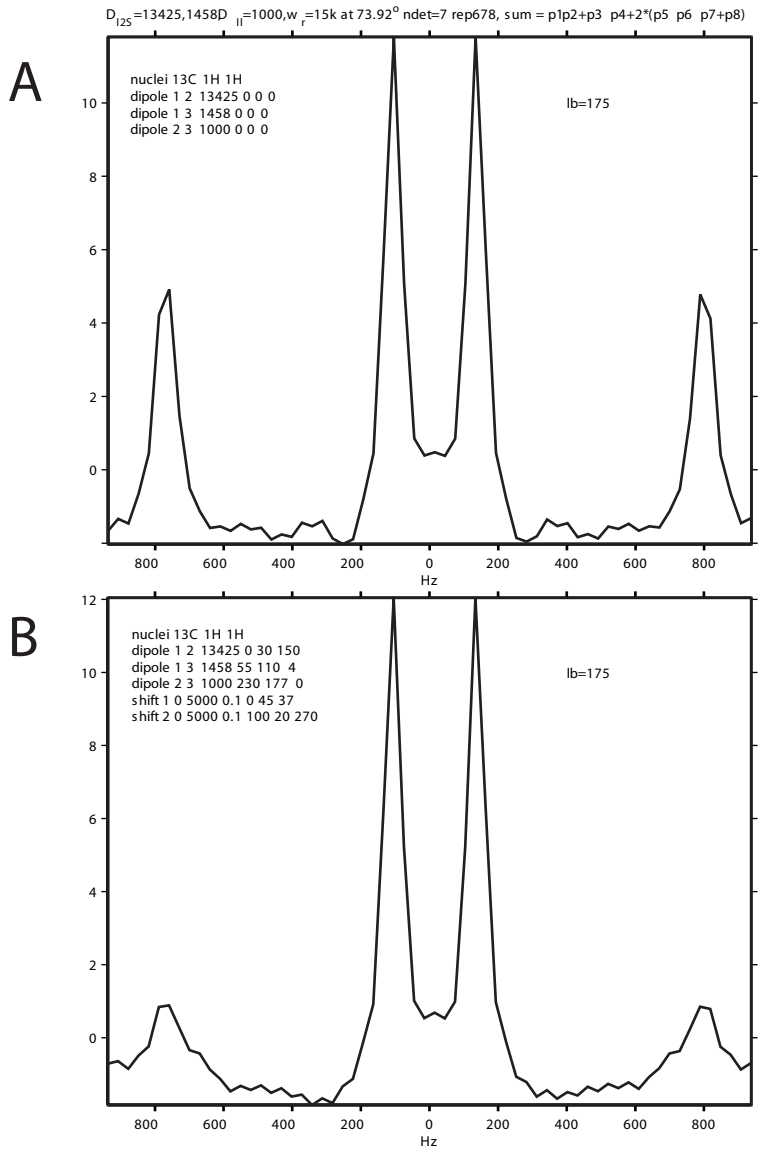

Figure 7.11: Simulation of the performance of the HETIE pulse sequence. (A) Ideal CH_2 spin system, (B) non-ideal spin system with the CSA and coupling parameters indicated on the figure.

ideal one with no CSA and a weak homonuclear proton-proton coupling (for the simulation input files, see Appendix A.2). As is shown in Figure 7.11A, the peaks are isotropic and sharp at the correct frequencies (as determined from the analytical scaling factor). It should be noted that since the spectral range is determined by the spinning speed divided by the number of evolution units per dwell (15 kHz / 8), the largest C-H coupling is actually under-sampled and is effectively folded in from the edges of the spectrum. This is an unfortunate artifact, however it is necessary given our maximum RF restrictions. Besides, the couplings which are expected to be of greatest interest for structure determinations will typically be those with small coupling values.

In continuing with the investigation of the performance of the HETIE sequence, Figure 7.11B shows the results of a simulation on a more realistic sample with non-zero Euler angles relating the axes of the interactions, as well as a 5 kHz CSA on each of the protons. Figure 7.11B indicates that the weaker coupling peaks are virtually unaffected while the larger coupling peak has some broadening which we attribute to a larger magnitude cross-term since the underlying dipolar coupling is significantly larger. This simulation in Figure 7.11B is in excess of what has previously been seen for the CSA of protons in ferrocene[102] with a $\Delta\sigma(= \sigma_{\parallel} - \sigma_{\perp})$ of -6.5 $\pm$0.1 ppm.

Finally, in Figure 7.12 the comparison is made between the ideal simulation and that of the actual experimental signal. The first thing to note is that the spectrum of Figure 7.12 is a power spectrum $(Abs(f(\omega))^2)$ which is necessary to facilitate the comparison with the simulation and this low signal to noise spectrum. Secondly, in the experimental spectrum, there is a large zero peak which has been truncated so that the peaks of interest are more clearly displayed. The origin of this peak is somewhat uncertain, however we

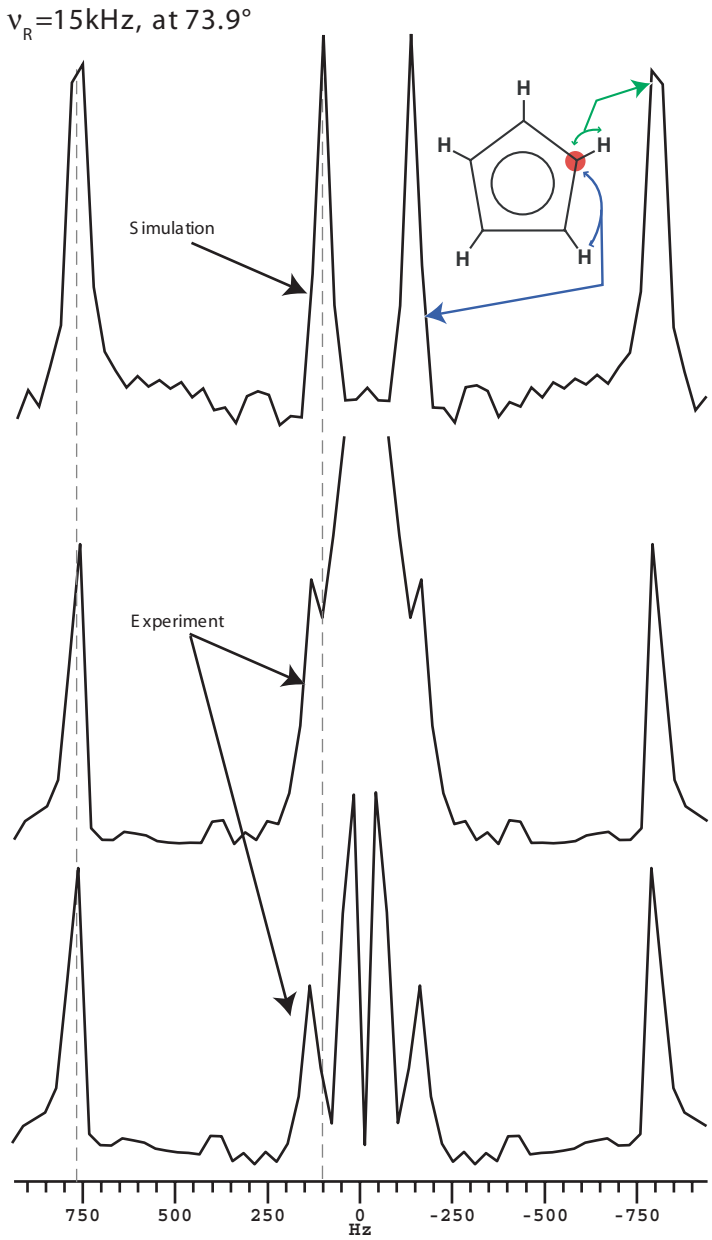

Figure 7.12: HETIE experiment and simulation comparison for $FeCp_2$, (top) the simulation uses the couplings as determined from diffraction studies, (middle) the experimental power spectrum was acquired at 300MHz, and (bottom) the *deconvolved* experimental spectrum.

suspect that it is related to the signal decay caused by the accumulation of pulse and phase errors, but requires further investigation.

The largest coupling peaks in the experimental spectrum appear to be at close to exactly the correct frequency (taking into account the spectral folding) at 1090 ± 10 Hz. The next largest coupling peak occurs at 147 ± 10 Hz and is slightly different from that found in the simulation (and noted by the dashed lines in Figure 7.12). The smallest C-H coupling peak can not be observed unless the large zero peak is deconvolved which is shown in the bottom plot of Figure 7.12 and it roughly occurs at 31.5 ±15 Hz, very close to the expected ideal value.

The heteronuclear coupling values as determined by the HETIE experiment actually agree quite well with the 'known structure' given the uncertainties in the interpretation of ferrocene diffraction studies. Thus far we have made only a single study, but with additional refinement of the HETIE sequence, we anticipate this method may yield valuable structural insight into solid samples.

Chapter 8

Conclusion

8.1 Oriented Systems

The work described in Chapters 3 and 4 represents an initial attempt at developing an area of research that holds much promise for yielding structural information in interesting systems. The 2D SAS correlations presented facilitate the assignment and resolution of dipolar couplings in complex spin systems. With this method, the larger goal of determining a complete structure is much more tractable.

The systems studied in Chapters 3 and 4 are relatively simple; however, in principle the methods can be applied to very complex spin systems such as proteins or nucleic acids. In combination with the numerous existing liquid state assignment methods, the limitations of these methods are no different than what is currently possible in liquid state structure determinations, and it is hoped that they will be applied to more interesting systems in the near future.

8.2 Solid State

8.2.1 Structure from CSA

Not unlike the methodology development in oriented systems, the solid state work presented is also in the early stages of development. The structure from CSA methods will continue to develop as *ab initio* computational methods improve providing better correlation with the experimental data. The availability of faster computers now makes computing more accurate shielding surfaces possible which only a few years ago would have been intractable. In the next year or two, it is expected that a new version of the shielding surfaces utilized in this paper will be updated with more accurate results. This method probably will be routinely utilized once these new surfaces are available due to the availability of CSA information in both solids and solutions.

8.2.2 Isotropic Dipolar Spectra

Of the variety of methods presented in this thesis for determining structure, the HOMIE and HETIE isotropic dipolar spectra experiments are the most novel. The application of these methods has been very limited due to the recent timing of the experiments. Actually, the experiments had to be halted in order to allow for the writing of this thesis. This method has great potential for providing unique information in the solid state in a form (isotropic) which is not readily available by other methods. Further demonstration of the abilities of the HETIE method is planned in a variety of samples with more diverse structures. If the method is further proven, it could facilitate for more accurate structure determinations in solids.

8.3 NMR Crystallography

None of the methods described in this thesis alone would constitute the entirety of a NMR crystallography method. A likely strategy for structure determination would be similar to what is performed in liquid state NMR where a sequence of different experimental methods are applied; each of these methods reveal different pieces of information until an appropriate structure is determined. With some developmental work applied to each of these methods, perhaps a complete structure determination methodology could be designed eventually. Until then, the developments continue.

Bibliography

[1] A. Cho and D. Normile. Mastering macromolecules. *Science*, 298, 2002.

[2] D. M. Grant and R. K. Harris, editors. *Encyclopedia of Nuclear Magnetic Resonance*, volume 1-9. Wiley, 2002.

[3] M. Mehring. *Principles of High Resolution NMR in Solids*. Springer-Verlag, New York, 2nd edition, 1983.

[4] M. Munowitz. *Coherence and NMR*. John Wiley and Sons, New York, USA, 1988.

[5] R.R. Ernst, G. Bodenhausen, and A. Wokaun. *Principles of Nuclear Magnetic Resonance in One and Two Dimensions*. Oxford University Press, New York, USA, 1987.

[6] M. Goldman. *Quantum Description of High-Resolution NMR in Liquids*. Clarendon, Oxford, 1988.

[7] J.J. Sakurai. *Modern Quantum Mechanics*. Addison-Wesley, Reading, Massachusetts, 1994.

[8] S. K. Buratto, D. N. Shykind, and D. P. Weitekamp. Time-sequenced optical nuclear-magnetic-resonance of gallium- arsenide. *Physical Review B*, 44(16):9035–9038, 1991.

[9] M. P. Augustine, D. M. TonThat, and J. Clarke. Squid detected NMR and NQR. *Solid State Nuclear Magnetic Resonance*, 11(1-2):139–156, 1998.

[10] P. Styles, N. F. Soffe, and C. A. Scott. An improved cryogenically cooled probe for high-resolution NMR. *Journal of Magnetic Resonance*, 84(2):376–378, 1989.

[11] H. D. W. Hill. Improved sensitivity of NMR spectroscopy probes by use of high-temperature superconductive detection coils. *IEEE Transactions on Applied Superconductivity*, 7(2):3750–3755, 1997.

[12] E. Fukushima and S. Roeder. *Experimental Pulse NMR: A Nuts and Bolts Approach.* Perseus Publishing, Cambridge, Massachusetts, 1986.

[13] F. Reinitzer. *Monatsh. Chem.*, 9:421, 1888. for English translation see *Liq. Cryst.* **1989**, 5, 7.

[14] S.H. Chen and N.M. Amer. *Phys. Rev. Lett.*, 51, 1983.

[15] W. Maier and A. Saupe. *Z. Naturforsch. A*, 14:882, 1959.

[16] W. Maier and A. Saupe. *Z. Naturforsch. A*, 15:287, 1960.

[17] K. Schmidt-Rohr, L. Emsley D. Nanz, and A. Pines. NMR measurement of resolved heteronuclear dipole couplings in liquid crystals and lipids. *J. Phys. Chem.*, 98:6668, 1994.

[18] W. S. Warren, D. P. Weitekamp, and A. Pines. *J. Chem. Phys.*, 73:2084, 1980.

[19] L. Emsley and A. Pines. *Proceedings of the International School of Physics.* Societa Italiana di Fisica, 1994.

[20] C. Algieri, F. Castiglione, G. Celebre, G. De Luca, M. Longeri, and J. W. Emsley. The structure of ethylbenzene as a solute in liquid crystalline solvents via analysis of proton NMR spectra. *Phys. Chem. Chem. Phys.*, 2:3405–3413, 2000.

[21] D. P. Weitekamp. Time-domain multiple-quantum NMR. *Advances In Magnetic Resonance*, 11:111–274, 1983.

[22] R. K. Hester, J. L. Ackerman, B. L. Neff, and J. S. Waugh. Separated local field spectra in NMR: Determination of structure of solids. *Phys. Rev. Lett.*, 36:1081–1083, 1976.

[23] E. Vinogradov, P. K. Madhu, and S. Vega. High-resolution proton solid-state NMR spectroscopy by phase-modulated Lee-Goldburg experiment. *Chem. Phys. Lett.*, 314:443–450, 1999.

[24] D. D. Laws, H. M. L. Bitter, and A. Jerschow. Solid-state NMR spectroscopic methods in chemistry. *Angewandte Chemie-International Edition*, 41(17):3096–3129, 2002.

[25] K. Wuthrich. *NMR of proteins and nucleic acids.* Wiley, New York, 1986.

[26] J. Cavanagh, A. G. Palmer, W. Fairbrother, and N. Skelton. *Protein Nmr Spectroscopy: Principles and Practice.* Academic Press, 1996.

[27] R.R. Ernst, G. Bodenhausen, and A. Wokaun. *Principles of Nuclear Magnetic Resonance in One and Two Dimensions.* Clarendon Press, Oxford, 1987.

[28] J. W. Emsley and J. C. Lindon. *NMR Spectroscopy Using Liquid Crystal Solvents.* Pergamon Press, Oxford, 1975.

[29] A. D. Buckingham, E. E. Burnell, and C. A. Delange. Determination of nuclear magnetic shielding anisotropies of solutes in liquid-crystal solvents. *Journal of the American Chemical Society*, 90(11):2972, 1968.

[30] E. de Alba and N. Tjandra. Nmr dipolar couplings for the structure determination of biopolymers in solution. *Progress in Nuclear Magnetic Resonance Spectroscopy*, 40(2):175–197, 2002.

[31] N. Tjandra and A. Bax. Direct measurement of distances and angles in biomolecules by NMR in a dilute liquid crystalline medium. *Science*, 278(5340):1111–1114, 1997.

[32] S. Caldarelli, M. Hong, L. Emsley, and A. Pines. Measurement of carbon-proton dipolar couplings in liquid crystals by local dipolar field NMR spectroscopy. *J. Phys. Chem.*, 100:18696, 1996.

[33] P. Lesot, J. M. Ouvrard, B. N. Ouvrard, and J. Courtieu. Coherent reduction of dipolar interactions in molecules dissolved in anisotropic media using a new multiple-pulse sequence in a COSY experiment. *J. Magn. Reson. A*, 107:141–150, 1994.

[34] M. Lee and W. Goldburg. Nuclear-magnetic-resonance line narrowing by a rotating rf field. *Phys. Rev.*, 140:1261–1271, 1965.

[35] J. Courtieu, D. W. Alderman, and D. M. Grant. Spinning near the magic angle: A means of obtaining first-order dipolar NMR spectra of molecules dissolved in nematic liquid crystals. *J. Am. Chem. Soc.*, 103:6783–6784, 1981.

[36] J. Courtieu, D. W. Alderman, D. M. Grant, and J. P. Bayles. Director dynamics

and NMR applications of nematic liquid crystals spinning at various angles from the magnetic field. *J. Chem. Phys.*, 77:723–730, 1982.

[37] J. Courtieu, J. P. Bayle, and B. M. Fung. Variable angle sample spinning NMR in liquid crystals. *Prog. Nucl. Magn. Reson. Spectrosc.*, 26:141–169, 1994.

[38] R. H. Havlin, G. H. J. Park, and A. Pines. Two-dimensional nmr correlations of liquid crystals using switched angle spinning. *Journal of Magnetic Resonance*, 157:163–169, 2002.

[39] G. Zandomeneghi, M. Tomaselli, J.D. van Beek, and B.H. Meier. Manipulation of the director in bicellar mesophases by sample spinning: A new tool for NMR spectroscopy. *J. Am. Chem. Soc.*, 123:910, 2001.

[40] D. McElheny, M. Zhou, and L. Frydman. Two-dimensional dynamic-director ^{13}c NMR in liquid crystals. *J. Magn. Reson.*, 148:436–441, 2001.

[41] L. Emsley and A. Pines. *Proceedings of the International School of Physics.* Societa Italiana di Fisica, 1994.

[42] U. Finkenzeller, T. Geelhaar, G. Weber, and L. Pohl. Liquid-crystalline reference compounds. *Liquid Crystals*, 5(1), 1989.

[43] M. Mehring. *Principles of High Resolution NMR in Solids.* Springer-Verlag, New York, 2nd edition, 1983.

[44] A. Bax, N. M. Szeverenyi, and G. E. Maciel. Chemical-shift anisotropy in powdered solids studied by 2D FT NMR with flipping of the spinning axis. *J. Magn. Reson.*, 55(3):494–497, 1983.

[45] T. Terao, H. Miura, and A. Saika. Dipolar sass nmr-spectroscopy - separation of heteronuclear dipolar powder patterns in rotating solids. *J. Chem. Phys.*, 85(7):3816–3826, 1986.

[46] A. Bax and R. Freeman. Investigation of complex networks of spin-spin coupling by two-dimensional nmr. *J. Magn. Reson.*, 44:542, 1981.

[47] C.A. Hunter and J.K.M. Sanders. The nature of pi-pi interactions. *J. Am. Chem. Soc.*, 112:5525, 1990.

[48] S.A. Smith, T.O. Levante, B.H. Meier, and R.R. Ernst. Computer simulations in magnetic resonance. an object oriented programming approach. *J. Magn. Reson.*, 106:75–105, 1994.

[49] J. Herzfeld and A. E. Berger. Sideband intensities in NMR-spectra of samples spinning at the magic angle. *Journal Of Chemical Physics*, 73(12):6021–6030, 1980.

[50] C. R. Sanders and K. Oxenoid. Customizing model membranes and samples for NMR spectroscopic studies of complex membrane proteins. *BBA-Biomembranes*, 1508(1-2):129–145, 2000.

[51] D. D. Laws, H. M. L. Bitter, and A. Jerschow. Solid-state NMR spectroscopic methods in chemistry. *Angewandte Chemie-International Edition*, 41(17):3096–3129, 2002.

[52] A. Samoson, T. Tuherm, and Z. Gan. High-field high-speed mas resolution enhancement in h-1 NMR spectroscopy of solids. *Solid State Nuclear Magnetic Resonance*, 20(3-4):130–136, 2001.

[53] A. Detken, E. H. Hardy, M. Ernst, and B. H. Meier. Simple and efficient decoupling in magic-angle spinning solid-state nmr: the xix scheme. *Chemical Physics Letters*, 356(3-4):298–304, 2002.

[54] S. Dusold and A. Sebald. Dipolar recoupling under magic-angle spinning conditions. *Annual Reports On NMR Spectroscopy*, 41:185–264, 2000.

[55] Y. K. Lee, N. D. Kumur, M. Helmle, O. G. Johannessen, N. C. Nielsen, and M. H. Levitt. Efficient dipolar recoupling in the NMR of rotating solids. a sevenfold symmetric radiofrequency pulse sequence. *Chem. Phys. Lett.*, 242:304–309, 1995.

[56] M. Carravetta, M. Edén, X. Zhao, A. Brinkmann, and M. H. Levitt. Symmetry principles for the design of radiofrequency pulse sequences in the nuclear magnetic resonance of rotating solids. *Chem. Phys. Lett.*, 321:205–215, 2000.

[57] Griffin RG Gross JD, Costa PR. Tilted n-fold symmetric radio frequency pulse sequences: Applications to csa and heteronuclear dipolar recoupling in homonuclear dipolar coupled spin networks. *J. Chem. Phys.*, 108(17):7286–7293, 1998.

[58] A. C. deDios. Ab initio calculations of the NMR chemical shift. *Progress in Nuclear Magnetic Resonance Spectroscopy*, 29(3-4):229–278, 1996.

[59] I. Ando, S. Kuroki, H. Kurosu, and T. Yamanobe. NMR chemical shift calculations and structural characterizations of polymers. *Progress in Nuclear Magnetic Resonance Spectroscopy*, 39(2):79–133, 2001.

[60] C. J. Jameson. Understanding NMR chemical shifts. *Annu. Rev. Phys. Chem.*, 47:135–169, 1996.

[61] F. R. Salsbury and R. A. Harris. Hydrogen chemical shieldings in small molecules: a magnetic field density functional approach. *Chem. Phys. Lett.*, 279(3-4):247–251, 1997.

[62] F. R. Salsbury and R. A. Harris. The current in magnetic field density functional theory and its application to the chemical shielding and magnetic susceptibility. *J. Chem. Phys.*, 107(18):7350–7359, 1997.

[63] H. B. Le, J. G. Pearson, A. C. Dedios, and E. Oldfield. Protein-structure refinement and prediction via NMR chemical- shifts and quantum-chemistry. *Journal of the American Chemical Society*, 117(13):3800–3807, 1995.

[64] J. G. Pearson, J. F. Wang, J. L. Markley, H. B. Le, and E. Oldfield. Protein-structure refinement using c-13 nuclear-magnetic- resonance spectroscopic chemical-shifts and quantum-chemistry. *Journal of the American Chemical Society*, 117(34):8823–8829, 1995.

[65] E. Oldfield. Chemical-shifts and 3-dimensional protein structures. *Journal of Biomolecular Nmr*, 5(3):217–225, 1995.

[66] D. Sitkoff and D. A. Case. Theories of chemical shift anisotropies in proteins and nucleic acids. *Progress in Nuclear Magnetic Resonance Spectroscopy*, 32:165–190, 1998.

[67] D. A. Case. The use of chemical shifts and their anisotropies in biomolecular structure determination. *Current Opinion in Structural Biology*, 8(5):624–630, 1998.

[68] D. A. Case. Interpretation of chemical shifts and coupling constants in macromolecules. *Current Opinion in Structural Biology*, 10(2):197–203, 2000.

[69] S. Spera and A. Bax. Empirical correlation between protein backbone conformation and c-alpha and c-beta c-13 nuclear-magnetic-resonance chemical- shifts. *Journal of the American Chemical Society*, 113(14):5490–5492, 1991.

[70] A. C. deDios, J. G. Pearson, and E. Oldfield. Secondary and tertiary structural effects on protein NMR chemical-shifts - an abinitio approach. *Science*, 260(5113):1491–1496, 1993.

[71] J. Heller, D. D. Laws, M. Tomaselli, D. S. King, D. E. Wemmer, A. Pines, R. H. Havlin, and E. Oldfield. Determination of dihedral angles in peptides through experimental and theoretical studies of alpha-carbon chemical shielding tensors. *Journal of the American Chemical Society*, 119(33):7827–7831, 1997.

[72] R. H. Havlin, H. B. Le, D. D. Laws, A. C. deDios, and E. Oldfield. An ab initio quantum chemical investigation of carbon-13 NMR shielding tensors in glycine, alanine, valine, isoleucine, serine, and threonine: Comparisons between helical and sheet tensors, and the effects of (x)(1) on shielding. *Journal of the American Chemical Society*, 119(49):11951–11958, 1997.

[73] M. Hong. Solid-state NMR determination of c-13 alpha chemical shift anisotropies for the identification of protein secondary structure. *Journal of the American Chemical Society*, 122(15):3762–3770, 2000.

[74] N. Tjandra, A. Szabo, and A. Bax. Protein backbone dynamics and n-15 chemical

shift anisotropy from quantitative measurement of relaxation interference effects. *J Am. Chem. Soc.*, 118(29):6986–6991, 1996.

[75] N. Tjandra and A. Bax. Large variations in c-13(alpha) chemical shift anisotropy in proteins correlate with secondary structure. *Journal of the American Chemical Society*, 119(40):9576–9577, 1997.

[76] A. E. Walling, R. E. Pargas, and A. C. deDios. Chemical shift tensors in peptides: A quantum mechanical study. *Journal of Physical Chemistry A*, 101(39):7299–7303, 1997.

[77] H. H. Sun, L. K. Sanders, and E. Oldfield. Carbon-13 NMR shielding in the twenty common amino acids: Comparisons with experimental results in proteins. *Journal of the American Chemical Society*, 124(19):5486–5495, 2002.

[78] G. Precigoux, C. Courseille, S. Geoffre, and F. Leroy. Crystal-structure of the 10-13 sequence of angiotensinogen l- leucyl-l-leucyl-l-valyl-l-tyrosyl methyl-ester. *Journal of the American Chemical Society*, 109(24):7463–7465, 1987.

[79] I. L. Karle, J. L. Flippenanderson, K. Uma, and P. Balaram. Apolar peptide models for conformational heterogeneity, hydration, and packing of polypeptide helices - crystal-structure of heptapeptides and octapeptides containing alpha- aminoisobutyric-acid. *Proteins-Structure Function and Genetics*, 7(1):62–73, 1990.

[80] I. L. Karle, J. L. Flippenanderson, K. Uma, and P. Balaram. Unfolding of an alpha-helix in peptide crystals by solvation - conformational fragility in a heptapeptide. *Biopolymers*, 33(5):827–837, 1993.

[81] R. Ditchfield. Molecular-orbital theory of magnetic shielding and magnetic susceptibility. *Journal of Chemical Physics*, 56(11):5688, 1972.

[82] J. W. Ponder and F. M. Richards. Tertiary templates for proteins - use of packing criteria in the enumeration of allowed sequences for different structural classes. *Journal of Molecular Biology*, 193(4):775–791, 1987.

[83] S. C. Lovell, J. M. Word, J. S. Richardson, and D. C. Richardson. The penultimate rotamer library. *Proteins-Structure Function and Genetics*, 40(3):389–408, 2000.

[84] S. J. Weiner, P. A. Kollman, D. A. Case, U. C. Singh, C. Ghio, G. Alagona, S. Profeta, and P. Weiner. A new force-field for molecular mechanical simulation of nucleic-acids and proteins. *Journal of the American Chemical Society*, 106(3):765–784, 1984.

[85] S. J. Weiner, P. A. Kollman, D. T. Nguyen, and D. A. Case. An all atom force-field for simulations of proteins and nucleic-acids. *Journal of Computational Chemistry*, 7(2):230–252, 1986.

[86] M. J. Frisch, G. W. Trucks, H. B. Schlegel, G. E. Scuseria, M. A. Robb, J. R. Cheeseman, V. G. Zakrzewski, Jr. Montgomery, J. A., R. E. Stratmann, J. C. Burant, S. Dapprich, J. M. Millam, A. D. Daniels, K. N. Kudin, M. C. Strain, O. Farkas, J. Tomasi, V. Barone, M. Cossi, R. Cammi, B. Mennucci, C. Pomelli, C. Adamo, S. Clifford, J. Ochterski, G. A. Petersson, Q. Ayala, P. Y. Cui, K. Morokuma, D. K. Malick, A. D. Rabuck, K. Raghavachari, J. B. Foresman, J. Cioslowski, J. V. Ortiz, A. G. Baboul, B. B. Stefanov, G. Liu, A. Liashenko, P. Piskorz, I. Komaromi, R. Gomperts, R. L. Martin, D. J. Fox, T. Keith, M. A. Al-Laham, C. Y. Peng,

A. Nanayakkara, C. Gonzalez, M. Challacombe, P. M. W. Gill, B. Johnson, W. Chen, M. W. Wong, J. L. Andres, C. Gonzalez, M. Head-Gordon, E. S. Replogle, and J. A. Pople. Gaussian98, revision a.7, 1998.

[87] D. B. Chesnut and K. D. Moore. Locally dense basis-sets for chemical-shift calculations. *Journal of Computational Chemistry*, 10(5):648–659, 1989.

[88] C. J. Jameson. Reply to 'conventions for tensor quantities used in nuclear magnetic resonance, nuclear quadrupole resonance and electron spin resonance spectroscopy'. *Solid State Nuclear Magnetic Resonance*, 11(3-4):265–268, 1998.

[89] A. C. deDios, D. D. Laws, and E. Oldfield. Predicting c-13 nuclear-magnetic-resonance chemical shielding tensors in zwitterionic l-threonine and l-tyrosine via quantum-chemistry. *Journal of the American Chemical Society*, 116(17):7784–7786, 1994.

[90] Y. X. Pang and E. R. P. Zuiderweg. Determination of protein backbone (co)-c-13 chemical shift anisotropy tensors in solution. *Journal of the American Chemical Society*, 122(19):4841–4842, 2000.

[91] E. Sternin, M. Bloom, and A. L. Mackay. De-pake-ing of NMR-spectra. *J. Magn. Reson.*, 55(2), 1983.

[92] DB. Zax, A. Bielecki, KW. Zilm, A. Pines, and DP. Weitekamp. Zero-field NMR and nqr. *J. Chem. Phys.*, 83:4877–4905, 1985.

[93] R. Tycko. Theory for zero-field NMR entirely in high field. *J. Magn. Reson.*, 75:193–197, 1987.

[94] R. Tycko. Zero-field nuclear magnetic resonance in high-field-the untruncation of dipole-dipole couplings by coherent averaging. *Phys. Rev. Lett.*, 60:2734–2737, 1988.

[95] R. Tycko. Zero field nuclear magnetic resonance in high field. *J. Chem. Phys.*, 92:5776–5793, 1990.

[96] M. E. Rose, editor. *Elementary Theory of Angular Momentum.* Wiley, New York, 1967.

[97] B.F. Chmelka, K.T. Mueller, A. Pines, J. Stebbins, Y. Wu, and J.W. Zwanziger. 0-17 NMR in solids by dynamic-angle spinning and double rotation. *Nature*, 339:42–43, 1989.

[98] M. Hohwy, H. J. Jakobsen, M. Eden, M. H. Levitt, and N. C. Nielsen. Broadband dipolar recoupling in the nuclear magnetic resonance of rotating solids: A compensated C7 pulse sequence. *J. Chem. Phys.*, 108:2686–2694, 1998.

[99] Hu Sheng-Zhi and T.C.W. Mak. *Acta Crystallogr., Sect. C (Cr. Str. Comm.)*, 42:1456, 1986. CSD ref. MMALAC01.

[100] C. P. Brock and Y. Fu. Rigid-body disorder models for the high-temperature phase of ferrocene. *Acta Cryst.*, B53:928–938, 1997.

[101] D. Braga. Dynamic processes in crystalline organometallic complexes. *Chemical Reviews*, 92(4):633–665, 1992.

[102] H. W. Spiess, H. Zimmermann, and U. Haeberlen. Proton magnetic shielding and susceptibility effects in single-crystals of ferrocene. *Chemical Physics*, 12(1):123–130, 1976.

Appendix A

Appendix

A.1 Irreducible Tensor Representations of Spin Interactions

As mentioned briefly in Chapter 2 it is sometimes more convenient to write spin interactions in spherical tensor form instead of the more familiar and experimentally relevant cartesian form.

The nine matrix elements of a cartesian second rank tensor T_{ij} (i,j=x,y,z) can be represented by:

a *scalar*

$$\mathbf{T}_0 = \frac{1}{3}Tr(T_{ij}) = \frac{1}{3}\sum_i T_{ii} \tag{A.1}$$

an *antisymmetric* first rank tensor

$$\mathbf{T}_1 : T'_{ij} = \frac{1}{2}(T_{ij} - T_{ji}) \tag{A.2}$$

with three components and zero trace, and into a traceless second rank tensor which is

symmetric

$$\mathbf{T}_2 : T''_{ij} = \frac{1}{2}(T_{ij} + T_{ji}) - \frac{1}{3}Tr(T_{ij}) \tag{A.3}$$

with five components. Now the sum of the three irreducible tensor is

$$T_{ij} = \frac{1}{3}Tr(T_{ij}) + T'_{ij} + T''_{ij} \tag{A.4}$$

The three components, scalar, antisymmetric, and symmetric, all transform in the same fashion as spherical harmonics of order zero, one and two, respectively.

Frame transformation are very common when dealing with spin interactions and it is often very useful to represent this utilizing the second rank spherical tensors . The tensor $\mathbf{T}_l$ of rank l with $2l+1$ components $\mathbf{T}_{lm}$ transforms into the new coordinate system (primed) according to the irreducible representation D_l of the rotation group[96]

$$T'_{lm} = R(\alpha\beta\gamma)T_{lm}R^{-1}(\alpha\beta\gamma) = \sum_{p=-l}^{+l} T_{lp}D^l_{pm}(\alpha\beta\gamma). \tag{A.5}$$

Using spherical unit vectors

$$\mathbf{e}_{10} = \mathbf{e}_z; \mathbf{e}_{1\pm1} = \mp(1/\sqrt{2})(\mathbf{e}_x \pm i\mathbf{e}_y) \tag{A.6}$$

the components of the first rank irreducible tensors T_{1m} in cartesian components is

$$T_{1m} = \mathbf{e}_{1m} - \mathbf{T} = \mathbf{e}_{1m} \cdot (\mathbf{e}_x T_x + \mathbf{e}_y T_y + \mathbf{e}_z T_z) \tag{A.7}$$

or

$$T_{10} = T_z; T_{1\pm1} = \mp(1/\sqrt{2})(T_x \pm iT_y) \tag{A.8}$$

In a similar fashion, the second rank irreducible spherical tensors in terms of the cartesian tensor are[3]

$$\begin{aligned}
T_{00} &= -\frac{1}{\sqrt{3}}[T_{xx} + T_{yy} + T_{zz}] \\
T_{10} &= -\frac{i}{\sqrt{2}}[T_{xy} - T_{yx}] \\
T_{1\pm1} &= -\frac{1}{2}[T_{zx} - T_{xz} \mp i(T_{zy} - T_{yz})] \\
T_{20} &= \frac{1}{\sqrt{6}}[3T_{zz} - (T_{xx} + T_{yy} + T_{zz})] \\
T_{2\pm1} &= \mp\frac{1}{2}[T_{xz} + T_{zx} \pm i(T_{yz} + T_{zy})] \\
T_{2\pm2} &= \frac{1}{2}[T_{xx} - T_{yy} \pm i(T_{xy} + Tyx)].
\end{aligned} \tag{A.9}$$

For second rank cartesian tensors which are symmetric and traceless only the second rank irreducible spherical tensor is nonzero, which is the case for dipolar coupling and quadrupolar coupling.

A.2 Simulation Programs

Listing A.1: Simpson simulation input file for HETIE pathways 1-4

```
cluster {
waugh
noether
}
spinsys {
channels 13C 1H
  nuclei 13C 1H 1H
  dipole 1 2 -13425 0 0 0
  dipole 1 3 -1458 0 0 0
  dipole 2 3 -1000 0 0 0
}

par {
    variable ndet  3
    method direct
    gamma_angles 40
```

```
    spin_rate          15000.0
    rotor_angle  73.92
    variable h1rf spin_rate*7.5
    variable hevorf spin_rate*27.0/4.0
    variable hdetrf spin_rate*15.0/2.0
    sw   spin_rate/8.0
    crystal_file       rep678
    np                 32
    start_operator      Inz
    detect_operator     I2m + I3m
    verbose            1101
    use_cluster  1
    cluster_port  3265
    variable ph_hdet   0
}

proc pulseq {} {
    global par
    maxdt 1.0

### Start H1 ###
    set t90 [expr 0.25e6/$par(h1rf)]
set phi [expr 0+$par(ph_h1)]
  for {set i 0} {$i < 5} {incr i 1} {
    foreach phi2 {180 270} {
        pulse $t90 0 0 $par(h1rf) [expr 0+$phi2+$phi]
        pulse $t90 0 0 $par(h1rf) [expr 90+$phi2+$phi]
        pulse $t90 0 0 $par(h1rf) [expr 0+$phi2+$phi]

        pulse $t90 0 0 $par(h1rf) [expr 90+$phi2+180+$phi]
        pulse $t90 0 0 $par(h1rf) [expr 0+$phi2+180+$phi]
        pulse $t90 0 0 $par(h1rf) [expr 90+$phi2+180+$phi]
    }
  }
store 1
reset

    set t90 [expr 0.25e6/$par(h1rf)]
set phi [expr 180+$par(ph_h1)]
  for {set i 0} {$i < 5} {incr i 1} {
    foreach phi2 {180 270} {
        pulse $t90 0 0 $par(h1rf) [expr 0+$phi2+$phi]
        pulse $t90 0 0 $par(h1rf) [expr 90+$phi2+$phi]
        pulse $t90 0 0 $par(h1rf) [expr 0+$phi2+$phi]

        pulse $t90 0 0 $par(h1rf) [expr 90+$phi2+180+$phi]
        pulse $t90 0 0 $par(h1rf) [expr 0+$phi2+180+$phi]
        pulse $t90 0 0 $par(h1rf) [expr 90+$phi2+180+$phi]
    }
  }
store 2
reset
### END H1 ###

### Start Hevo ###
set phi [expr 0]
    set t90 [expr 0.25e6/$par(hevorf)]
    for {set i 0} {$i < 9} {incr i 1} {
 set phi2 [expr 45+40]
        pulse $t90 0 0 $par(hevorf) [expr 0+$phi2+$phi]
        pulse $t90 0 0 $par(hevorf) [expr 90+$phi2+$phi]
        pulse $t90 0 0 $par(hevorf) [expr 0+$phi2+$phi]

 set phi2 [expr 45+140]
        pulse $t90 0 0 $par(hevorf) [expr 90+$phi2+$phi]
        pulse $t90 0 0 $par(hevorf) [expr 0+$phi2+$phi]
        pulse $t90 0 0 $par(hevorf) [expr 90+$phi2+$phi]
    }
store 3
reset

set phi [expr 180]
    set t90 [expr 0.25e6/$par(hevorf)]
    for {set i 0} {$i < 9} {incr i 1} {
 set phi2 [expr 45+40]
        pulse $t90 0 0 $par(hevorf) [expr 0+$phi2+$phi]
        pulse $t90 0 0 $par(hevorf) [expr 90+$phi2+$phi]
        pulse $t90 0 0 $par(hevorf) [expr 0+$phi2+$phi]

 set phi2 [expr 45+140]
        pulse $t90 0 0 $par(hevorf) [expr 90+$phi2+$phi]
        pulse $t90 0 0 $par(hevorf) [expr 0+$phi2+$phi]
        pulse $t90 0 0 $par(hevorf) [expr 90+$phi2+$phi]
    }
store 4
reset
```

```
#Hdet

set t90 [expr 0.25e6/$par(hdetrf)]
set phi [expr 0+$par(ph_hdet)]
  for {set i 0} {$i < 5} {incr i 1} {
    foreach phi2 {0 90} {
        pulse $t90 0 0 $par(hdetrf) [expr 0+18+$phi2+$phi]
        pulse $t90 0 0 $par(hdetrf) [expr 90+18+$phi2+$phi]
        pulse $t90 0 0 $par(hdetrf) [expr 0+18+$phi2+$phi]

        pulse $t90 0 0 $par(hdetrf) [expr 90+18+144+$phi2+$phi]
        pulse $t90 0 0 $par(hdetrf) [expr 0+18+144+$phi2+$phi]
        pulse $t90 0 0 $par(hdetrf) [expr 90+18+144+$phi2+$phi]
    }
  }
store 5
reset

set t90 [expr 0.25e6/$par(hdetrf)]
set phi [expr 180+$par(ph_hdet)]
  for {set i 0} {$i < 5} {incr i 1} {
    foreach phi2 {0 90} {
        pulse $t90 0 0 $par(hdetrf) [expr 0+18+$phi2+$phi]
        pulse $t90 0 0 $par(hdetrf) [expr 90+18+$phi2+$phi]
        pulse $t90 0 0 $par(hdetrf) [expr 0+18+$phi2+$phi]

        pulse $t90 0 0 $par(hdetrf) [expr 90+18+144+$phi2+$phi]
        pulse $t90 0 0 $par(hdetrf) [expr 0+18+144+$phi2+$phi]
        pulse $t90 0 0 $par(hdetrf) [expr 90+18+144+$phi2+$phi]
    }
  }
store 6
reset

### END Hdet ###

acq
    for {set i 1} {$i < $par(np)} {incr i} {
 reset
 for {set j 1} {$j <= $i} {incr j} {
   if [expr $j%2 == 1] {
     prop 1
     pulseid 2 250000 0 0 0
     prop 2
   } else {
     prop 2
      pulseid 2 250000 0 0 0
     prop 1
   }
 }
 for {set j $i} {$j > 0} {incr j -1} {
   set k [expr $i%2]
   if [expr $j%2 == 1] {
     prop 4
      pulseid 2 250000 0 0 0
     prop 3
   } else {
     prop 3
      pulseid 2 250000 0 0 0
     prop 4
   }
 }
 if [expr $par(hdet1) == 0] {
   for {set j 1} {$j <= $par(ndet)} {incr j} {
     if [expr $j%2 == 1] {
               prop 6
               pulseid 2 250000 0 0 0
               prop 5
     } else {
               prop 5
               pulseid 2 250000 0 0 0
               prop 6
     }
     }
 } else {
   for {set j 1} {$j <= $par(ndet)} {incr j} {
     if [expr $j%2 == 1] {
               prop 5
               pulseid 2 250000 0 0 0
               prop 6
     } else {
               prop 6
               pulseid 2 250000 0 0 0
               prop 5
     }
```

```
   }
 }
 for {set j $par(ndet)} {$j > 0} {incr j -1} {
   if [expr $j%2 == 1] {
            prop 6
            pulseid 2 250000 0 0 0
            prop 5
   } else {
            prop 5
            pulseid 2 250000 0 0 0
            prop 6
   }
 }
# ACQUIRE PULSE
        pulseid 1 0 0 250000 0
        acq
    }
}

proc main {} {
    global par

set k $par(ndet)
    set par(ph_h1) 0
    set par(hdet1) 0
   for {set j 1} {$j <= 4} {incr j 1} {
    if [expr $j%2 == 0] {
      set par(hdet1) 180
    }
    if [expr $j > 2] {
      set par(ph_h1) 180
    }

set f [fsimpson]
    fsave $f $par(name)_$j.d.$k.fid
    fzerofill $f 64
    faddlb $f 10 0
    fft $f
    fphase $f -rp 90
    fsave $f $par(name)_$j.d.$k.spe
    }
}
```

Listing A.2: Simpson simulation input file for HETIE pathways 5-8

```
cluster {
waugh
noether
}
spinsys {
channels 13C 1H
  nuclei 13C 1H 1H
  dipole 1 2 -13425 0 0 0
  dipole 1 3 -1458 0 0 0
  dipole 2 3 -1000 0 0 0
}

par {
    variable ndet  3
    method direct
    gamma_angles 40
    spin_rate          15000.0
    rotor_angle  73.92
    variable h1rf spin_rate*7.5
    variable hevorf spin_rate*27.0/4.0
    variable hdetrf spin_rate*15.0/2.0
    sw   spin_rate/8.0
    crystal_file   rep678
    np                 32
    start_operator      Inz
    detect_operator     I2m + I3m
    verbose            1101
    use_cluster  1
    cluster_port  3265
    variable ph_hdet  0
}

proc pulseq {} {
    global par
    maxdt 1.0

### Start H1 ###
    set t90 [expr 0.25e6/$par(h1rf)]
set phi [expr 0+$par(ph_h1)]
  for {set i 0} {$i < 5} {incr i 1} {
```

```
    foreach phi2 {180 270} {
        pulse $t90 0 0 $par(h1rf) [expr 0+$phi2+$phi]
        pulse $t90 0 0 $par(h1rf) [expr 90+$phi2+$phi]
        pulse $t90 0 0 $par(h1rf) [expr 0+$phi2+$phi]

        pulse $t90 0 0 $par(h1rf) [expr 90+$phi2+180+$phi]
        pulse $t90 0 0 $par(h1rf) [expr 0+$phi2+180+$phi]
        pulse $t90 0 0 $par(h1rf) [expr 90+$phi2+180+$phi]
    }
  }
store 1
reset

    set t90 [expr 0.25e6/$par(h1rf)]
set phi [expr 180+$par(ph_h1)]
  for {set i 0} {$i < 5} {incr i 1} {
    foreach phi2 {180 270} {
        pulse $t90 0 0 $par(h1rf) [expr 0+$phi2+$phi]
        pulse $t90 0 0 $par(h1rf) [expr 90+$phi2+$phi]
        pulse $t90 0 0 $par(h1rf) [expr 0+$phi2+$phi]

        pulse $t90 0 0 $par(h1rf) [expr 90+$phi2+180+$phi]
        pulse $t90 0 0 $par(h1rf) [expr 0+$phi2+180+$phi]
        pulse $t90 0 0 $par(h1rf) [expr 90+$phi2+180+$phi]
    }
  }
store 2
reset
### END H1 ###

### Start Hevo ###
set phi [expr 0]
    set t90 [expr 0.25e6/$par(hevorf)]
    for {set i 0} {$i < 9} {incr i 1} {
 set phi2 [expr 45+40]
        pulse $t90 0 0 $par(hevorf) [expr 0+$phi2+$phi]
        pulse $t90 0 0 $par(hevorf) [expr 90+$phi2+$phi]
        pulse $t90 0 0 $par(hevorf) [expr 0+$phi2+$phi]

 set phi2 [expr 45+140]
        pulse $t90 0 0 $par(hevorf) [expr 90+$phi2+$phi]
        pulse $t90 0 0 $par(hevorf) [expr 0+$phi2+$phi]
        pulse $t90 0 0 $par(hevorf) [expr 90+$phi2+$phi]
    }
store 3
reset

set phi [expr 180]
    set t90 [expr 0.25e6/$par(hevorf)]
    for {set i 0} {$i < 9} {incr i 1} {
 set phi2 [expr 45+40]
        pulse $t90 0 0 $par(hevorf) [expr 0+$phi2+$phi]
        pulse $t90 0 0 $par(hevorf) [expr 90+$phi2+$phi]
        pulse $t90 0 0 $par(hevorf) [expr 0+$phi2+$phi]

 set phi2 [expr 45+140]
        pulse $t90 0 0 $par(hevorf) [expr 90+$phi2+$phi]
        pulse $t90 0 0 $par(hevorf) [expr 0+$phi2+$phi]
        pulse $t90 0 0 $par(hevorf) [expr 90+$phi2+$phi]
    }
store 4
reset

#Hdet

set t90 [expr 0.25e6/$par(hdetrf)]
set phi [expr 0+$par(ph_hdet)]
  for {set i 0} {$i < 5} {incr i 1} {
    foreach phi2 {0 90} {
        pulse $t90 0 0 $par(hdetrf) [expr 0+18+$phi2+$phi]
        pulse $t90 0 0 $par(hdetrf) [expr 90+18+$phi2+$phi]
        pulse $t90 0 0 $par(hdetrf) [expr 0+18+$phi2+$phi]

        pulse $t90 0 0 $par(hdetrf) [expr 90+18+144+$phi2+$phi]
        pulse $t90 0 0 $par(hdetrf) [expr 0+18+144+$phi2+$phi]
        pulse $t90 0 0 $par(hdetrf) [expr 90+18+144+$phi2+$phi]
    }
  }
store 5
reset

set t90 [expr 0.25e6/$par(hdetrf)]
set phi [expr 180+$par(ph_hdet)]
  for {set i 0} {$i < 5} {incr i 1} {
    foreach phi2 {0 90} {
        pulse $t90 0 0 $par(hdetrf) [expr 0+18+$phi2+$phi]
```

```
        pulse $t90 0 0 $par(hdetrf) [expr 90+18+$phi2+$phi]
        pulse $t90 0 0 $par(hdetrf) [expr 0+18+$phi2+$phi]

        pulse $t90 0 0 $par(hdetrf) [expr 90+18+144+$phi2+$phi]
        pulse $t90 0 0 $par(hdetrf) [expr 0+18+144+$phi2+$phi]
        pulse $t90 0 0 $par(hdetrf) [expr 90+18+144+$phi2+$phi]
    }
  }
store 6
reset

### END Hdet ###
## Hdet2 ##

set t90 [expr 0.25e6/$par(hdetrf)]
set phi [expr 0]
  for {set i 0} {$i < 5} {incr i 1} {
    foreach phi2 {0 90} {
        pulse $t90 0 0 $par(hdetrf) [expr 90-18+$phi2+$phi]
        pulse $t90 0 0 $par(hdetrf) [expr 0-18+$phi2+$phi]
        pulse $t90 0 0 $par(hdetrf) [expr 90-18+$phi2+$phi]

        pulse $t90 0 0 $par(hdetrf) [expr 0+198+$phi2+$phi]
        pulse $t90 0 0 $par(hdetrf) [expr 90+198+$phi2+$phi]
        pulse $t90 0 0 $par(hdetrf) [expr 0+198+$phi2+$phi]
    }
  }
store 7
reset

set t90 [expr 0.25e6/$par(hdetrf)]
set phi [expr 180]
  for {set i 0} {$i < 5} {incr i 1} {
    foreach phi2 {0 90} {
        pulse $t90 0 0 $par(hdetrf) [expr 90-18+$phi2+$phi]
        pulse $t90 0 0 $par(hdetrf) [expr 0-18+$phi2+$phi]
        pulse $t90 0 0 $par(hdetrf) [expr 90-18+$phi2+$phi]

        pulse $t90 0 0 $par(hdetrf) [expr 0+198+$phi2+$phi]
        pulse $t90 0 0 $par(hdetrf) [expr 90+198+$phi2+$phi]
        pulse $t90 0 0 $par(hdetrf) [expr 0+198+$phi2+$phi]
    }
  }
store 8
reset
### END Hdet ###


acq
    for {set i 1} {$i < $par(np)} {incr i} {
 reset
 for {set j 1} {$j <= $i} {incr j} {
   if [expr $j%2 == 1] {
     prop 1
     pulseid 2 250000 0 0 0
     prop 2
   } else {
     prop 2
      pulseid 2 250000 0 0 0
     prop 1
   }
 }
 for {set j $i} {$j > 0} {incr j -1} {
   set k [expr $i%2]
   if [expr $j%2 == 1] {
     prop 4
      pulseid 2 250000 0 0 0
     prop 3
   } else {
     prop 3
      pulseid 2 250000 0 0 0
     prop 4
   }
 }
 if [expr $par(hdet1) == 0] {
   for {set j 1} {$j <= $par(ndet)} {incr j} {
     if [expr $j%2 == 1] {
              prop 6
              pulseid 2 250000 0 0 0
              prop 5
     } else {
              prop 5
              pulseid 2 250000 0 0 0
              prop 6
     }
     }
```

```
 } else {
   for {set j 1} {$j <= $par(ndet)} {incr j} {
     if [expr $j%2 == 1] {
              prop 5
              pulseid 2 250000 0 0 0
              prop 6
     } else {
              prop 6
              pulseid 2 250000 0 0 0
              prop 5
     }
   }
 }
 for {set j $par(ndet)} {$j > 0} {incr j -1} {
   if [expr $j%2 == 1] {
            prop 8
            pulseid 2 250000 0 0 0
            prop 7
   } else {
            prop 7
            pulseid 2 250000 0 0 0
            prop 8
   }
 }
# ACQUIRE PULSE
        pulseid 1 0 0 250000 0
        acq
    }
}

proc main {} {
    global par

   set k $par(ndet)
    set par(ph_h1) 0
    set par(hdet1) 0
   for {set j 1} {$j <= 4} {incr j 1} {
    if [expr $j%2 == 0] {
      set par(hdet1) 180
    }
    if [expr $j > 2] {
      set par(ph_h1) 180
    }
    set nk [expr $j+4]
set f [fsimpson]
    fsave $f $par(name)_$nk.d.$k.fid
    fzerofill $f 64
    faddlb $f 10 0
    fft $f
    fphase $f -rp 90
    fsave $f $par(name)_$nk.d.$k.spe
    }
}
```

A.3 Pulse Sequences

Listing A.3: Infinity+ pulse program for HETIE pathways 1-4

```
name "isohet_HETIE";
title "isohet_HETIE";

!  COMPILED WITH OPTIMIZATION ON
!  $Header: /usr2/users/applab/CFR/ppg/cp_postC7_2D.s,v 1.1 1998/11/05 22:44:25 applab Exp $
!   InfinityPlus Compatible

 NMRchnls RF: ch1 ch2; NMRacq;

!-----------------------------------------------
! Define variables in .data section
!-----------------------------------------------

.data
.long hd1=0;
.long count3d=0;
.long path=0; ! Number of Hdetections to optimize signal
.long extern nhdet=1; ! Number of Hdetections to optimize signal
.time   extern autofix  pw90Hevo = 1.0us;
.time   extern autofix  pw90Hdet = 1.0us;
.time           autofix     PW90Hevo        "pw360X*.25 - TPM1"       = 2.0us;
.time           autofix     PW90Hdet        "pw360X*.25 - TPM1"       = 2.0us;
.time           autofix     PW90H       "pw360X*.25 - TPM1"       = 2.0us;
.time autofix xdelay = 100us; ! Delay to center the pi pulse on the S spin
.time autofix evodelay = 100us; ! Delay to center the pi pulse on the S spin for Hevo
```

```
.time autofix detdelay = 100us; ! Delay to center the pi pulse on the S spin for Hevo
.freq extern rspeed;
.long   k,j,x,States_Flag,halfal;
.long ncyc2d; !2D counter
.time  extern al2d  = 50ms;
.long   i  = 1;
.ampl extern autofix aH1=0.01;
.ampl extern autofix aHevo=0.01;
.ampl  autofix aHdet=0.01; !HDET
.phase list X180[]=0,0;
.phase autofix list H1[240]; ! empty autofixed list to accept designated phases at runtime
.phase autofix list Hevo[216]; ! empty autofixed list to accept designated phases at runtime
.phase autofix list Hdet1[240]; ! empty autofixed list to accept designated phases at runtime
.phase autofix list Hdet2[240]; ! empty autofixed list to accept designated phases at runtime
.phase list last[]=0,180,90,270; !phase for pulse before Acq
.phase lastp;
.long   extern list abph[]   = 0,2,1,3; !Note odd - even = path1 - path2

include "./phases.inc";
include "../includes/STANDARD_PARAMS";
include "../includes/THREE_D.inc";

!-----------------------------------------------
! update Spinsight with calculations.
!-----------------------------------------------

.update "rb=1.30*sw";
.update "aqtm=(dw*al)";
.update "dw2 = (2.0*60.0*pw90H)+(2.0*54.0*pw90Hevo)";
.update "al2d = AL2*(dw2)";
.update "rspeed = (1.0/(7500.0*4.00*pw90H)+1.0/(6750.0*4.0*pw90Hevo))/2.0";
.update "extm = (pw90H+(AL2*dw2)+ad+rd+aqtm+pd)";
.update "txduty1=(pw90H+(AL2*dw2)+ad+rd+aqtm)/extm";
.update "time1d = (na+dp)*extm*2.0/60.0";

!-----------------------------------------------
!  Executed once at Start of Experiment
!-----------------------------------------------

.program

dataxfer= al2*al3;
dpc = dp;
PW90H = pw90H;
PW90Hevo = pw90Hevo;
PW90Hdet = PW90H;
aHdet=aH1;
xdelay=pw90H*60.0-pw180X/2.0;
evodelay=pw90Hevo*54.0-pw180X/2.0;
detdelay=xdelay;
path=1;
count3d=1;

.start

!LOOP3D
!{
ncyc2d=1;
    loop2D
    {
        abph = abph.start;
     last = last.start;
     hd1=1; ! re-initialize counter to decide which of the 4 to apply
        loop1D
        {
            call mainseq;
   hd1++;
        }
    if (count3d%AL2 == 0) {
 path++;
 ncyc2d=0;
    }
    count3d++;
    ncyc2d++;
    }
!path++;
!}

.end

!=================================================================!
mainseq:
 if (hd1 > 4) { hd1=1; }
 if (hd1 == 1) {
   aqph=@abph++;
   lastp=@last++;
```

```
    }
!Pi phase shift both H1 and Hevo to give a filter
if (hd1%2 == 1) {
 if (path < 3) {
  H1 = H1_0110.start;
  Hevo = Hevo_1001.start;
  if (ncyc2d%2 == 0) { Hevo = Hevo_0110.start; }
 } else {
  H1 = H1_1001.start;
  Hevo = Hevo_0110.start;
  if (ncyc2d%2 == 0) { Hevo = Hevo_1001.start; }
 }
}
! Pi phase shift of H1 and Hevo for filter
if (hd1%2 == 0) {
 if (path > 2) {
  H1 = H1_0110.start;
  Hevo = Hevo_1001.start;
  if (ncyc2d%2 == 0) { Hevo = Hevo_0110.start; }
 } else {
  H1 = H1_1001.start;
  Hevo = Hevo_0110.start;
  if (ncyc2d%2 == 0) { Hevo = Hevo_1001.start; }
 }
}

!! Alternate Hdets+Pi for hd1>2
if (hd1 > 2) {
 !!Alternate Hdet1
 if (path%2 == 0) {
  Hdet1 = Hdet_0110.start; ! odd points phase=0
 } else {
  Hdet1 = Hdet_1001.start; ! even points phase=180
 }
 !Match Hdet2 with Hdet1
 Hdet2 = Hdet_0110.start;
 if (nhdet%2 == 0) { Hdet2 = Hdet_1001.start; }
} else {
    !!Alternate Hdet1
    if (path%2 == 0) {
        Hdet1 = Hdet_1001.start; ! even points phase=180
    } else {
        Hdet1 = Hdet_0110.start; ! odd points phase=0
    }
    !Match Hdet2 with Hdet1
    Hdet2 = Hdet_1001.start;
    if (nhdet%2 == 0) { Hdet2 = Hdet_0110.start; }
}
!!! END Logic..

 out  time(10u);
Async;
ch++ ch1;
 out  time(10u);
 out   time(10u) ch1:SC(scH)     ;
 out   time(10u) ch1: OUTA aH1  ;
! Apply H1 01 or 10 for 4 rotors ncyc2d times
for (j=0, j < ncyc2d, j++)
  {
    do(120)
        {
!             out  PM1  ch1:TG|OUTAP aH1|@H1++;
            out  PW90H       ch1:TG|OUTAP aH1|@H1++;
        }
  }
! Apply Hevo 01 or 10 for 4 rotors ncyc2d times
for (j=0, j < ncyc2d, j++)
  {
    do(108)
        {
!             out  PM1  ch1:TG|OUTAP aHevo|@Hevo++;
            out  PW90Hevo       ch1:TG|OUTAP aHevo|@Hevo++;
        }
  }

! Apply Hdet1 01 or 10 for 4 rotors nhdet times
for (j=0, j < nhdet, j++) {
    do(120)
        {
!             out  PM1  ch1:TG|OUTAP aHdet|@Hdet1++;
            out  PW90Hdet       ch1:TG|OUTAP aHdet|@Hdet1++;
        }
}
! Apply Hdet2 01 or 10 for 4 rotors nhdet times
for (j=0, j < nhdet, j++) {
    do(120)
```

```
        {
!             out  PM1  ch1:TG|OUTAP aHdet|@Hdet2++;
             out  PW90Hdet       ch1:TG|OUTAP aHdet|@Hdet2++;
        }
}
!    out PM1   ch1:TG|P(lastp);
 out PW90Hdet  ch1:TG|P(lastp);
 out  rd    ch1:TB|P(p);
 out  ad    ch1:RE|TB;
 outAQ dw  ch1:RE|TB,al;
Sync;
ch--;

ch++ ch2;
 out  time(10u);
 out   time(10u) ch2:SC(scX)     ;
 out   time(10u) ch2:AP(aX,@X180) ;

for (k=0, k < ncyc2d, k++)
  {
     out xdelay;
 out pw180X  ch2:TG;
 out xdelay;
  }
for (k=0, k < ncyc2d, k++)
  {
     out evodelay;
 out pw180X  ch2:TG;
 out evodelay;
  }

for (k=0, k < nhdet, k++) {
     out detdelay;
 out pw180X  ch2:TG;
 out detdelay;
}
for (k=0, k < nhdet, k++) {
     out detdelay;
 out pw180X  ch2:TG;
 out detdelay;
}
  waitS;
ch--;

scan pd;
return;
```

Listing A.4: Infinity+ pulse program phases for HETIE pathways 1-4

```
!ihet_p12 phases
.phase autofix list H1_0110[]=  180,270,180,90,0,90,270,0,270,180,90,180,
                180,270,180,90,0,90,270,0,270,180,90,180,
                180,270,180,90,0,90,270,0,270,180,90,180,
                180,270,180,90,0,90,270,0,270,180,90,180,
                180,270,180,90,0,90,270,0,270,180,90,180,
                0,90,0,270,180,270,90,180,90,0,270,0,
                0,90,0,270,180,270,90,180,90,0,270,0,
                0,90,0,270,180,270,90,180,90,0,270,0,
                0,90,0,270,180,270,90,180,90,0,270,0,
                0,90,0,270,180,270,90,180,90,0,270,0,
                0,90,0,270,180,270,90,180,90,0,270,0,
                0,90,0,270,180,270,90,180,90,0,270,0,
                0,90,0,270,180,270,90,180,90,0,270,0,
                0,90,0,270,180,270,90,180,90,0,270,0,
                0,90,0,270,180,270,90,180,90,0,270,0,
                180,270,180,90,0,90,270,0,270,180,90,180,
                180,270,180,90,0,90,270,0,270,180,90,180,
                180,270,180,90,0,90,270,0,270,180,90,180,
                180,270,180,90,0,90,270,0,270,180,90,180,
                180,270,180,90,0,90,270,0,270,180,90,180;

.phase autofix list H1_1001[]=  0,90,0,270,180,270,90,180,90,0,270,0,
                0,90,0,270,180,270,90,180,90,0,270,0,
                0,90,0,270,180,270,90,180,90,0,270,0,
                0,90,0,270,180,270,90,180,90,0,270,0,
                0,90,0,270,180,270,90,180,90,0,270,0,
                180,270,180,90,0,90,270,0,270,180,90,180,
                180,270,180,90,0,90,270,0,270,180,90,180,
                180,270,180,90,0,90,270,0,270,180,90,180,
                180,270,180,90,0,90,270,0,270,180,90,180,
                180,270,180,90,0,90,270,0,270,180,90,180,
                180,270,180,90,0,90,270,0,270,180,90,180,
                180,270,180,90,0,90,270,0,270,180,90,180,
                180,270,180,90,0,90,270,0,270,180,90,180,
                180,270,180,90,0,90,270,0,270,180,90,180,
                180,270,180,90,0,90,270,0,270,180,90,180,
```

```
                180,270,180,90,0,90,270,0,270,180,90,180,
                0,90,0,270,180,270,90,180,90,0,270,0,
                0,90,0,270,180,270,90,180,90,0,270,0,
                0,90,0,270,180,270,90,180,90,0,270,0,
                0,90,0,270,180,270,90,180,90,0,270,0,
                0,90,0,270,180,270,90,180,90,0,270,0;
.phase autofix list Hevo_1001[]=
265,355,265, 95,  5, 95, 265,355,265, 95,  5, 95, 265,355,265, 95,  5, 95, 265,355,265, 95,  5, 95,
265,355,265, 95,  5, 95,
265,355,265, 95,  5, 95, 265,355,265, 95,  5, 95, 265,355,265, 95,  5, 95, 265,355,265, 95,  5, 95,
 85,175, 85,275,185,275,  85,175, 85,275,185,275,  85,175, 85,275,185,275,  85,175, 85,275,185,275,
 85,175, 85,275,185,275,
 85,175, 85,275,185,275,  85,175, 85,275,185,275,  85,175, 85,275,185,275,  85,175, 85,275,185,275,
 85,175, 85,275,185,275,  85,175, 85,275,185,275,  85,175, 85,275,185,275,  85,175, 85,275,185,275,
 85,175, 85,275,185,275,
 85,175, 85,275,185,275,  85,175, 85,275,185,275,  85,175, 85,275,185,275,  85,175, 85,275,185,275,
265,355,265, 95,  5, 95, 265,355,265, 95,  5, 95, 265,355,265, 95,  5, 95, 265,355,265, 95,  5, 95,
265,355,265, 95,  5, 95,
265,355,265, 95,  5, 95, 265,355,265, 95,  5, 95, 265,355,265, 95,  5, 95, 265,355,265, 95,  5, 95;

.phase autofix list Hevo_0110[]=
 85,175, 85,275,185,275,  85,175, 85,275,185,275,  85,175, 85,275,185,275,  85,175, 85,275,185,275,
 85,175, 85,275,185,275,
 85,175, 85,275,185,275,  85,175, 85,275,185,275,  85,175, 85,275,185,275,  85,175, 85,275,185,275,
265,355,265, 95,  5, 95, 265,355,265, 95,  5, 95, 265,355,265, 95,  5, 95, 265,355,265, 95,  5, 95,
265,355,265, 95,  5, 95,
265,355,265, 95,  5, 95, 265,355,265, 95,  5, 95, 265,355,265, 95,  5, 95, 265,355,265, 95,  5, 95,
265,355,265, 95,  5, 95, 265,355,265, 95,  5, 95, 265,355,265, 95,  5, 95, 265,355,265, 95,  5, 95,
265,355,265, 95,  5, 95,
265,355,265, 95,  5, 95, 265,355,265, 95,  5, 95, 265,355,265, 95,  5, 95, 265,355,265, 95,  5, 95,
 85,175, 85,275,185,275,  85,175, 85,275,185,275,  85,175, 85,275,185,275,  85,175, 85,275,185,275,
 85,175, 85,275,185,275,
 85,175, 85,275,185,275,  85,175, 85,275,185,275,  85,175, 85,275,185,275,  85,175, 85,275,185,275;


.phase autofix list Hdet_0110[]=    18,108,18,252,162,252,108,198,108,342,252,342,
                        18,108,18,252,162,252,108,198,108,342,252,342,
                        18,108,18,252,162,252,108,198,108,342,252,342,
                        18,108,18,252,162,252,108,198,108,342,252,342,
                        18,108,18,252,162,252,108,198,108,342,252,342,  ! 0
                        198,288,198,72,342,72,288,18,288,162,72,162,
                        198,288,198,72,342,72,288,18,288,162,72,162,
                        198,288,198,72,342,72,288,18,288,162,72,162,
                        198,288,198,72,342,72,288,18,288,162,72,162,
                        198,288,198,72,342,72,288,18,288,162,72,162,    ! Pi
                        198,288,198,72,342,72,288,18,288,162,72,162,
                        198,288,198,72,342,72,288,18,288,162,72,162,
                        198,288,198,72,342,72,288,18,288,162,72,162,
                        198,288,198,72,342,72,288,18,288,162,72,162,
                        198,288,198,72,342,72,288,18,288,162,72,162,    ! Pi
                        18,108,18,252,162,252,108,198,108,342,252,342,
                        18,108,18,252,162,252,108,198,108,342,252,342,
                        18,108,18,252,162,252,108,198,108,342,252,342,
                        18,108,18,252,162,252,108,198,108,342,252,342,
                        18,108,18,252,162,252,108,198,108,342,252,342;  ! 0
.phase autofix list Hdet_1001[]=    198,288,198,72,342,72,288,18,288,162,72,162,
                        198,288,198,72,342,72,288,18,288,162,72,162,
                        198,288,198,72,342,72,288,18,288,162,72,162,
                        198,288,198,72,342,72,288,18,288,162,72,162,
                        198,288,198,72,342,72,288,18,288,162,72,162,    ! Pi
                        18,108,18,252,162,252,108,198,108,342,252,342,
                        18,108,18,252,162,252,108,198,108,342,252,342,
                        18,108,18,252,162,252,108,198,108,342,252,342,
                        18,108,18,252,162,252,108,198,108,342,252,342,
                        18,108,18,252,162,252,108,198,108,342,252,342,  ! 0
                        18,108,18,252,162,252,108,198,108,342,252,342,
                        18,108,18,252,162,252,108,198,108,342,252,342,
                        18,108,18,252,162,252,108,198,108,342,252,342,
                        18,108,18,252,162,252,108,198,108,342,252,342,
                        18,108,18,252,162,252,108,198,108,342,252,342,  ! 0
             198,288,198,72,342,72,288,18,288,162,72,162,
                        198,288,198,72,342,72,288,18,288,162,72,162,
                        198,288,198,72,342,72,288,18,288,162,72,162,
                        198,288,198,72,342,72,288,18,288,162,72,162,
                        198,288,198,72,342,72,288,18,288,162,72,162;    ! Pi
```

Listing A.5: Infinity+ pulse program for HETIE pathways 5-8

```
name "isohet_HETIE";
title "isohet_HETIE";

!  COMPILED WITH OPTIMIZATION ON
!  $Header: /usr2/users/applab/CFR/ppg/cp_postC7_2D.s,v 1.1 1998/11/05 22:44:25 applab Exp $
!   InfinityPlus Compatible
```

```
 NMRchnls RF: ch1 ch2; NMRacq;

!-----------------------------------------------
! Define variables in .data section
!-----------------------------------------------

.data
.long hd1=0;
.long count3d=0;
.long path=0; ! set the pathway
.long extern nhdet=1; ! Number of Hdetections to optimize signal
.time   extern autofix  pw90Hevo = 1.0us;
.time           autofix     PW90Hevo        "pw360X*.25 - TPM1"        = 2.0us;
.time           autofix     PW90Hdet        "pw360X*.25 - TPM1"        = 2.0us;
.time           autofix     PW90H        "pw360X*.25 - TPM1"        = 2.0us;
.time autofix xdelay = 100us; ! Delay to center the pi pulse on the S spin
.time autofix evodelay = 100us; ! Delay to center the pi pulse on the S spin for Hevo
.time autofix detdelay = 100us; ! Delay to center the pi pulse on the S spin for Hevo
.freq extern rspeed;
.long   k,j,x,States_Flag,halfal;
.long ncyc2d; !2D counter
.time  extern al2d  = 50ms;
.long   i  = 1;
.ampl extern autofix aH1=0.01;
.ampl extern autofix aHevo=0.01;
.ampl autofix aHdet=0.01;
.phase list X180[]=0,0;
.phase autofix list H1[240]; ! empty autofixed list to accept designated phases at runtime
.phase autofix list Hevo[216]; ! empty autofixed list to accept designated phases at runtime
.phase autofix list Hdet1[240]; ! empty autofixed list to accept designated phases at runtime
.phase autofix list Hdet2[240]; ! empty autofixed list to accept designated phases at runtime
.phase list last[]=0,180,90,270; !phase for pulse before Acq
.phase lastp;
.long   extern list abph[]   = 0,2,1,3; !Note odd - even = path1 - path2

include "./phases.inc";
include "../includes/STANDARD_PARAMS";
include "../includes/THREE_D.inc";

!-----------------------------------------------
! update Spinsight with calculations.
!-----------------------------------------------

.update "rb=1.30*sw";
.update "aqtm=(dw*al)";
.update "dw2 = (2.0*60.0*pw90H)+(2.0*54.0*pw90Hevo)";
.update "al2d = AL2*(dw2)";
.update "rspeed = (1.0/(7500.0*4.00*pw90H)+1.0/(6750.0*4.0*pw90Hevo))/2.0";
.update "extm = (pw90H+(AL2*dw2)+ad+rd+aqtm+pd)";
.update "txduty1=(pw90H+(AL2*dw2)+ad+rd+aqtm)/extm";
.update "time1d = (na+dp)*extm*2.0/60.0";

!-----------------------------------------------
!  Executed once at Start of Experiment
!-----------------------------------------------

.program

dataxfer = al2*al3;

dpc = dp;
PW90H = pw90H;
PW90Hevo = pw90Hevo;
PW90Hdet = PW90H;
aHdet=aH1;
xdelay=pw90H*60.0-pw180X/2.0;
evodelay=pw90Hevo*54.0-pw180X/2.0;
detdelay=xdelay;
path=5;
count3d=1;

.start
!LOOP3D
!{
ncyc2d=1;
loop2D
    {
        abph = abph.start;
     last = last.start;
     hd1=1; ! re-initialize counter to decide which of the 4 to apply
        loop1D
        {
            call mainseq;
   hd1++;
        }
```

```
    if (count3d%AL2 == 0) {
        path++;
        ncyc2d=0;
    }
    count3d++;
    ncyc2d++;
    }
!path++;
!}
.end

!==========================================================!
mainseq:
    if (hd1 > 4) { hd1=1; }
    if (hd1 == 1) {
      aqph=@abph++;
      lastp=@last++;
    }

!Set H1 and Hevo according to path var
if (hd1%2 == 1) {
 if (path < 7) {
  H1 = H1_0110.start;
  Hevo = Hevo_1001.start;
  if (ncyc2d%2 == 0) { Hevo = Hevo_0110.start; }
 } else {
  H1 = H1_1001.start;
  Hevo = Hevo_0110.start;
  if (ncyc2d%2 == 0) { Hevo = Hevo_1001.start; }
 }
}
!Pi phase shift H1 and Hevo for filter
if (hd1%2 == 0) {
 if (path > 6) {
  H1 = H1_0110.start;
  Hevo = Hevo_1001.start;
  if (ncyc2d%2 == 0) { Hevo = Hevo_0110.start; }
 } else {
  H1 = H1_1001.start;
  Hevo = Hevo_0110.start;
  if (ncyc2d%2 == 0) { Hevo = Hevo_1001.start; }
 }
}

if (hd1 > 2) {
 !Alternate Hdet1
 if (path%2 == 0) {
  Hdet1 = Hdet_0110.start; ! odd points phase=0
 } else {
  Hdet1 = Hdet_1001.start; ! even points phase=180
 }
 !Match Hdet2 with Hdet1
 Hdet2 = Hdetp_0110.start;
 if (nhdet%2 == 0) { Hdet2 = Hdetp_1001.start; }
} else {
    !Alternate Hdet1
    if (path%2 == 0) {
        Hdet1 = Hdet_1001.start; ! even points phase=180
    } else {
        Hdet1 = Hdet_0110.start; ! odd points phase=0
    }
 !Match Hdet2 with Hdet1
    Hdet2 = Hdetp_1001.start;
    if (nhdet%2 == 0) { Hdet2 = Hdetp_0110.start; }
}
!!! End Logic

 out  time(10u);
Async;
ch++ ch1;
 out  time(10u);
 out   time(10u) ch1:SC(scH)     ;
 out   time(10u) ch1: OUTA aH1 ;
! Apply H1 01 or 10 for 4 rotors ncyc2d times
for (j=0, j < ncyc2d, j++)
  {
    do(120)
        {
!             out  PM1  ch1:TG|OUTAP aH1|@H1++;
            out  PW90H       ch1:TG|OUTAP aH1|@H1++;
        }
  }
! Apply Hevo 01 or 10 for 4 rotors ncyc2d times
for (j=0, j < ncyc2d, j++)
  {
    do(108)
```

```
        {
!             out  PM1  ch1:TG|OUTAP aHevo|@Hevo++;
            out  PW90Hevo       ch1:TG|OUTAP aHevo|@Hevo++;
        }
  }

! Apply Hdet1 01 or 10 for 4 rotors nhdet times
for (j=0, j < nhdet, j++) {
    do(120)
        {
!             out  PM1  ch1:TG|OUTAP aHdet|@Hdet1++;
            out  PW90Hdet       ch1:TG|OUTAP aHdet|@Hdet1++;
        }
}
! Apply Hdet2 01 or 10 for 4 rotors nhdet times
for (j=0, j < nhdet, j++) {
    do(120)
        {
!             out  PM1  ch1:TG|OUTAP aHdet|@Hdet2++;
            out  PW90Hdet       ch1:TG|OUTAP aHdet|@Hdet2++;
        }
}
!    out PM1   ch1:TG|P(lastp);
 out PW90Hdet  ch1:TG|P(lastp);
 out  rd   ch1:TB|P(p);
 out  ad   ch1:RE|TB;
 outAQ dw  ch1:RE|TB,al;
Sync;
ch--;

ch++ ch2;
 out  time(10u);
 out   time(10u) ch2:SC(scX)     ;
 out   time(10u) ch2:AP(aX,@X180) ;

for (k=0, k < ncyc2d, k++)
  {
     out xdelay;
 out pw180X  ch2:TG;
 out xdelay;
  }
for (k=0, k < ncyc2d, k++)
  {
     out evodelay;
 out pw180X  ch2:TG;
 out evodelay;
  }

for (k=0, k < nhdet, k++) {
     out detdelay;
 out pw180X  ch2:TG;
 out detdelay;
}
for (k=0, k < nhdet, k++) {
     out detdelay;
 out pw180X  ch2:TG;
 out detdelay;
}
  waitS;
ch--;

scan pd;
return;
```

Listing A.6: Infinity+ pulse program phases for HETIE pathways 5-8

```
!ihet_p12 phases
.phase autofix list H1_0110[]=  180,270,180,90,0,90,270,0,270,180,90,180,
                180,270,180,90,0,90,270,0,270,180,90,180,
                180,270,180,90,0,90,270,0,270,180,90,180,
                180,270,180,90,0,90,270,0,270,180,90,180,
                180,270,180,90,0,90,270,0,270,180,90,180,
                0,90,0,270,180,270,90,180,90,0,270,0,
                0,90,0,270,180,270,90,180,90,0,270,0,
                0,90,0,270,180,270,90,180,90,0,270,0,
                0,90,0,270,180,270,90,180,90,0,270,0,
                0,90,0,270,180,270,90,180,90,0,270,0,
                0,90,0,270,180,270,90,180,90,0,270,0,
                0,90,0,270,180,270,90,180,90,0,270,0,
                0,90,0,270,180,270,90,180,90,0,270,0,
                0,90,0,270,180,270,90,180,90,0,270,0,
                0,90,0,270,180,270,90,180,90,0,270,0,
                180,270,180,90,0,90,270,0,270,180,90,180,
                180,270,180,90,0,90,270,0,270,180,90,180,
                180,270,180,90,0,90,270,0,270,180,90,180,
```

```
                180,270,180,90,0,90,270,0,270,180,90,180,
                180,270,180,90,0,90,270,0,270,180,90,180;

.phase autofix list H1_1001[]=  0,90,0,270,180,270,90,180,90,0,270,0,
                0,90,0,270,180,270,90,180,90,0,270,0,
                0,90,0,270,180,270,90,180,90,0,270,0,
                0,90,0,270,180,270,90,180,90,0,270,0,
                0,90,0,270,180,270,90,180,90,0,270,0,
                180,270,180,90,0,90,270,0,270,180,90,180,
                180,270,180,90,0,90,270,0,270,180,90,180,
                180,270,180,90,0,90,270,0,270,180,90,180,
                180,270,180,90,0,90,270,0,270,180,90,180,
                180,270,180,90,0,90,270,0,270,180,90,180,
                180,270,180,90,0,90,270,0,270,180,90,180,
                180,270,180,90,0,90,270,0,270,180,90,180,
                180,270,180,90,0,90,270,0,270,180,90,180,
                180,270,180,90,0,90,270,0,270,180,90,180,
                180,270,180,90,0,90,270,0,270,180,90,180,
                180,270,180,90,0,90,270,0,270,180,90,180,
                0,90,0,270,180,270,90,180,90,0,270,0,
                0,90,0,270,180,270,90,180,90,0,270,0,
                0,90,0,270,180,270,90,180,90,0,270,0,
                0,90,0,270,180,270,90,180,90,0,270,0,
                0,90,0,270,180,270,90,180,90,0,270,0;
.phase autofix list Hevo_1001[]=
265,355,265, 95,  5, 95, 265,355,265, 95,  5, 95, 265,355,265, 95,  5, 95, 265,355,265, 95,  5, 95,
265,355,265, 95,  5, 95,
265,355,265, 95,  5, 95, 265,355,265, 95,  5, 95, 265,355,265, 95,  5, 95, 265,355,265, 95,  5, 95,
 85,175, 85,275,185,275,  85,175, 85,275,185,275,  85,175, 85,275,185,275,  85,175, 85,275,185,275,
 85,175, 85,275,185,275,
 85,175, 85,275,185,275,  85,175, 85,275,185,275,  85,175, 85,275,185,275,  85,175, 85,275,185,275,
 85,175, 85,275,185,275,  85,175, 85,275,185,275,  85,175, 85,275,185,275,  85,175, 85,275,185,275,
 85,175, 85,275,185,275,
 85,175, 85,275,185,275,  85,175, 85,275,185,275,  85,175, 85,275,185,275,  85,175, 85,275,185,275,
265,355,265, 95,  5, 95, 265,355,265, 95,  5, 95, 265,355,265, 95,  5, 95, 265,355,265, 95,  5, 95,
265,355,265, 95,  5, 95,
265,355,265, 95,  5, 95, 265,355,265, 95,  5, 95, 265,355,265, 95,  5, 95, 265,355,265, 95,  5, 95;

.phase autofix list Hevo_0110[]=
 85,175, 85,275,185,275,  85,175, 85,275,185,275,  85,175, 85,275,185,275,  85,175, 85,275,185,275,
 85,175, 85,275,185,275,
 85,175, 85,275,185,275,  85,175, 85,275,185,275,  85,175, 85,275,185,275,  85,175, 85,275,185,275,
265,355,265, 95,  5, 95, 265,355,265, 95,  5, 95, 265,355,265, 95,  5, 95, 265,355,265, 95,  5, 95,
265,355,265, 95,  5, 95,
265,355,265, 95,  5, 95, 265,355,265, 95,  5, 95, 265,355,265, 95,  5, 95, 265,355,265, 95,  5, 95,
265,355,265, 95,  5, 95, 265,355,265, 95,  5, 95, 265,355,265, 95,  5, 95, 265,355,265, 95,  5, 95,
265,355,265, 95,  5, 95,
265,355,265, 95,  5, 95, 265,355,265, 95,  5, 95, 265,355,265, 95,  5, 95, 265,355,265, 95,  5, 95,
 85,175, 85,275,185,275,  85,175, 85,275,185,275,  85,175, 85,275,185,275,  85,175, 85,275,185,275,
 85,175, 85,275,185,275,
 85,175, 85,275,185,275,  85,175, 85,275,185,275,  85,175, 85,275,185,275,  85,175, 85,275,185,275;

.phase autofix list Hdet_0110[]=    18,108,18,252,162,252,108,198,108,342,252,342,
                        18,108,18,252,162,252,108,198,108,342,252,342,
                        18,108,18,252,162,252,108,198,108,342,252,342,
                        18,108,18,252,162,252,108,198,108,342,252,342,
                        18,108,18,252,162,252,108,198,108,342,252,342,  ! 0
                        198,288,198,72,342,72,288,18,288,162,72,162,
                        198,288,198,72,342,72,288,18,288,162,72,162,
                        198,288,198,72,342,72,288,18,288,162,72,162,
                        198,288,198,72,342,72,288,18,288,162,72,162,
                        198,288,198,72,342,72,288,18,288,162,72,162,    ! Pi
                        198,288,198,72,342,72,288,18,288,162,72,162,
                        198,288,198,72,342,72,288,18,288,162,72,162,
                        198,288,198,72,342,72,288,18,288,162,72,162,
                        198,288,198,72,342,72,288,18,288,162,72,162,
                        198,288,198,72,342,72,288,18,288,162,72,162,    ! Pi
                        18,108,18,252,162,252,108,198,108,342,252,342,
                        18,108,18,252,162,252,108,198,108,342,252,342,
                        18,108,18,252,162,252,108,198,108,342,252,342,
                        18,108,18,252,162,252,108,198,108,342,252,342,
                        18,108,18,252,162,252,108,198,108,342,252,342;  ! 0
.phase autofix list Hdet_1001[]=    198,288,198,72,342,72,288,18,288,162,72,162,
                        198,288,198,72,342,72,288,18,288,162,72,162,
                        198,288,198,72,342,72,288,18,288,162,72,162,
                        198,288,198,72,342,72,288,18,288,162,72,162,
                        198,288,198,72,342,72,288,18,288,162,72,162,    ! Pi
                        18,108,18,252,162,252,108,198,108,342,252,342,
                        18,108,18,252,162,252,108,198,108,342,252,342,
                        18,108,18,252,162,252,108,198,108,342,252,342,
                        18,108,18,252,162,252,108,198,108,342,252,342,
                        18,108,18,252,162,252,108,198,108,342,252,342,  ! 0
                        18,108,18,252,162,252,108,198,108,342,252,342,
                        18,108,18,252,162,252,108,198,108,342,252,342,
                        18,108,18,252,162,252,108,198,108,342,252,342,
                        18,108,18,252,162,252,108,198,108,342,252,342,
                        18,108,18,252,162,252,108,198,108,342,252,342,  ! 0
```

```
            198,288,198,72,342,72,288,18,288,162,72,162,
                        198,288,198,72,342,72,288,18,288,162,72,162,
                        198,288,198,72,342,72,288,18,288,162,72,162,
                        198,288,198,72,342,72,288,18,288,162,72,162,
                        198,288,198,72,342,72,288,18,288,162,72,162;    ! Pi
.phase autofix list Hdetp_0110[]=   72,342,72,198,288,198,162,72,162,288,18,288,
                    72,342,72,198,288,198,162,72,162,288,18,288,
                    72,342,72,198,288,198,162,72,162,288,18,288,
                    72,342,72,198,288,198,162,72,162,288,18,288,
                    72,342,72,198,288,198,162,72,162,288,18,288,    ! 0
                    252,162,252,18,108,18,342,252,342,108,198,108,
                    252,162,252,18,108,18,342,252,342,108,198,108,
                    252,162,252,18,108,18,342,252,342,108,198,108,
                    252,162,252,18,108,18,342,252,342,108,198,108,
                    252,162,252,18,108,18,342,252,342,108,198,108,  ! Pi
                    252,162,252,18,108,18,342,252,342,108,198,108,
                    252,162,252,18,108,18,342,252,342,108,198,108,
                    252,162,252,18,108,18,342,252,342,108,198,108,
                    252,162,252,18,108,18,342,252,342,108,198,108,
                    252,162,252,18,108,18,342,252,342,108,198,108,  ! Pi
                    72,342,72,198,288,198,162,72,162,288,18,288,
                    72,342,72,198,288,198,162,72,162,288,18,288,
                    72,342,72,198,288,198,162,72,162,288,18,288,
                    72,342,72,198,288,198,162,72,162,288,18,288,
                    72,342,72,198,288,198,162,72,162,288,18,288;    ! 0

.phase autofix list Hdetp_1001[]=   252,162,252,18,108,18,342,252,342,108,198,108,
                    252,162,252,18,108,18,342,252,342,108,198,108,
                    252,162,252,18,108,18,342,252,342,108,198,108,
                    252,162,252,18,108,18,342,252,342,108,198,108,
                    252,162,252,18,108,18,342,252,342,108,198,108,  ! Pi
                    72,342,72,198,288,198,162,72,162,288,18,288,
                    72,342,72,198,288,198,162,72,162,288,18,288,
                    72,342,72,198,288,198,162,72,162,288,18,288,
                    72,342,72,198,288,198,162,72,162,288,18,288,
                    72,342,72,198,288,198,162,72,162,288,18,288,    ! 0
                    72,342,72,198,288,198,162,72,162,288,18,288,
                    72,342,72,198,288,198,162,72,162,288,18,288,
                    72,342,72,198,288,198,162,72,162,288,18,288,
                    72,342,72,198,288,198,162,72,162,288,18,288,
                    72,342,72,198,288,198,162,72,162,288,18,288,    ! 0
                    252,162,252,18,108,18,342,252,342,108,198,108,
                    252,162,252,18,108,18,342,252,342,108,198,108,
                    252,162,252,18,108,18,342,252,342,108,198,108,
                    252,162,252,18,108,18,342,252,342,108,198,108,
                    252,162,252,18,108,18,342,252,342,108,198,108;  ! Pi
```

A.4 Processing Scripts

Listing A.7: Spinsight macro script for processing HETIE 3D dataset generated by the sequences in Appendix A.3

```
bufa0 = query "Enter_name_of_path1-4_3D_buffer" -s;
bufa = copy bufa0;
bufb0 = query "Enter_name_of_path5-8_3D_buffer" -s;
bufb = copy bufb0;

view bufa -d2 0.0 0.15;

p14 = proj bufa -m sum;
dis p14;

setsize p14 32;
dis p14;

view bufb -d2 0.0 0.15;

p58 = proj bufb -m sum;
dis p58;

setsize p58 32;

view p14 1 1 0;
p1s=extract p14;
dis p1s;

view p14 1 1 1;
p2s=extract p14;
dis p2s;

view p14 1 1 2;
p3s=extract p14;
```

```
dis p3s;

view p14 1 1 3;
p4s=extract p14;
dis p4s;

view p58 1 1 0;
p5s=extract p58;
dis p5s;

view p58 1 1 1;
p6s=extract p58;
dis p6s;

view p58 1 1 2;
p7s=extract p58;
dis p7s;

view p58 1 1 3;
p8s=extract p58;
dis p8s;
```

Listing A.8: Spinsight macro script 2 for processing HETIE 3D dataset generated by the sequences in Appendix A.3

```
/*psum_5t=p12_5s+p34_5s+2.0*p56_5s-2.0*p78_5s;*/
t12=p1s-p2s;
t34=p3s-p4s;
t1234=t12+t34;
delete t12;
delete t34;
t56=p5s-p6s;
t78=p7s-p8s;
t5678=t56-t78;
delete t56;
delete t78;
psum=t1234+t5678;
delete t1234;
delete t5678;
dis psum;
```